ABSTRACT

SYNTHESIS AND CHARACTERIZATION OF METAL-BASED REACTIVE POWDERS

by
Yasmine Aly

Aluminum added to propellants, explosives, and pyrotechnics, boosts their energy density. Different approaches were investigated that could shorten aluminum ignition delays, increase combustion rates, and decrease the tendency of aluminum droplets to agglomerate. Here, Al-based reactive, mechanically milled materials are prepared and characterized.

For powders with Fe, Ni, or Zn additives, the particles consist of an aluminum matrix and inclusions of Fe, Ni, or Zn comprising 10 at % of the bulk composition. For additives of Ni and Zn, only short milling times can be used to prepare composites; intermetallic phases form at longer milling times. Thermogravimetric analysis shows selective oxidation of Zn and Ni at low temperatures, prior to a characteristic first step of Al oxidation. At higher temperatures, the powders oxidize following, qualitatively, the stepwise process reported earlier for the pure Al. The magnitude and kinetics of the low-temperature aluminum oxidation steps are affected by the presence of metal additive inclusions. Heated-filament ignition experiments show that all three prepared composite powders ignite at lower temperatures than pure Al powder. Comparison of the Al-metal composites with $Al{\cdot}Al_2O_3$ reference composites prepared with similar milling conditions suggests that the altered Al morphology, such as developed grain boundary network produced in the milled powders, is primarily responsible for their accelerated low-temperature oxidation. It is concluded that the improved ignition dynamics for the

prepared Al-metal composites is due to a combination of the accelerated low-temperature oxidation with reaction mechanisms altered by the presence of metal inclusions.

For Al·Mg alloys, both internal structures and particle size distributions are adjusted for powders with 50-90 at. % Al. Previous work showed that particles of mechanically alloyed (MA) Al·Mg powders burn faster than similarly sized particles of pure aluminum. However, preparation of MA powders with particle sizes matching those of fine aluminum used in energetic formulations was not achieved. Milling protocol is optimized to prepare equiaxial, μm-scale particles. Ignition temperatures are much lower than those of pure Al powders and are close to those of Mg. For aerosolized powders ignited in air, maximum pressures are higher, rates of pressure rise are greater, and ignition delays are shorter for the MA powders than for pure Al. Single particle laser combustion experiments show that the MA-particles burn in two stages, while the first stage is gradually disappearing at higher Al concentrations.

Finally, it has been shown that a range of MA-Al·Mg powders can be prepared with different compositions and particle sizes. Conventionally, such alloys are prepared by melt processing. Here, the oxidation, ignition, and combustion characteristics are compared for two powders of Al·Mg with similar bulk compositions and particle sizes: one produced via MA, and another, produced via grinding of a cast alloy. Low-temperature exothermic features are observed for the MA powder but not for the cast-alloyed powder in thermo-analytical experiments. MA powders have slightly lower ignition temperatures than cast-alloyed powders. Aerosol combustion experiments show a substantial increase in both the maximum pressure and rate of pressure rise for the MA powders as compared to the cast alloyed powders. In single particle laser ignition

experiments, MA particles ignite more readily than cast alloyed particles. MA powders burn in a staged sequence, with the first stage dominated by combustion of Mg and the second stage representing primarily combustion of Al. No similar staged combustion behavior is observed for the cast-alloyed powders, which generates very short emission pulses with a relatively low brightness, and thus may not have burned completely. It is proposed that the difference in the structure and morphology between the MA and cast alloyed particles results in different ignition and combustion scenarios.

SYNTHESIS AND CHARACTERIZATION OF METAL-BASED REACTIVE POWDERS

by
Yasmine Aly

A Dissertation
Submitted to the Faculty of
New Jersey Institute of Technology
in Partial Fulfillment of the Requirements for the Degree of
Doctor of Philosophy in Chemical Engineering

Otto H. York Department of Chemical, Biological, and Pharmaceutical Engineering

August 2014

.

APPROVAL PAGE

SYNTHESIS AND CHARACTERIZATION OF METAL-BASED REACTIVE POWDERS

Yasmine Aly

Dr. Edward L. Dreizin, Dissertation Advisor Date
Professor of Chemical, Biological, and PharmaceuticalEngineering, NJIT

Dr. Rajesh N. Dave, Committee Member Date
Distinguished Professor of Chemical, Biological, and Pharmaceutical Engineering, NJIT

Dr. Robert B. Barat, Committee Member Date
Professor of Chemical, Biological, and Pharmaceutical Engineering, NJIT

Dr. MirkoSchoenitz, Committee Member Date
Associate Research Professor of Chemical, Biological, and Pharmaceutical Engineering, NJIT

Dr. Victor Stepanov, Committee Member Date
Senior Scientist, U.S. Army RDECOM-ARDEC, Picatinny Arsenal, NJ

BIOGRAPHICAL SKETCH

Author: Yasmine Aly

Degree: Doctor of Philosophy

Date: August 2014

Undergraduate and Graduate Education:

- Doctor of Philosophy in Chemical Engineering,
  New Jersey Institute of Technology, Newark, NJ, 2014

- Bachelor of Science in Chemical Engineering,
  New Jersey Institute of Technology, Newark, NJ, 2008

Major: Chemical Engineering

Presentations and Publications:

Peer-Reviewed Journal Publications:

Aly, Y. and Dreizin, E.L., "Ignition and combustion of Al·Mg alloy powders prepared by different techniques," *Combustion and Flame*, To be submitted, 2014.

Corcoran, A.L., Wang, S., Aly, Y., Dreizin, E.L., "Combustion of mechanically-alloyed Al·Mg powders in products of a hydrocarbon flame," *Combustion, Science, and Technology*, Under Review, 2014.

Machado, M.A., Rodriguez, D.A., Aly, Y., Schoenitz, M., Dreizin, E.L., Shafirovich, E., "Nanocomposite and mechanically alloyed reactive materials as energetic additives in chemical oxygen generators," *Combustion and Flame*, Article in Press, 2014.

Abraham, A., Zhang, S., Aly, Y., Schoenitz, M., Dreizin, E.L., "Aluminum-iodoform composite reactive material."*Advanced Engineering Materials*, Article in Press, 2014.

Aly, Y., Hoffman, V.K., Schoenitz, M., Dreizin, E.L., "Reactive, mechanically-alloyed Al·Mg powders with customized particle sizes and compositions."*Journal of Propulsion and Power*, 30:1, pp. 96-104, 2014.

Aly, Y., Zhang, S., Schoenitz, M., Hoffmann, V.K., Dreizin,E.L., Yermakov, M., Indugula, T., Grinshpun, S.A., "Iodine-containing aluminum-based fuels for inactivation of bio-aerosols."*Combustion and Flame*, 161:1, pp. 303-310, 2014.

Aly, Y., Hoffman, V.K., Schoenitz, M., Dreizin, E.L., "Preparation, ignition, and combustion of mechanically alloyed Al-Mg powders with customized particle sizes."*MRS Proceedings*, 1521, 2013.

Aly, Y., Schoenitz, M.,Dreizin, E.L., "Ignition and combustion of mechanically alloyed Al-Mg powders with customized particle sizes."*Combustion and Flame*, 160:4, pp. 835-842, 2013.

Dreizin, E.L., Badiola, C., Zhang, S., Aly, Y., "Particle combustion dynamics of metal-based reactive materials."*International Journal of Energetic Materials and Chemical Propulsion*, 10:4, pp. 297-319, 2012.

Aly, Y., Schoenitz, M.,Dreizin, E.L., "Aluminum-Metal Reactive Composites."*Combustion Science and Technology*, 183:10, pp. 1107-1132, 2011.

Ermoline, A., Aly, Y., Trunov, M.A., Schoenitz, M.,Dreizin, E.L., "Preparation and characterization of granular hybrid reactive materials."*International Journal of Energetic Materials and Chemical Propulsion*, 9:3, pp. 267-284, 2010.

Vummidi, S.L., Aly, Y.,Schoenitz, M., Dreizin, E.L., "Characterization of fine aluminum powder coated with nickel as a potential fuel additive."*Journal of Propulsion and Power*, 26:3, pp. 454-460, 2010.

Conference Proceedings:

Aly, Y., Schoenitz, M., Dreizin, E.L., "Aluminum-boron-halogen ternary reactive composite powders."*7th U.S. National Combustion Meeting*, Atlanta, GA. March 20-23, 2011.

Aly, Y., Stamatis, D., Badiola, C., Dreizin, E.L., "Ternary reactive nanocomposite powders." *49th AIAA Aerospace Sciences Meeting*, Orlando, FL. January 4-7, 2011.

Presentations:

Aly, Y., Schoenitz, M., Dreizin, E.L., "Ignition and combustion of Al·Mg alloy powders prepared by different techniques."*Gordon Research Seminar and Conference*, Newry, ME, June 13-21, 2014.

Aly, Y., Schoenitz, M., Dreizin, E.L., "Mechanically alloyed Al·Mg powders with customized particle sizes and compositions."*Johnson & Johnson Engineering Showcase*, New Brunswick, NJ, February 2014.

Aly, Y., Schoenitz, M., Dreizin, E.L., "Ignition and combustion of Al·Mg alloy powders prepared by different techniques."*American Institute of Chemical Engineers (AIChE) Annual Meeting*, San Francisco, CA, November 5-7, 2013.

Aly, Y., Schoenitz, M., Dreizin, E.L., "Mechanically alloyed Al·Mg powders with customized particle sizes and compositions."*AIChE Annual Meeting*, San Francisco, CA,November 5-7, 2013.

Aly, Y., Schoenitz, M., Dreizin, E.L., "Mechanically alloyed Al-based powders with customized particle sizes and compositions."*9th Annual NJIT Graduate Student Research Day*, Newark, NJ, October 2013.

Aly, Y., Schoenitz, M., Dreizin, E.L., "Mechanically alloyed Al-based powders with customized particle sizes and compositions."*DTRA Basic Research Technical Review*, Springfield, VA,July 2013.

Aly, Y., Schoenitz, M., Dreizin, E.L., "Preparation and characterization of Aluminum-based reactive materials with customized combustion characteristics."*Johnson & Johnson Engineering Showcase*, New Brunswick, NJ, February 2013.

Aly, Y., Hoffman, V.K., Schoenitz, M., Dreizin, E.L., "Preparation, ignition, and combustion of mechanically alloyed Al-Mg powders with customized particle sizes."*Materials Research Society (MRS) Fall Meeting*, Boston, MA, November 26, 2012.

Aly, Y., Hoffman, V.K., Schoenitz, M., Dreizin, E.L., "Preparation, ignition, and combustion of mechanically alloyed Al-Mg powders with customized particle sizes."*Society of Women Engineers (SWE) Annual Conference*, Houston, TX, November 8, 2012.

Aly, Y., Schoenitz, M., Dreizin, E.L., "Aluminum-based reactive materials with customized combustion characteristics."*AIChE Annual Meeting*, Pittsburgh, PA, October 2012.

Aly, Y., Schoenitz, M., Dreizin, E.L., "Aluminum-based reactive materials with customized combustion characteristics."*DTRA Basic Research Technical Review*, Springfield, VA,July 2012.

Aly, Y., Schoenitz, M., Dreizin, E.L., "Aluminum-based reactive materials with customized combustion characteristics."*Gordon Research Conference*, West Dover, VT, June 2012.

Aly, Y., Schoenitz, M., Dreizin, E.L., "Aluminum-based reactive materials with customized combustion characteristics."*8th Annual NJIT Graduate Student Research Day*, Newark, NJ, October 2012.

Aly, Y., Schoenitz, M., Dreizin, E.L., "Aluminum-based ternary reactive composite powders."*AIAA Region I YPSE Conference*, Laurel, MD, November 4, 2011.

Aly, Y., Schoenitz, M., Dreizin, E.L., "Aluminum-based ternary reactive composite powders."*7th Annual NJIT Graduate Student Research Day*, Newark, NJ, November 2011.

Aly, Y., Schoenitz, M., Dreizin, E.L., "Aluminum-based ternary reactive composite powders."*NJIT Provost Research Day*, Newark, NJ, October 2011.

Aly, Y., Schoenitz, M., Dreizin, E.L., "Aluminum-based ternary reactive composite powders."*AIChE Annual Meeting*, Minneapolis, MN, October 20, 2011.

Aly, Y., Dupiano, P., Schoenitz, M., Dave, R., Iqbal, Z., Dreizin, E.L., "Reactive materials for advanced energetics," *RDECOM-ARDEC Technical Meeting*, Picatinny, NJ, October 2011.

Aly, Y., Schoenitz, M., Dreizin, E.L., "Aluminum-boron-halogen ternary reactive composite powders."*7th U.S. National Combustion Meeting*, Atlanta, GA, March 20-23, 2011.

Aly, Y., Stamatis, D., Badiola, C., Dreizin, E.L., "Ternary reactive nanocomposite powders." *49th AIAA Aerospace Sciences Meeting*, Orlando, FL,January 4-7, 2011.

Aly, Y., Schoenitz, M., Dreizin, E.L., "Al-metal reactive composites."*AIChE Annual Meeting*,Salt Lake City, UT, November 11, 2010.

Aly, Y., Schoenitz, M., Dreizin, E.L.,"Al-metal reactive composites." 6th *Annual NJIT Graduate Student Research Day*, Newark, NJ, October 2010.

Aly, Y., Schoenitz, M., Dreizin, E.L., "Al-based reactive composite powders."*NJIT Dana Knox Student Research Showcase*, Newark, NJ, April 14, 2010.

Aly, Y., Schoenitz, M., Dreizin, E.L., "Al-metal reactive nanocomposite materials."*AIChE Annual Meeting*, Nashville, TN, November 13, 2009.

“Feelings of worth can flourish only in an atmosphere where individual differences are appreciated, mistakes are tolerated, communication is open, and rules are flexible—the kind of atmosphere that is found in a nurturing family.”

-Virginia Satir

To my parents, Hesham and Nevein, for their love, support, and encouragement, teaching me the importance of education and setting high goals, and instilling in me the confidence to achieve them

To my sisters, Nisma, Sarah, Noor, Lena, and Nisreen, and to my brother, Mahmoud, for never letting a dull moment pass

To my husband, Ahmed, for loving and supporting me all while keeping me happy

ACKNOWLEDGMENT

Completing my PhD, while certainly a personal achievement, was not an accomplishment that I reached alone. There are many individuals that I would like to acknowledge as supporters. First and foremost, I thank Allah (God) for allowing me to reach my goals successfully, making the journey possible, and surrounding me with the wonderful support system I have.

I would like to express my deepest gratitude to my advisor, Edward L. Dreizin, for his continued support, guidance, and sound advisement. His knowledge, intellect, intuition, and compassion were key factors in this achievement. He has been and will always be a great role model for me and a source of inspiration to think bigger, do better, and achieve more. He has always helped me keep things in perspective and provided great direction in my work. He has not only been the best advisor I could have asked for, but also provided a listening ear for more personal matters. Although our relationship as student/advisor ends here, I am certain and look forward to him always being my mentor. Thank you!

Next, I would like to thank Dr. Mirko Schoenitz for always being one of my biggest advocates. He has been a co-advisor of sorts to me, always providing me with support whenever needed. The lab shortcuts and tricks I have learned from him were very important and made lab research a lot easier. He has been the best of mentors. Words cannot describe our relationship, but it has been a great experience and pleasure working with him. I hope he is aware of how much I have learned from him throughout the years and how valuable his presence has been to me.

I would like to thank the remaining members of my thesis committee, Drs. Rajesh Dave, Robert Barat, and Victor Stepanov, for the time they each took out of their busy schedules to provide me with insight and a fresh perspective in my work.

I would like to thank the Defense Threat Reduction Agency (DTRA), Picatinny Arsenal, and any other sources that have funded my various projects and making the research possible.

Throughout the years of this journey, I have worked with many students and support staff within my research group. I would like to acknowledge former students Demitrios Stamatis, Ervin Beloni, Carlo Badiola, Shasha Zhang, and Priya Radhi Santhanam as being my earliest trainers in the lab, great collaborators, making my work environment highly enjoyable, and eventually becoming my greatest friends. I would like to also thank former support staff Vern Hoffman, Bob Gill, and Alexandre Ermoline for all their assistance. I would like to acknowledge current group members and friends who I have had a pleasure working with: Shashank Lakshman Vummidi, Rayon Williams, Hongqi Nie, Ani Abraham, Song Wang, and Amy Corcoran.

I would like to acknowledge and thank all the faculty and staff of the Otto H. York Department of Chemical, Biological, and Pharmaceutical Engineering whom I have had the pleasure of dealing with during all my years here at NJIT. It was my absolute pleasure working with all the current and former members of the Society of Women Engineers (SWE). I have seen great pleasures from that experience and I appreciate all the support I have gained through SWE.

I would like to acknowledge the Office of Graduate Studies for their help in preparing and composing my thesis document and for all other services they have provided me with.

Last, but certainly not least, I would like to thank my family. My parents, Hesham and Nevein Aly, along with my siblings, Nisma, Sarah, Noor, Mahmoud, Lena, and Nisreen, as well as my husband, Ahmed, for being so pivotal in all my successes. They have kept me sane throughout this journey providing me with unconditional love, support, and encouragement at all times. They have been with me every step of the way, through all the good times and the bad. I greatly appreciate everything they have done and sacrificed for me. Thank you all so very much. I love you dearly.

TABLE OF CONTENTS

TABLE OF CONTENTS

(Continued)

Chapter **Page**

TABLE OF CONTENTS

(Continued)

Chapter **Page**

TABLE OF CONTENTS

(Continued)

LIST OF TABLES

LIST OF FIGURES

LIST OF FIGURES

(Continued)

LIST OF FIGURES

(Continued)

LIST OF FIGURES

(Continued)

LIST OF FIGURES

(Continued)

CHAPTER 1

INTRODUCTION

Energetic materials (EMs) such as propellants, explosives, and pyrotechnics are used in both constructive and destructive purposes in civil and military applications. Military EMs are used in variety of munitions (shells, grenades, missiles, rocket warheads, etc.) whereas civil EMs exploited in mining, quarrying, construction, etc. [1]. Some of the most commonly used EMs are the organic, high-nitrogen, monomolecular compounds, such as TNT, HMX, RDX, and CL-20, dubbed "secondary high explosives" [1-3]. These materials are capable of rapid exothermic reactions that are rate limited by the chemical kinetic of production of H_2O and CO_2 as products upon complete decomposition of the monomolecular energetic compounds [4-6]. The drawback of these materials is their relatively low energy densities.

Metal fuels such as B, Al, Mg, Ti, and Zr added to energetic formulations can oxidize in the surrounding air and/or in the produced H_2O and CO_2, and create higher combustion energies and, therefore, higher energy densities of EMs. These advantages are due to the metals' high gravimetric and volumetric reaction enthalpies when compared to the high explosives mentioned previously. The higher combustion enthalpies give rise to higher combustion temperatures, making the metallized formulations still more advantageous to use over monomolecular explosives and other EMs [3]. The disadvantage of using metal fuels in practical applications is their low rates of energy release as compared to monomolecular EMs. The long ignition delays and low burn

rates, typical of the heterogeneous reactions of burning metal fuels impede the overall rate of combustion for metallized EMs [3, 7, 8].

Based on the attractive thermodynamics of combustion, research efforts sustained over several decades are focused on the utilization of metals and metal-based fuels as additives to various formulations with the goal of synthesis of materials that offer higher energy densities, shorter ignition delays, higher burn rates, desired reaction products, and higher combustion enthalpies and temperatures.

Among various metal additives, aluminum is used most widely due to its high combustion enthalpy and low cost [9-11]. Multiple Al-based nanocomposite reactive materials have been explored recently, including thermite compositions prepared by mixing nanopowders of Al and metal oxides [12-14], mechanical milling of coarse starting powders [15, 16], sol-gel processing [17-21], self-assembly [22, 23], and layered deposition producing multilayered foils [24-27]. In most cases, a highly exothermic reaction is expected to occur between aluminum and one of the additional components resulting in an accelerated ignition due to the intimate contact of the developed reactive interface area. The addition of solid oxidizers, however, inevitably reduces the overall energy density of the metal fuel additives, reducing their ability to react with CO_2, H_2O and surrounding air.

Recently, extensive studies have focused on the use of mechanical ball milling to prepare Al-based nanocomposites and mechanically alloyed materials. One of the advantages of preparing materials by mechanical milling over mixing nanopowders is that the reactive interface structures and properties in the milled materials lack the natural passivating oxide layer on the surface of Al or other metals used as fuels. Within Al-

based mechanically alloyed (MA) materials, the reactivity of Al can be greatly assisted by a highly reactive metal additive. Alloys can be designed to undergo phase changes upon heating, which generate fresh surface capable of rapid reactions with ambient oxidizers [3]. Previous studies have shown Al combustion to be enhanced when aluminum is alloyed or MA with Ti, Mg, or Li [28-31]. Exothermic formation of an Al·Ti and Al·Mg intermetallic phases and selective oxidation of Mg and Li were proposed to increase the overall reactivity of the respective alloys.

1.1 Objective

To further studies on mechanically milled materials, this work is collectively focused on the synthesis of Al-based materials with diverse metal additives, such as Fe, Ni, Zn, and Mg. The resulting nanocomposites and alloys are then characterized with respect to their ignition and combustion characteristics. Despite small differences in individual objectives for each material system, the goal, generally, is to prepare composites or alloys with enhanced reactivity compared to pure Al powders. It is further desired to understand the mechanism of the achieved enhanced behavior.

For particles of Al and Fe, Ni, or Zn additives, the particles consist of an aluminum matrix and inclusions of Fe, Ni, or Zn comprising 10 at % of the bulk composition. The bulk compositions are aluminum-rich to take advantage of the high aluminum combustion enthalpy. The idea here is to finely mix aluminum with a metal, rather than an oxide. The formation of intermetallic compounds is undesired. The materials prepared are micron-sized powders in which each particle has an aluminum matrix and micron or nano-sized inclusions of the metal additive. These materials have higher energy density than nanocomposite thermites with similar morphology and are

expected to be more reactive than alloyed powders with the same bulk compositions, in which components are bonded into intermetallic compounds. It is expected that the reactivity of such composite materials will be improved compared to both pure aluminum and respective intermetallics because of several reasons. Early selective oxidation of the added metal can offer an energy boost during the particle pre-heating. An exothermic intermetallic reaction can occur; this reaction would be particularly important for such systems as Al-Ni and others with relatively high reaction enthalpy. The kinetics of aluminum oxidation, controlled by the growth kinetics for various aluminum oxide polymorphs are also expected to change as a result of the combined oxidation processes of different metals, and because of formation of ternary oxides, less protective than pure alumina. Finally, an increase in the surface area of the reactive interface, including multiple grain boundaries in the prepared nanocomposite materials, is expected to increase the rate of their heterogeneous oxidation. Different mechanisms are expected to improve reactivity of Al-metal nanocomposite materials for different metal additives.

Another objective is to adjust particle size distribution for the prepared MA powders. The focus is on Al·Mg alloys with 50-90 at. % Al. In order for many of these materials to be practically useful, their particle size distribution should be fine-tuned to make them compatible with the existing protocols for preparation of energetic formulations. However, cold welding that often occurs due to the ductile nature of Al prevents synthesis of MA powders with useful size distributions. Process control agents (PCAs) have been used previously to avoid or minimize cold welding; similarly, smaller particle sizes can, in principle, be obtained by using smaller milling balls [32]. However, Al-based MA powders with attractive compositions prepared to date [30, 33] were too

coarse for practical applications. Long milling durations and increased PCA amounts can be used to further reduce particle size, but milling tools and PCAs contaminate the desired formulations [32].

Despite significant attention to combustion characteristics of Al·Mg alloys [34-36], combustion of fine particles of such alloys has not been studied in detail, most likely because such fine particles were not readily available. Thus, enabling preparation of fine Al·Mg alloy powders by mechanical alloying, a very versatile materials manufacturing method, is of substantial interest. The issue is challenging primarily due to high ductility of Al, which tends to result in cold welding and coarse product particles. In previous research, elemental iodine was milled with aluminum resulting in particle size reduction [37]. In this work, both internal structures and particle size distributions of mechanically milled Al·Mg alloys are adjusted for powders with 50-90 at. % Al. Iodine is used as an additional PCA enabling a better control over the particle shapes and sizes for an Al-Mg alloy. A 2-step ball milling technique is implemented with the first milling step used to achieve the desired structural and compositional refinement. Iodine is added and smaller milling balls are used for the second milling step aimed to reduce particle sizes. Combustion and ignition of the prepared materials is investigated and correlations between different oxidation, ignition, and combustion characteristics are studied and compared.

Finally, after the several studies showing that mechanical alloying can be used to prepare a range of Al·Mg powders with different compositions and particle sizes, the final chapter describes a study aimed at comparing the oxidation, ignition, and combustion characteristics between two powders of Al·Mg with similar bulk

compositions and particle sizes: one produced via mechanical alloying, and another, produced via grinding of a cast alloy. Conventionally, such alloys are prepared by melt processing; however, no direct comparisons of combustion characteristics of such alloys prepared using different methods are available. Although both materials may contain the same bulk Al·Mg compositions, the structures and phase compositions may be different. MA powders are likely to contain nanocomposite structures and poorly crystalline solid solution phases. On the other hand, cast-alloyed powders are expected to contain well-crystallized intermetallics. The effect of such structural and morphological differences on the ignition and combustion of alloys is unknown. An attempt to understand these differences is made in this final study.

CHAPTER 2

ALUMINUM-METAL REACTIVE COMPOSITES

2.1 Abstract

Three binary Al-based reactive composite powders are prepared by mechanical milling. The particles have an aluminum matrix and inclusions of Fe, Ni, or Zn comprising 10 at % of the bulk composition. For additives of Ni and Zn, only short milling times can be used to prepare composites; intermetallic phases form at longer milling. Short milling times yield relatively coarse particles with flake-like shapes. Prepared powders are characterized using electron microscopy and x-ray diffraction. Oxidation and ignition of the materials are studied using thermal analysis and heated-filament ignition, respectively. Thermogravimetric analysis shows selective oxidation of Zn and Ni at low temperatures, prior to a characteristic first step of Al oxidation. At higher temperatures, the powders oxidize following, qualitatively, the stepwise process reported earlier for the pure Al powders. The magnitude and kinetics of the low-temperature aluminum oxidation steps are substantially affected by the presence of the metal inclusions. Heated-filament ignition experiments showed that all three prepared composite powders ignite at lower temperatures than pure Al powder. Comparison of the Al-metal composites with $Al{\cdot}Al_2O_3$ reference composites prepared with similar milling conditions suggests that the altered Al morphology, such as developed grain boundary network produced in the milled powders, is primarily responsible for their accelerated low-temperature oxidation. It is further observed that simply an increase in the low-temperature oxidation rate detected in thermo-analytical experiments is insufficient to achieve ignition of the

material under rapid heating conditions. It is concluded that the improved ignition dynamics for the prepared Al-metal composites is due to a combination of the accelerated low-temperature oxidation with reaction mechanisms altered by the presence of metal inclusions.

2.2 Introduction

to propellants, explosives, and pyrotechnic compositions increase the energy density of respective formulations. Among various metal additives, aluminum is used most widely due to its high combustion enthalpy and low cost [9-11]. Multiple Al-based nanocomposite reactive materials have been explored recently, including thermite compositions prepared by mixing nanopowders [12-14], mechanical milling of coarse starting powders [15, 38], sol-gel processing [17-21], self-assembly [22, 23], and layered deposition producing multilayered foils [24-27]. In most cases, a highly exothermic reaction is expected to occur between aluminum and one of the additional components resulting in an accelerated ignition. However, adding solid oxidizers inevitably reduces the overall energy density of the metal fuel additives. Aluminum combustion was also shown to be enhanced when aluminum is alloyed or mechanically alloyed with titanium, magnesium, or lithium [28, 29, 31, 33]. Exothermic formation of an Al-Ti intermetallic phase and selective oxidation of Mg and Li were proposed to increase the overall reactivity of the respective alloys.

New types of Al-based reactive composite materials are explored in this article. In these materials, aluminum is finely mixed with a metal, rather than an oxide. The formation of intermetallic compounds is avoided. The materials prepared are micron-sized powders in which each particle has an aluminum matrix and micron or nano-sized

inclusions of the metal additive. The bulk compositions are aluminum-rich to take advantage of the high aluminum combustion enthalpy. Such materials have higher energy density than nanocomposite thermites with similar morphology and are expected to be more reactive than alloyed powders with the same bulk compositions, in which components are bonded into intermetallic compounds. It is expected that the reactivity of such composite materials will be improved compared to both pure aluminum and respective intermetallics because of several reasons. Early selective oxidation of the added metal can offer an energy boost during the particle pre-heating. An exothermic intermetallic reaction can occur; this reaction would be particularly important for such systems as Al-Ni and others with relatively high reaction enthalpy. The kinetics of aluminum oxidation, controlled by the growth kinetics for various aluminum oxide polymorphs are also expected to change as a result of the combined oxidation processes of different metals, and because of formation of ternary oxides, less protective than pure alumina. Finally, an increase in the surface area of the reactive interface, including multiple grain boundaries in the prepared nanocomposite materials, is expected to increase the rate of their heterogeneous oxidation. Different mechanisms are expected to improve reactivity of Al-metal nanocomposite materials for different metal additives.

2.3 Experimental

2.3.1 Material Synthesis

Starting materials used in the synthesis of the composites included Al powder (Atlantic Equipment Engineers, 99.8% pure, -325 mesh); Fe powder (Alfa-Aesar, 98% metals basis, -325 mesh, reduced); Zn dust (Acros Organics, >97%); and Ni powder (Alfa-

Aesar, 99.9% metals basis, APS 3-7 μm). Powders were mechanically milled using a SPEX Certiprep 8000 shaker mill with 50-ml flat-ended steel vials and steel milling media (9.5 mm diameter balls.) Each vial was loaded in argon with a 5-g powder load and a ball-to-powder mass ratio (BPR) of 10. To take advantage of the high combustion enthalpy of aluminum, bulk compositions of each system were aluminum-rich (90 atomic % Al). Stearic acid ($CH_3(CH_2)_{16}COOH$, Fluka, ≥ 97.0%), added as 2 wt. % of the initial powder load, was used as a process control agent to inhibit cold-welding and prevent partial reactions during the milling process.

Milling times were varied for each of the three materials systems. For Al-Fe, it was shown that no phases other than α(Al) solid solution form for the composition used in this study milled for up to 20 hours [39]. Longer milling times are impractical. To examine the formation of Al-Fe composites at shorter milling times, two samples were prepared by milling blended Al and Fe powders for 120 and 480 min. Similarly, two different milling times, 20 and 120 min, were used to prepare Al-Zn and Al-Ni composites. For Al-Zn, it was reported [40] that peaks of Zn in x-ray diffraction patterns decrease with increasing milling time due to dissolution of Zn in Al. However, for the Al powder milled with 10 at. % Ni, it was reported that no aluminide phases form for milling durations past 30 hours, with no details given about the composite structure [41]. Our preliminary experiments showed that for ball-milled Al-Zn powder blends, x-ray diffraction peaks of Zn disappear after a relatively short (~30 min) milling time. Therefore, Al-Zn composites were prepared using a short, 20-min period of milling. In addition, a set of samples were prepared using a longer milling time; in those samples, formation of intermetallic phases was anticipated.

To specifically address the effect of morphology created by mechanical milling in aluminum-rich composite materials, two reference $Al{\cdot}Al_2O_3$ composite samples were also prepared. Nanocrystalline α-Al_2O_3 powder (Inframat® Advanced Materials, crystal size ~40 nm, particle size ~150 nm) was used. The bulk composition included 90 volume % of Al, similar to that in the prepared metal-metal composites. The milling times were 20 and 120 min as for the prepared metal-metal composites.

Table 2.1 summarizes the compositions and respective milling times used in the preparation of materials used in this study.

Table 2.1 Prepared Materials

Composition	**Additive Weight %**	**Milling Time [min.]**
$Al_{0.9}Fe_{0.1}$	18.7	120
		480
$Al_{0.9}Zn_{0.1}$	21.2	20
		120
$Al_{0.9}Ni_{0.1}$	19.5	20
		120
$Al{\cdot}Al_2O_3$	29.6	20
		120

2.3.2 Material Characterization

Powder morphology and elemental composition were examined using a LEO 1530 Field Emission Scanning Electron Microscope (SEM), equipped with an energy dispersive x-ray spectrometer (EDX). Samples were embedded in epoxy and cross-sectioned for analysis. Images were taken using backscattered electron imaging. Phase compositions of the samples were analyzed using X-ray Diffraction (XRD) on a Phillips X'pert MRD

powder diffractometer operated at 45 kV and 40 mA, using Cu Kα radiation (λ = 1.5438 Å). Samples were mounted on a zero-background quartz plate for the analysis and scanned for 2 hours between 10-80°.

Particle size distributions of the prepared materials were measured with low-angle laser light scattering using a Beckman-Coulter LS230 Enhanced Particle Analyzer. Powder suspensions for analysis were prepared in distilled water and ultrasonicated to minimize particle agglomeration.

Oxidation was studied using differential scanning calorimetry (DSC) and thermogravimetric analysis (TGA) using a Netzsch Simultaneous Thermal Analyzer STA409 PG with a DSC sample carrier and corundum sample crucibles. The thermal analyzer was temperature-calibrated using the known melting points of a set of certified high-purity metals. Measurements were performed in a mixed 1:1 ratio of oxygen (50 ml/min, Matheson, 99.98% purity) and ultra-high purity argon (50 ml/min, Matheson, 99.99%) at various heating rates between 5-40 K/min. In each experiment, samples were heated to 1495 °C, cooled to room temperature, and heated again to the same maximum temperature at the same heating rate. The second heating was then subtracted from the first to obtain the baseline for the measurement.

For these oxidation experiments, samples of the prepared Al-metal composites were blended with nanocrystalline α-Al_2O_3 powder (Inframat® Advanced Materials, crystal size ~40 nm, particle size ~150 nm). This was done to minimize the effect of coalescence of Al particles upon their melting. A sample blend consisted of 25 wt. % of a prepared composite and 75 wt. % of α-Al_2O_3. The powders were mixed in hexane using an ultrasonic bath for 1.5 hours. Once blended, the samples were dried in vacuum

and used for the oxidation experiments.

Ignition of the prepared materials was analyzed using a heated filament ignition apparatus described in detail elsewhere [42, 43]. A thin layer of powder was coated onto a nickel-chromium alloy heating wire (manufacturer-specified working temperature range up to 1953 K). The filament was heated by a DC current and its temperature was monitored optically using an infrared pyrometer focused on an uncoated section of the filament. Concurrently, light emission from the powder coating was measured using a photodiode sensor, in which a sharp onset of light emission was identified as the ignition instant. The temperature measured by the pyrometer at this instant was assumed to be the ignition temperature. Such experiments were conducted in air for a range of heating rates between 103 and 105 K/s.

2.4 Results

2.4.1 SEM and Particle Size Distribution

SEM micrographs illustrating particle shapes and morphologies of the prepared materials are shown in Figure 2.1. For the Al-Fe composite, the particles are mostly equiaxial and fairly coarse. Images of the Al-Zn and Al-Ni composites prepared with shorter milling times show a mixture of large flakes and smaller equiaxial particles. Similar, equiaxial particle shapes are observed for all materials for the powders prepared with extended milling times. The morphologies of reference $Al{\cdot}Al_2O_3$ samples milled for 20 and 120 min are similar to those of the Al-metal composites prepared with the same milling times. A mix of large flakes and equiaxial particles is observed for the 20-min milled sample, and equiaxial particles with broad range of dimensions are observed for the sample milled for 120 min.

Results of the particle size distribution measurements presented in Figure 2.2 show a broad range of particle sizes. Average particle sizes are 31.5, 37.6, and 46.6 μm for the Al-Fe, Al-Zn, and Al-Ni composites, respectively. For the $Al{\cdot}Al_2O_3$ powders, average particle sizes were 42.8 and 42.5 μm for the milling times of 20 and 120 min, respectively. Also shown in Figure 2.2 are the size distributions for powder samples obtained with extended milling times (see Table 2.1) For Al-Fe and Al-Zn, the powders milled longer have larger particle sizes; however, for Al-Ni, extended milling results in an apparent size reduction by almost 10 μm.

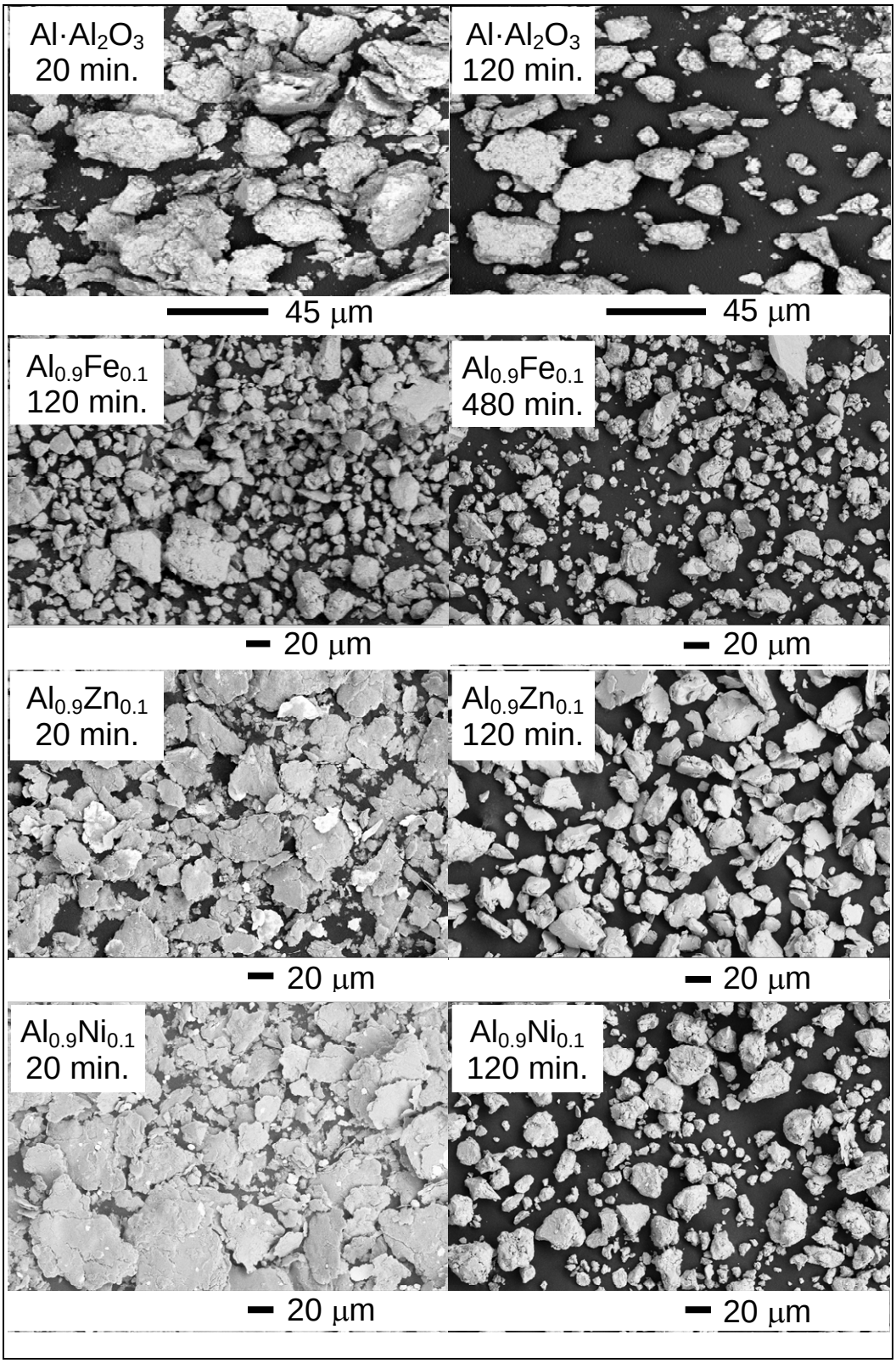

Figure 2.1 SEM micrographs of the milled materials. The left and right columns represent the composite and alloyed powders obtained respectively at shorter and longer milling times.

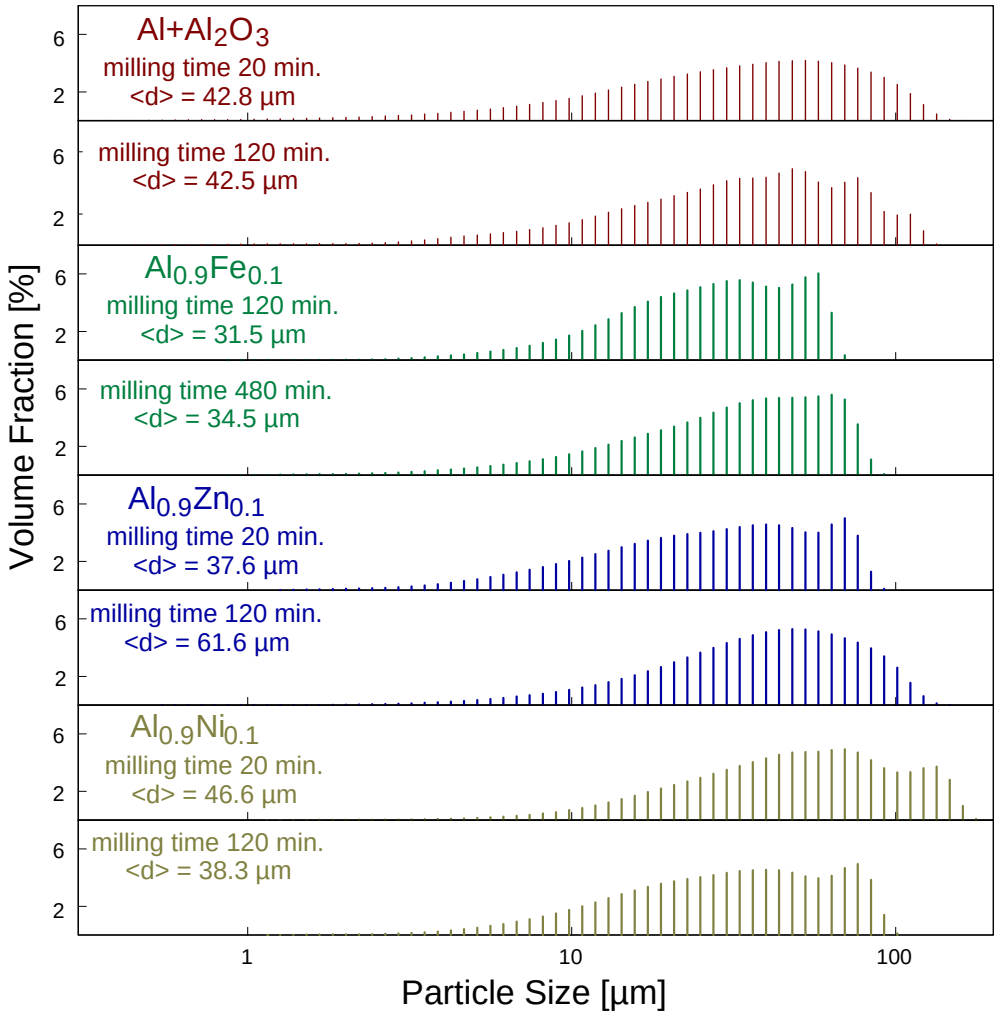

Figure 2.2 Particle size distributions of the milled materials.

Due to the flake-like shapes of the Al-Zn and Al-Ni particles (Figure 2.1), the distributions shown in Figure 2.2 may not give an adequate measure of the particle dimensions. To further characterize particle sizes, the prepared powders were passed through a stack of standard sieves. Figure 2.3 shows the cumulative size distributions of the three powders based on sieving. In both Figures 2.2 and 2.3, the Al-Fe composite appears to include finer particles than the other materials, which is clearly the result of a more equiaxial shape of the respective particles. Based on sieving, Al-Zn appears to be

the coarsest, most likely simply indicating the greatest aspect ratio for the prepared flake-like particles.

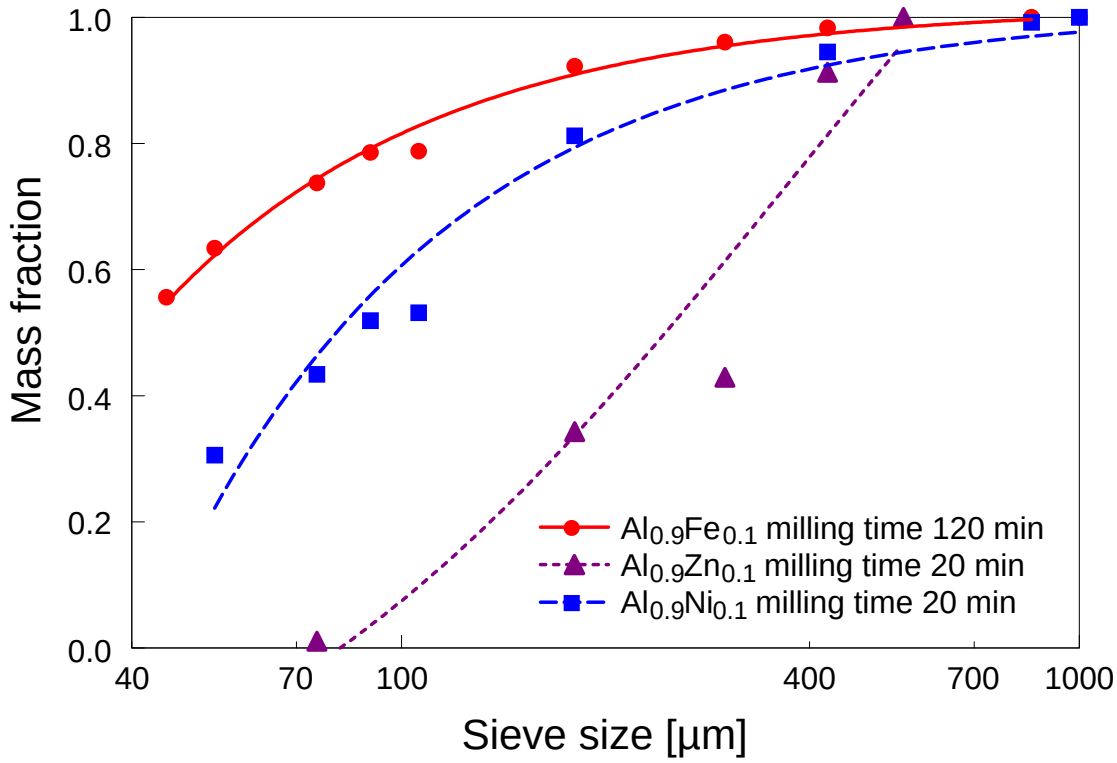

Figure 2.3 Cumulative size distributions of composite powders.

Backscattered SEM micrographs of cross-sections of the prepared materials are shown in Figure 2.4. All images show a gray Al matrix with light areas corresponding to inclusions of the metal additives or Al_2O_3, for the reference sample. The dark background is epoxy. All images were taken at the same magnification except for a magnified view of a rectangular Al-Fe particle. Consistent with the images shown in Figure 2.1, cross-sectioned particles of Al-Ni and Al-Zn composites appear as thin platelets (flakes), while Al-Fe particles are equiaxial.

The phase contrast in the reference $Al{\cdot}Al_2O_3$ samples is unexpected. It likely indicates that the discernable inclusions represent multiple 100-nm sized Al_2O_3 particles, which due to their small size appear brighter than the surrounding Al matrix.

In the Al-Fe sample, a large particle with a distinct shape is highlighted. Looking closer at this particle, it is observed that the particle shape is typical for a ball-milled material, in which the powder was compacted into platelets pressed between milling tools, which were broken apart due to continuing milling. This particle also shows that the Al and Fe are mixed quite homogeneously. The inclusions in this system are formed in both micron and sub-micron size ranges.

Both Zn and Ni inclusions (Figure 2.4 bottom left and right, respectively) are generally coarser than Fe inclusions. This is due to the shorter milling time, required to avoid formation of the intermetallic phases.

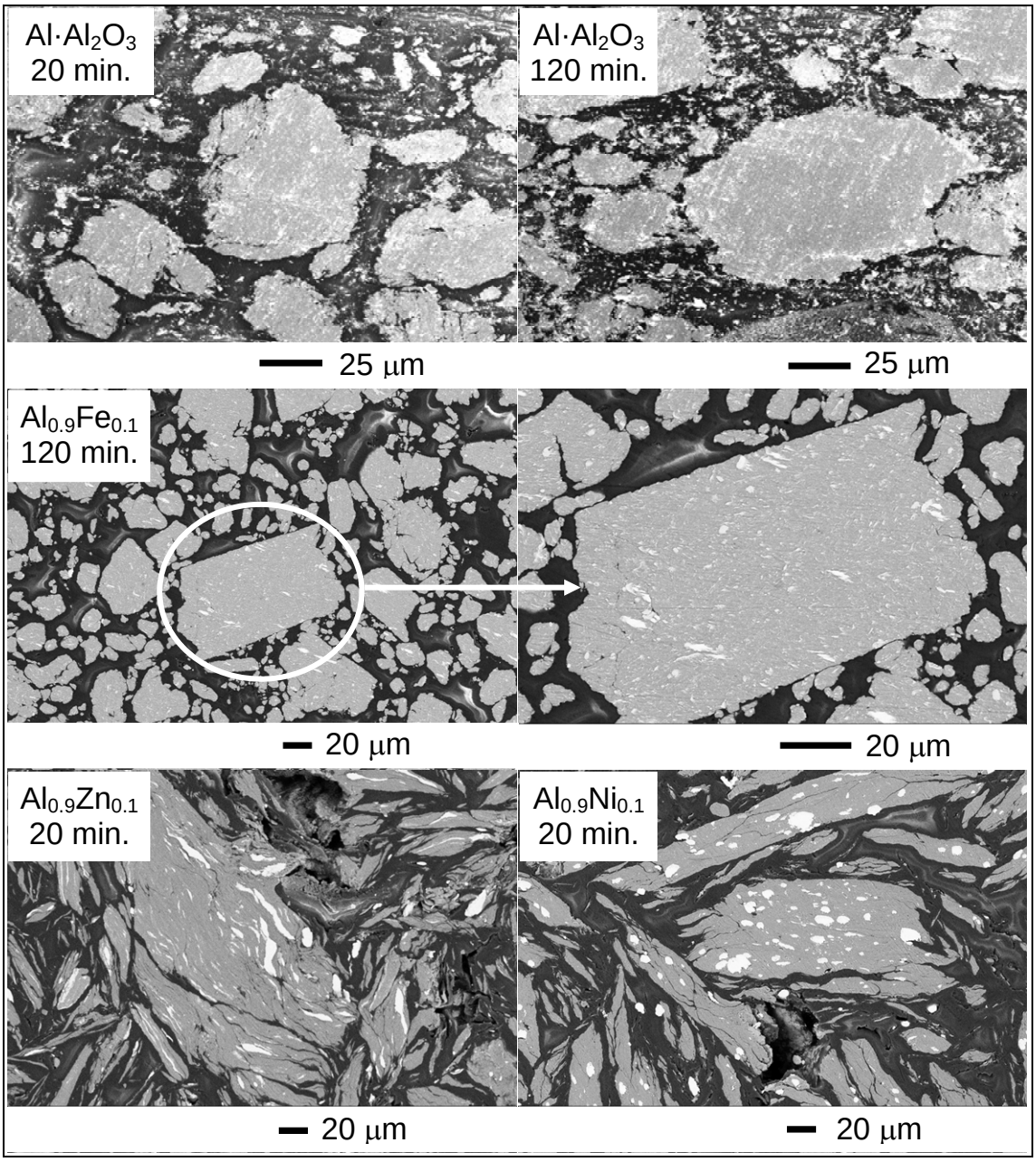

Figure 2.4 Backscattered SEM micrographs of cross-sections of the as-milled composite materials.

2.4.2 Phase Identification

Figure 2.5 shows the XRD patterns of the milled composite materials. Solid lines represent samples prepared with shorter milling times and dashed lines are for the

samples with extended milling times. The patterns are shifted vertically for clarity. As expected, strong Al peaks were measured for each of the materials as indicated by the vertical dashed lines in Figure 2.5. XRD patterns for the $Al{\cdot}Al_2O_3$ composite materials show peaks of Al and α-Al_2O_3 only. Peaks of Fe overlap with Al peaks for Al-Fe composites. The elemental metal additives Zn and Ni were clearly detected in respective composite powders prepared with short milling times. No reaction products (alloys or compounds) were detected. XRD patterns of the powders prepared with extended milling times generally show broader peaks, indicative of a smaller crystallite size. For Al-Fe, the XRD peak patterns are qualitatively similar for different milling times. For Al-Ni, the relative intensity of Ni peaks is clearly reduced for the sample prepared with a longer milling time. For the Al-Zn material prepared by 120 min milling, the XRD pattern shows that the elemental Zn peaks effectively disappeared.

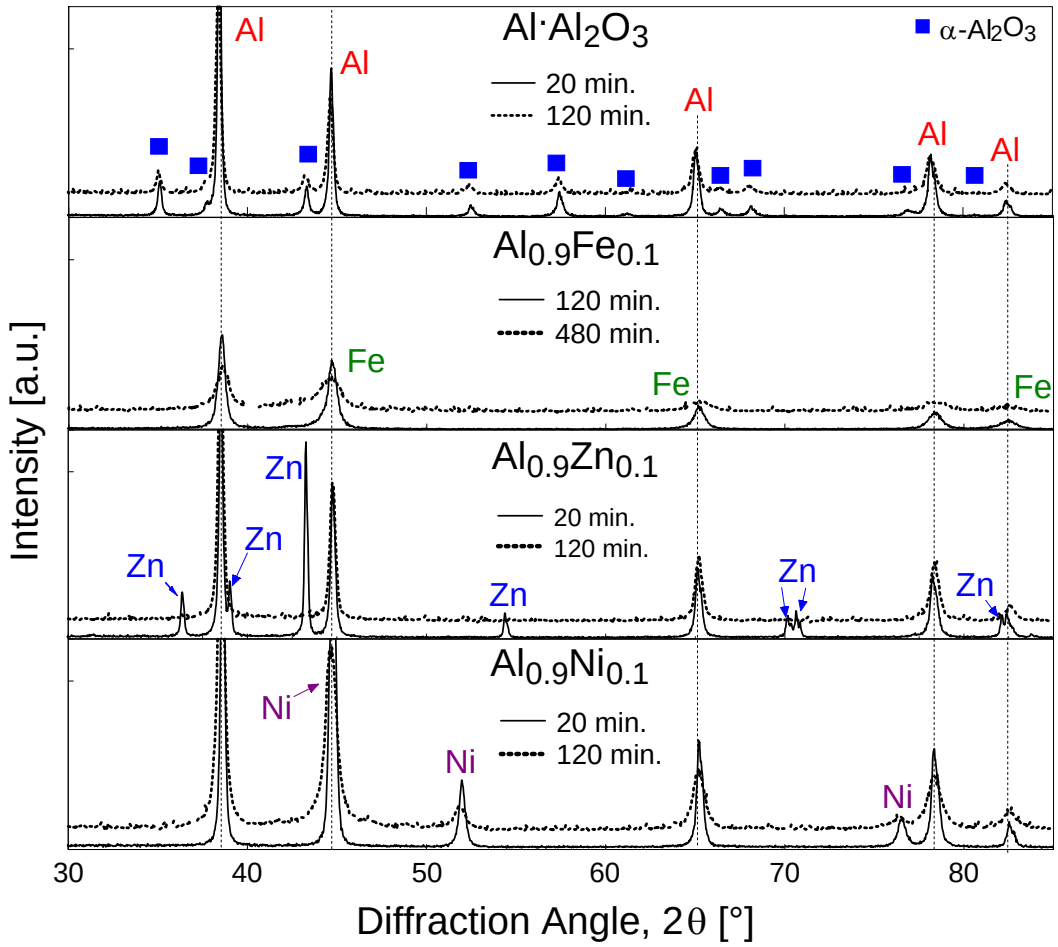

Figure 2.5 XRD patterns of the composite materials prepared using shorter (solid lines) and longer (dotted lines) milling time.

2.4.3 Thermal Analysis

Results of oxidation experiments for composite powders using DSC/TGA are shown in Figure 2.6. In addition, the TGA oxidation curves measured for the samples prepared with extended milling times are shown. DSC measurements taken over a broad range of temperatures exhibited a non-linear baseline and the data shown in Figure 2.6 were additionally processed to remove that effect. For the additional processing, portions of the DSC signal were identified for which no significant reactions could be detected. This

reaction identification was made using both DSC and TGA signals, considering the absence of clear peaks in either *dm/dT* or DSC curves. A polynomial fit was produced to pass through the "reaction-free" portions of the DSC signal and used as a baseline subtracted from the measured signal consistently. Because the "reaction-free" regions were difficult to identify at higher temperatures, the constructed baseline became more and more tentative as the temperature increased. Respectively, shown in Figure 2.6 are only portions of the DSC curves for which the baseline is identified reasonably well. The TGA baseline was flat after the initial heating period, but it was poorly defined at low temperatures. Respectively, TGA signals are also shown for the temperature ranges for which the baseline could be defined reasonably well.

Prior to any detected mass changes, the DSC traces for the Al-Fe and Al-Ni composites exhibit small but clearly distinguishable exothermic peaks at low temperatures: between 200 and 400 ºC for both materials. Respective portions of DSC curves between 100 and 500 ºC are magnified and shown as insets in Figure 2.6. These sub-solidus reactions are not associated with oxidation and represent the formation of intermetallic phases, as confirmed by XRD (see below). Similar exothermic events are not detectable in the Al-Zn curves; rather, a stepwise change in the heat release rate is observed in the measured DSC traces at about 390-420 ºC corresponding to the Al-Zn eutectic [44].

Two strong exothermic peaks correlating with the step-wise increases in the sample weight are observed in DSC signals for all materials. The two exothermic peaks occurring at about 600 and 950 ºC for appear to be qualitatively similar for all composites milled for 20 min (Al-Ni, Al-Zn, and $Al \cdot Al_2O_3$). The energy release values for both

peaks are comparable to each other, and the first peak appears a bit sharper than the second one. The first oxidation peak observed for all 20-min milled samples occurs substantially earlier and is substantially stronger than that observed previously for oxidation of spherical Al powders [45, 46].

For all composites milled for 120 min, the first oxidation exotherm occurs at a higher temperature, with the peak position close to 680 ºC (concurrently with the corresponding weight increase observed in TGA.) This onset temperature is higher than that observed for oxidation of spherical Al powders [45, 46]. For all Al-metal composites, this first oxidation peak becomes substantially smaller than the second exothermic peak at longer milling times while for the reference $Al{\cdot}Al_2O_3$ composite, the two exothermic peaks remain comparable to each other. The temperature range at which the second exothermic peak occurs is the same for all materials prepared at different milling times.

The DSC curve for the Al-Fe composite clearly shows Al melting preceding the first oxidation step. However, the melting is not detected for Al-Zn and is barely detectable for the Al-Ni composite, for which the melting peaks overlap with the strong exothermic peaks caused by oxidation. The melting peak is not detected for the $Al{\cdot}Al_2O_3$ composite milled for 120 min (DSC trace is not shown in Figure 2.6), but is observed to occur after the first oxidation step for the $Al{\cdot}Al_2O_3$ composite milled for 20 min, similar to the 20-min milled Al-Ni composites.

TGA curves for all materials also show a third oxidation step at elevated temperatures; that step is spread over a broad temperature range and only appears to be completed for the Al-Ni and $Al{\cdot}Al_2O_3$ composites, for which the weight stabilizes before

the maximum temperature of 1495 ºC is reached. For other materials, the weight continues to increase. High-temperature portions of the DSC curves for Al-Fe and Al-Zn composites are not shown because of the ambiguity in defining the respective baselines, as discussed above.

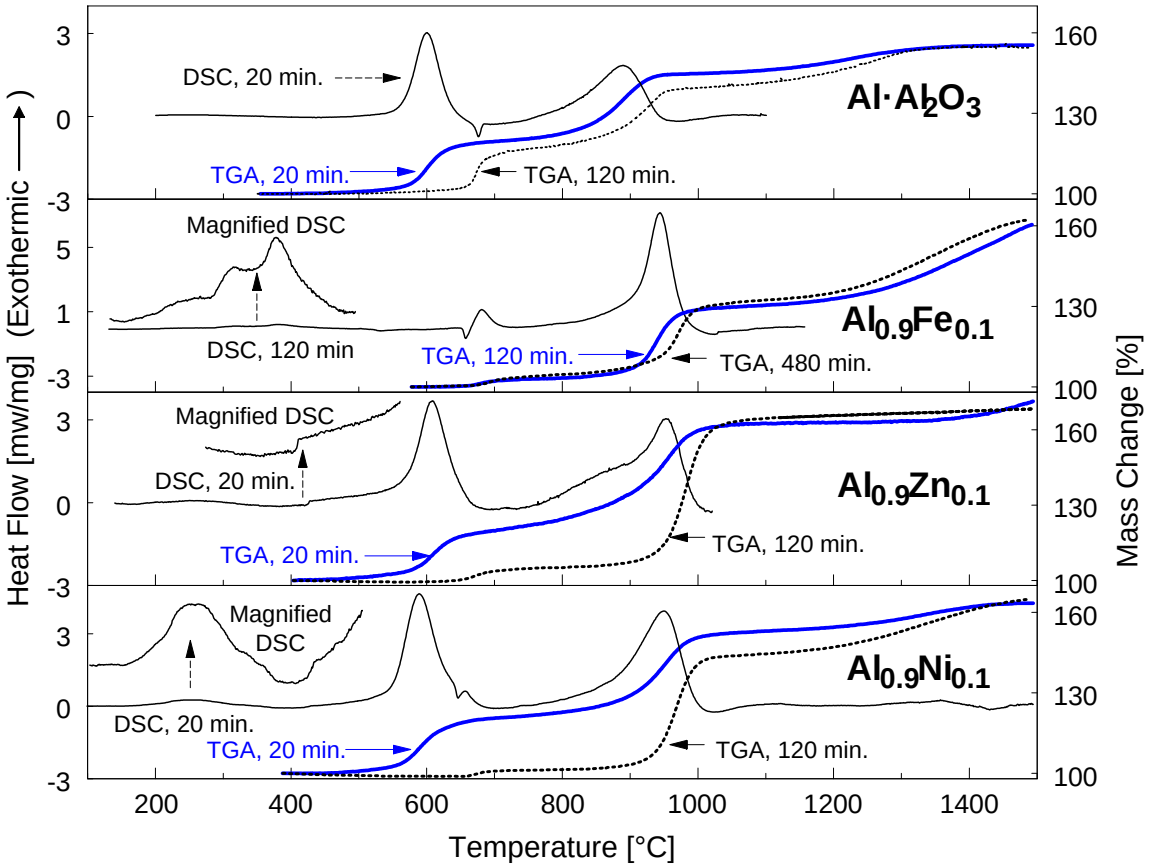

Figure 2.6 DSC/TGA plots showing heat flow and mass changes with respect to temperature for the prepared composites. Heating rate is 5 K/min for all experiments.

Oxidation kinetic data for the composites were obtained by a set of TGA measurements at varying heating rates of 5, 10, 20, and 40 K/min. For each system, the general trend shows a shift of oxidation steps to higher temperatures as the heating rate is increased. Apparent peak maxima of the derivative thermogravimetric (DTG) curves

were used in the isoconversion processing by the Kissinger method [36]. Individual activation energies for the first and second oxidation steps were determined and shown in Table 2.2.

Table 2.2 Activation Energies for Oxidation Stages of Prepared Composites

System	**Milling time, min**	**Activation Energy, E_a [kJ/mol]**	
		Oxidation Step I (Transformation from amorphous to γ-Al_2O_3)	Oxidation Step II (γ-phase growth)
$Al_{0.9}Fe_{0.1}$	120	290 ± 15	230 ± 12
$Al_{0.9}Zn_{0.1}$	20	420 ± 80	225 ± 35
$Al_{0.9}Ni_{0.1}$	20	320 ± 110	270 ± 30
$Al{\cdot}Al_2O_3$	20	270 ± 7	290 ± 6
	120	540 ± 80	330 ± 40
Al oxidation model [45, 47]		458	227

2.4.4 Compositions of Reacted and Partially Reacted Samples

Formation of various reaction products, including oxidized and intermetallic compounds, produced at different temperatures was investigated by SEM/EDX and XRD analyses of partially oxidized samples heated to and quenched from intermediate temperatures. Prior to quenching, all samples were heated at 5 K/min.

A set of XRD patterns of the as-milled and quenched samples recovered for the Al-Fe (120 min. milled) composite at different temperatures is shown in Figure 2.7. These analyses were particularly focused on initial exothermic reactions, expected to be important for interpretation of ignition mechanisms in such materials. SEM images and EDX spectra of both as-milled and low-temperature-quenched samples are also presented in Figures 2.8 and 2.9, respectively.

For the Al-Fe sample quenched at 710 °C, after the first oxidation step, aside from elemental metal peaks, new peaks present in the XRD pattern are those of $Al_{13}Fe_4$ and FeAl intermetallics. The sample recovered from 940 ºC was in the middle of the second oxidation step. At that temperature, peaks of $Al_{13}Fe_4$ intermetallic are still present, with peaks of α-Al_2O_3 and FeAl intermetallic also observed. For the sample heated to 1495 ºC, the only peaks present are those corresponding to α-Al_2O_3, FeAl alloy, and a ternary metal-oxide phase identified as $Fe_{1.5}Al_{0.5}O_3$.

Figure 2.8 shows SEM images for both, as-milled samples and samples quenched from 710 ºC. In the sample quenched at 710 ºC, Fe inclusions are no longer distinguishable, most likely due to mixing substantially enhanced by melted Al. No surface oxide layers or other oxygen-rich regions are detected in any of the quenched particles. EDX spectra corresponding to the images presented in Figure 2.8 and respective standardless composition analyses are shown in Figure 2.9. The spectra show a small, but clearly detectable increase in the oxygen concentration for the sample quenched from 710 ºC as compared to the as-milled material. It should be noted that the results of the EDX-based standardless composition analyses shown in Figure 2.9 and below for other materials, are only useful for semi-quantitative comparison of composition changes for similarly prepared samples; these analyses do not represent the actual materials' compositions.

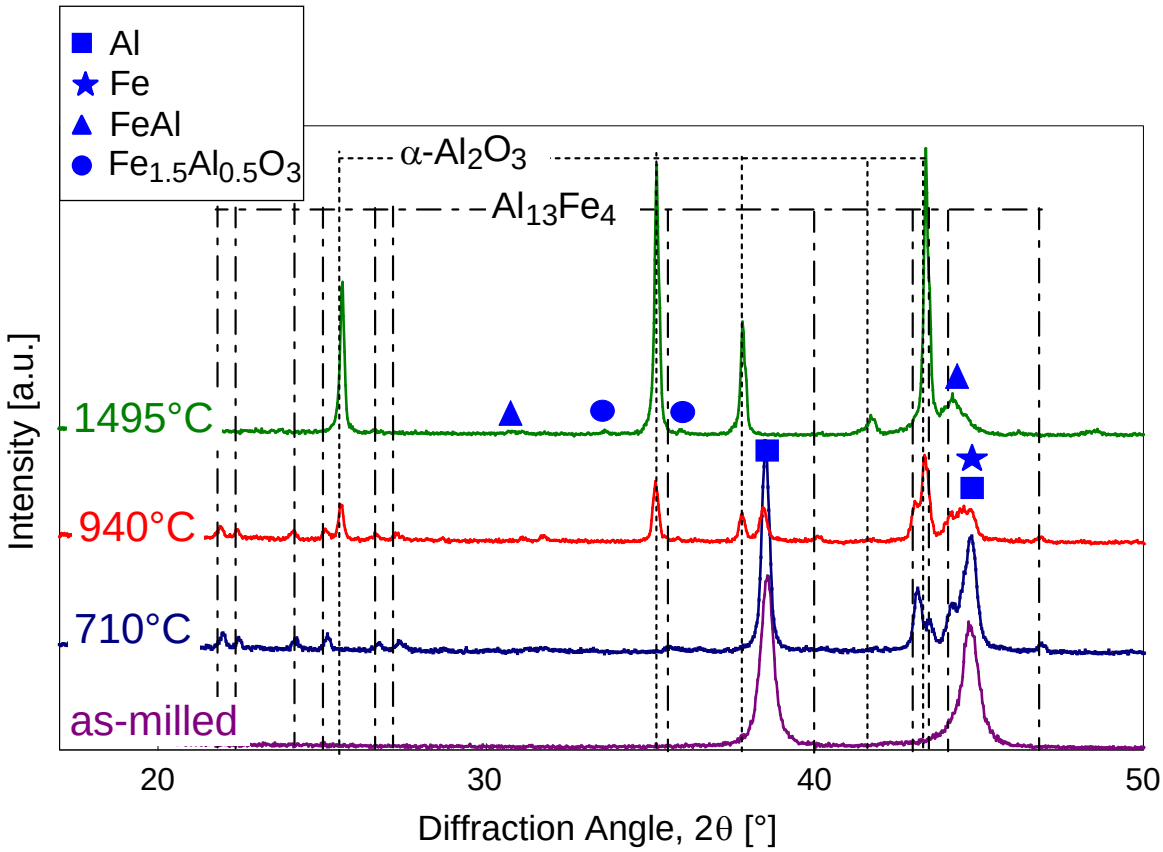

Figure 2.7 XRD patterns of the as-milled and quenched $Al_{0.9}Fe_{0.1}$ (120 min. milled) samples.

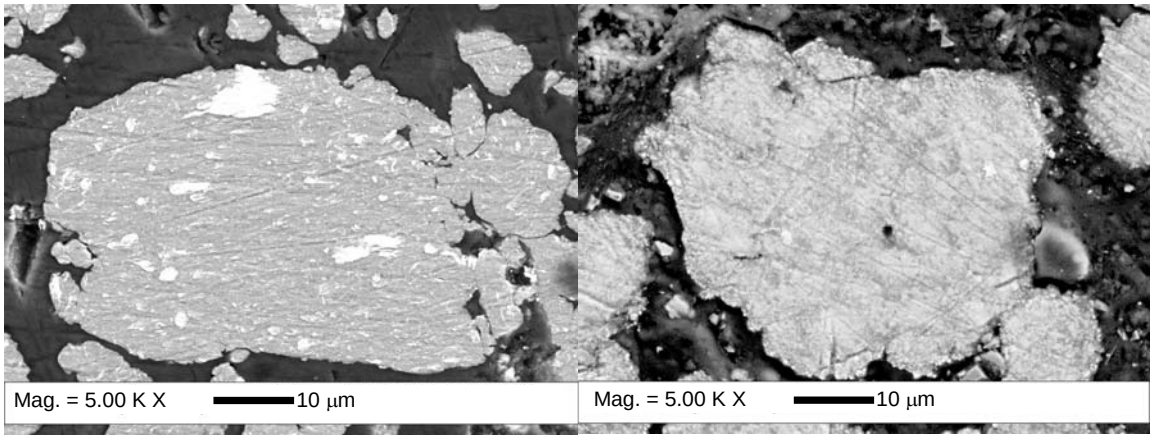

Figure 2.8 Backscattered SEM micrographs of cross-sections of the as-milled and quenched from 710 °C $Al_{0.9}Fe_{0.1}$ (120 min. milled) samples.

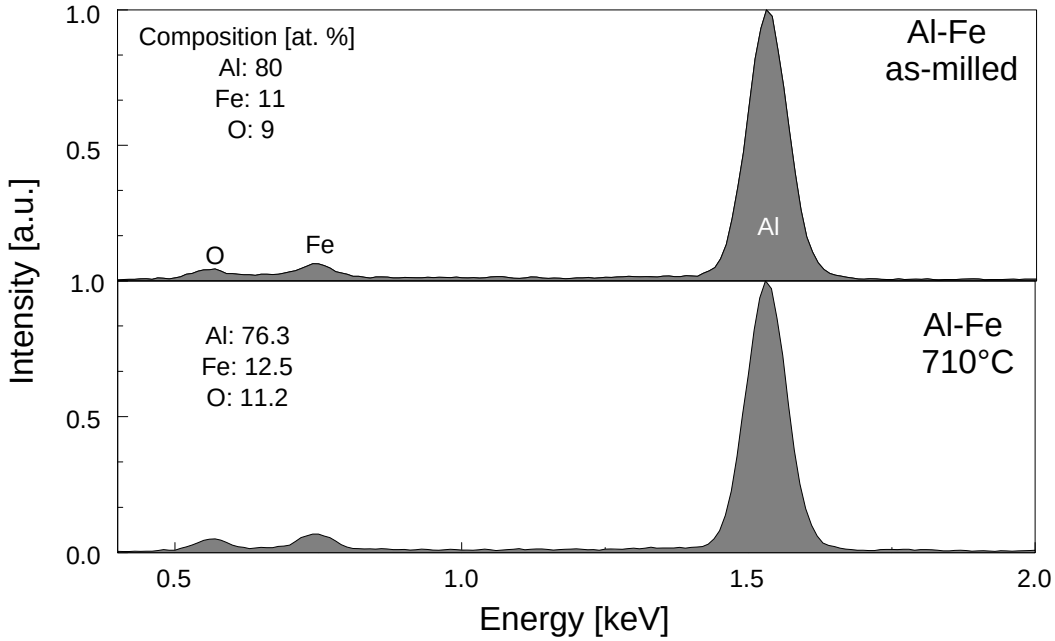

Figure 2.9 EDX spectra and inferred elemental compositions of the as-milled and quenched from 710 °C $Al_{0.9}Fe_{0.1}$ (120 min. milled) samples.

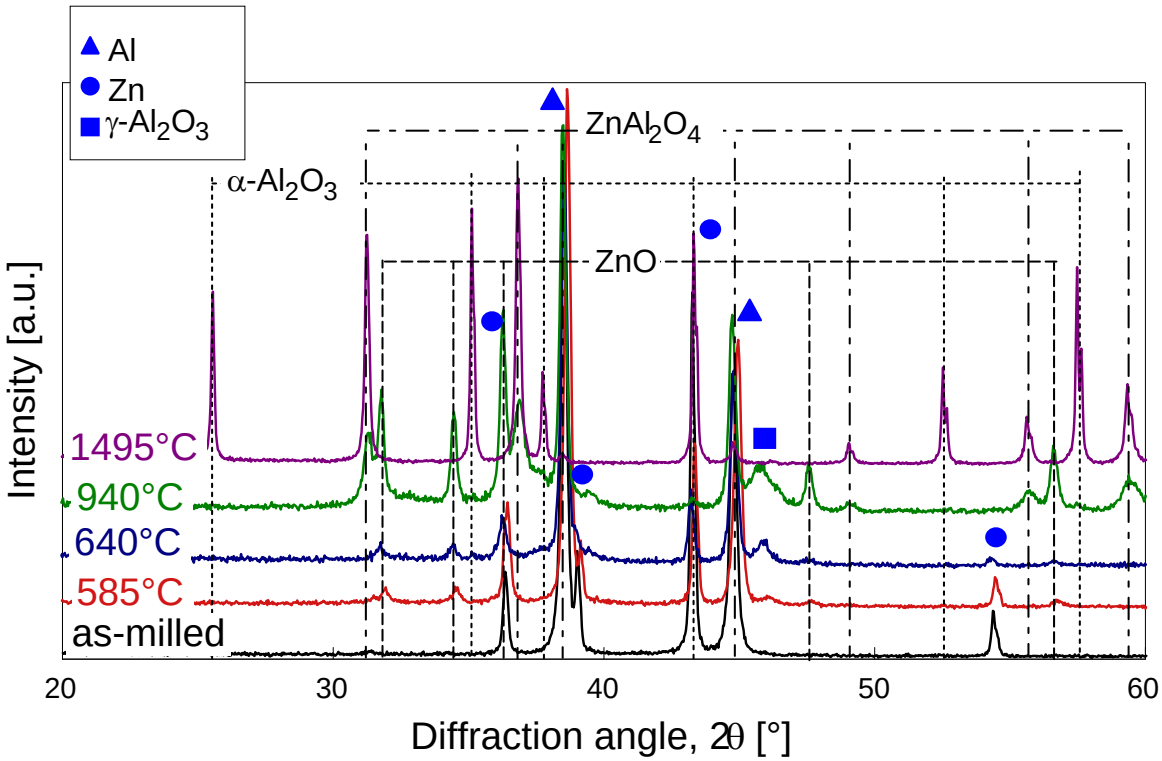

Figure 2.10 XRD patterns of the as-milled and quenched $Al_{0.9}Zn_{0.1}$ (20 min. milled) samples.

A set of XRD patterns for as-milled and quenched samples recovered for the 20-min. milled Al-Zn composite at different temperatures is shown in Figure 2.10. SEM images and EDX elemental maps/spectra of as-milled and low-temperature-quenched samples are presented in Figures 2.11 and 2.12, respectively. For the sample quenched at 585 °C, following the initial mass increase, the most significant new peaks in the XRD pattern are those of ZnO and γ-Al_2O_3. By the end of the first oxidation step, for the sample quenched at 640 ºC, the peaks of ZnO and γ-Al_2O_3 become stronger. At 940 °C, towards the end of the second oxidation step, the strongest peaks for α-Al_2O_3 become visible. For the sample heated to 1495 ºC, ZnO and γ-Al_2O_3 peaks disappear and the pattern of the ternary oxide phase $ZnAl_2O_4$ appears instead. This spinel and α-Al_2O_3 are the only two distinguishable phases at this temperature.

From Figure 2.11, it is clear that after heating, zinc is more uniformly distributed in the particle volume. According to the Al-Zn phase diagram, material with a bulk composition of 10 at. % Zn should consist of a single phase between ~250 °C and the solidus temperature of ~590 °C, and of two phases below ~250 °C. The compositional variation observed in the quenched sample in Figure 2.12 could come from the decomposition of the homogeneous material when it is cooled below ~250 °C. However, the alignment of the Zn-rich regions with the lamellar texture of the material suggests that the original Zn inclusions did not homogenize completely on the time scale of the DSC experiment. Therefore, the Zn-rich regions indicate the continuous presence of a Zn-rich melt. This presence of the melt is in distinct contrast to what is expected to occur in the material milled for 2 hours, where all Zn is dissolved into the Al phase after milling at room temperature.

In Figure 2.11, marker 1 indicates a bright Zn inclusion, and marker 2 indicates gray Al matrix embedded in the dark epoxy background. Elemental maps show that for the as-milled sample, oxygen concentration is relatively uniform within the sample volume. In fact, based on the oxygen map it is virtually impossible to distinguish between the as-milled sample and surrounding epoxy. In the sample quenched at 585 ºC, oxygen concentration is markedly increased in the Al matrix, and the sample/epoxy boundaries become apparent in the respective oxygen map. However, the oxygen increase is not apparent in or at the boundaries of the Zn inclusions. In agreement with the elemental maps, the EDX spectra for the as-milled and quenched samples presented in Figure 2.12 confirm a noticeable increase in the oxygen concentration in the heated and quenched sample.

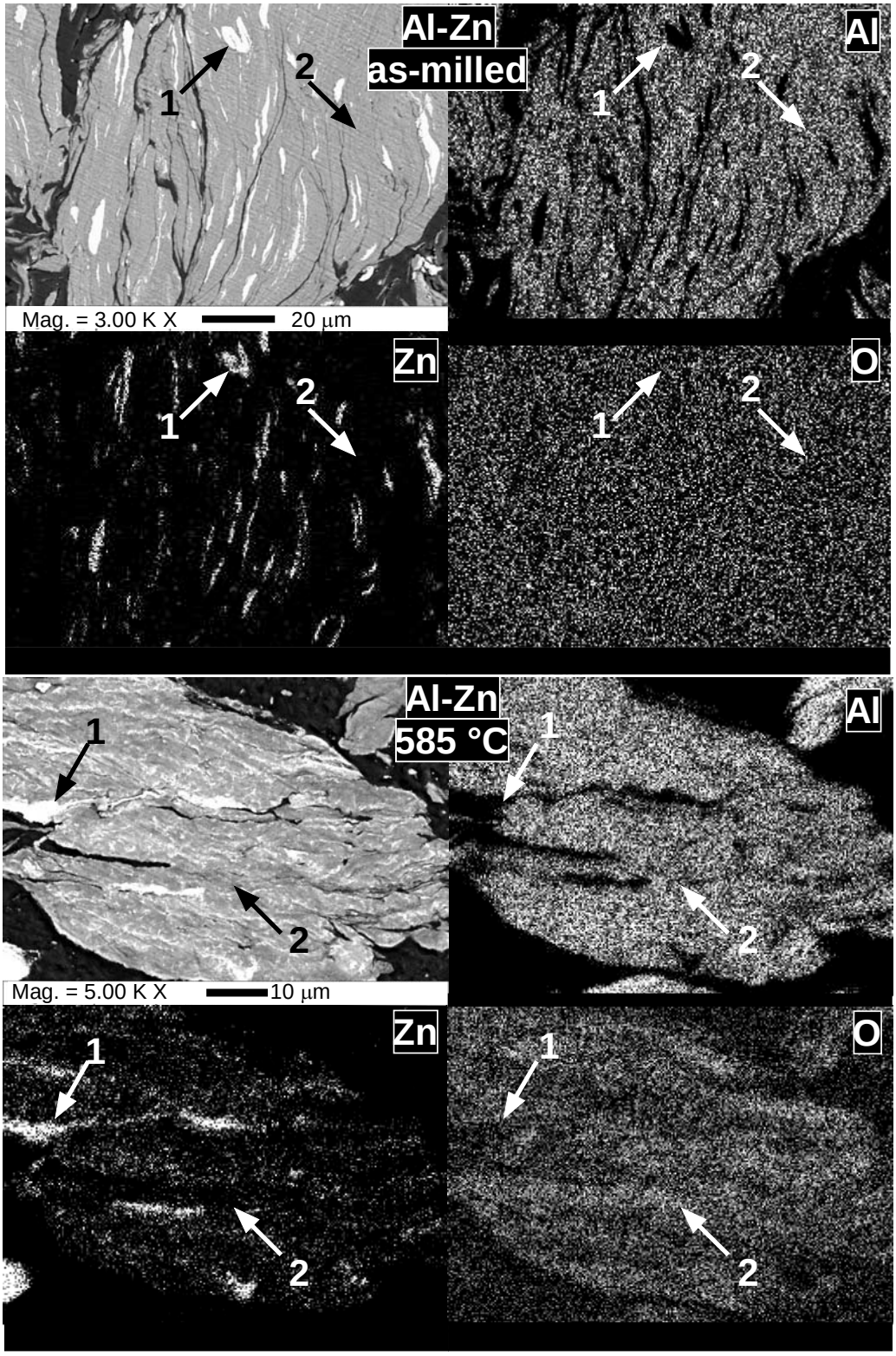

Figure 2.11 EDX maps of the as-milled and quenched from 585°C $Al_{0.9}Zn_{0.1}$ (20 min. milled) samples.

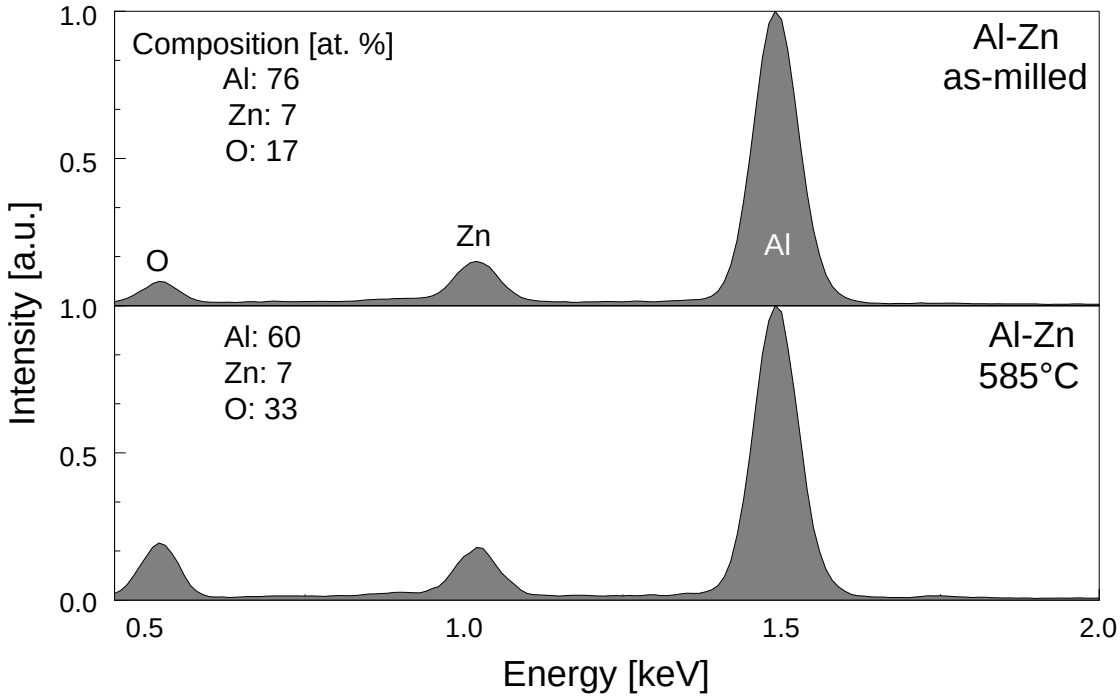

Figure 2.12 EDX spectra and inferred elemental compositions of the as-milled and quenched from 585°C $Al_{0.9}Zn_{0.1}$ (20 min. milled) samples.

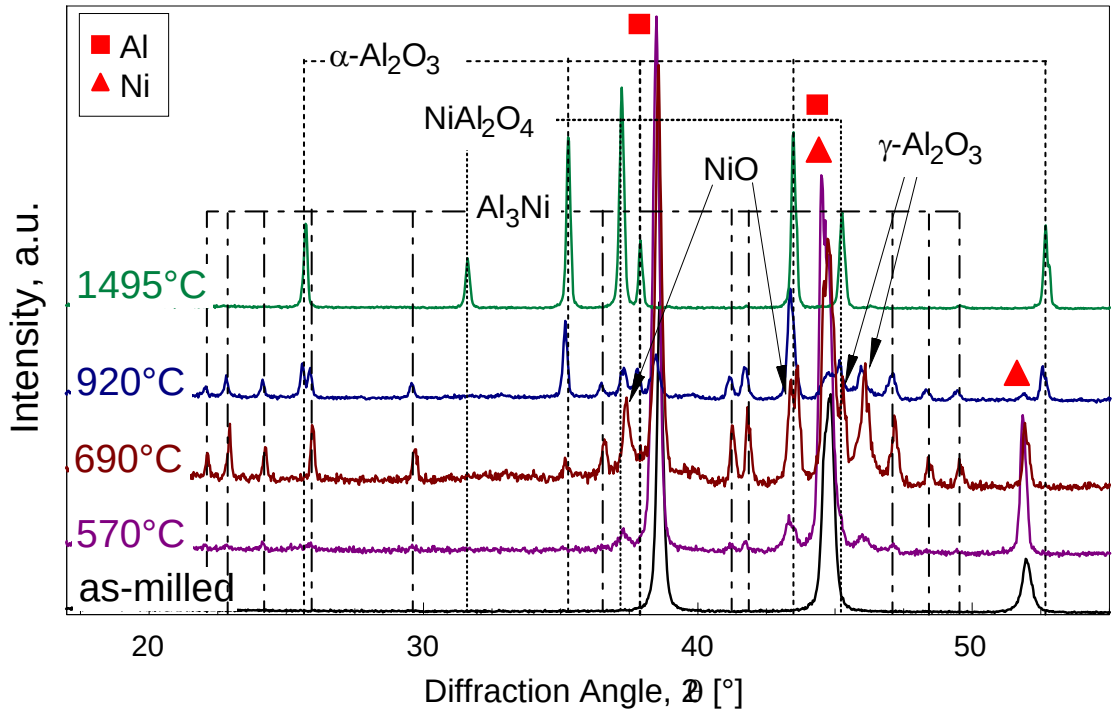

Figure 2.13 XRD patterns of quenched $Al_{0.9}Ni_{0.1}$ (20 min. milled) samples.

A set of XRD patterns of 20-min. milled Al-Ni composites recovered from different temperatures is shown in Figure 2.13. SEM images and EDX elemental maps/spectra of as-milled and low-temperature-quenched samples are presented in Figures 2.14 and 2.15, respectively. For the sample quenched at 570 °C, following the initial mass increase, the most significant new peaks in the XRD pattern are those of NiO. In addition, intermetallic Al_3Ni and traces of γ-Al_2O_3 are detected. By the end of the first oxidation step, for the sample quenched at 690 ºC, the peaks of NiO and γ-Al_2O_3 are noticeably stronger, while the strongest peak for α-Al_2O_3 is also visible. The sample recovered from 920 ºC was at the beginning of the second oxidation step; it contains Al_3Ni alloy, NiO, and γ- and α-Al_2O_3. For the sample heated to 1495 ºC, NiO peaks disappear and the pattern of the ternary oxide phase $NiAl_2O_4$ appears instead. $NiAl_2O_4$ and α-Al_2O_3 are the only two distinguishable phases in the XRD patterns.

Similar to Figure 2.11, in the images and elemental maps shown in Figure 2.14, marker 1 points to a bright Ni inclusion and marker 2 points to the darker Al matrix embedded in epoxy. In the as-milled sample in Figure 2.14, the oxygen map indicates no apparent difference in the oxygen concentration in Al matrix or Ni inclusions, similar to that seen in Figure 2.11 for Al-Zn composites. However, it is apparent that in the sample quenched from 570 ºC, oxygen is preferentially concentrated in the Al-rich regions. The EDX spectra for the as milled and heated/quenched samples (Figure 2.15) show an overall increase in the oxygen concentration, as would be expected from the appearance of the elemental maps. A summary of phases detected by XRD is shown in Table 2.3 for all composite systems.

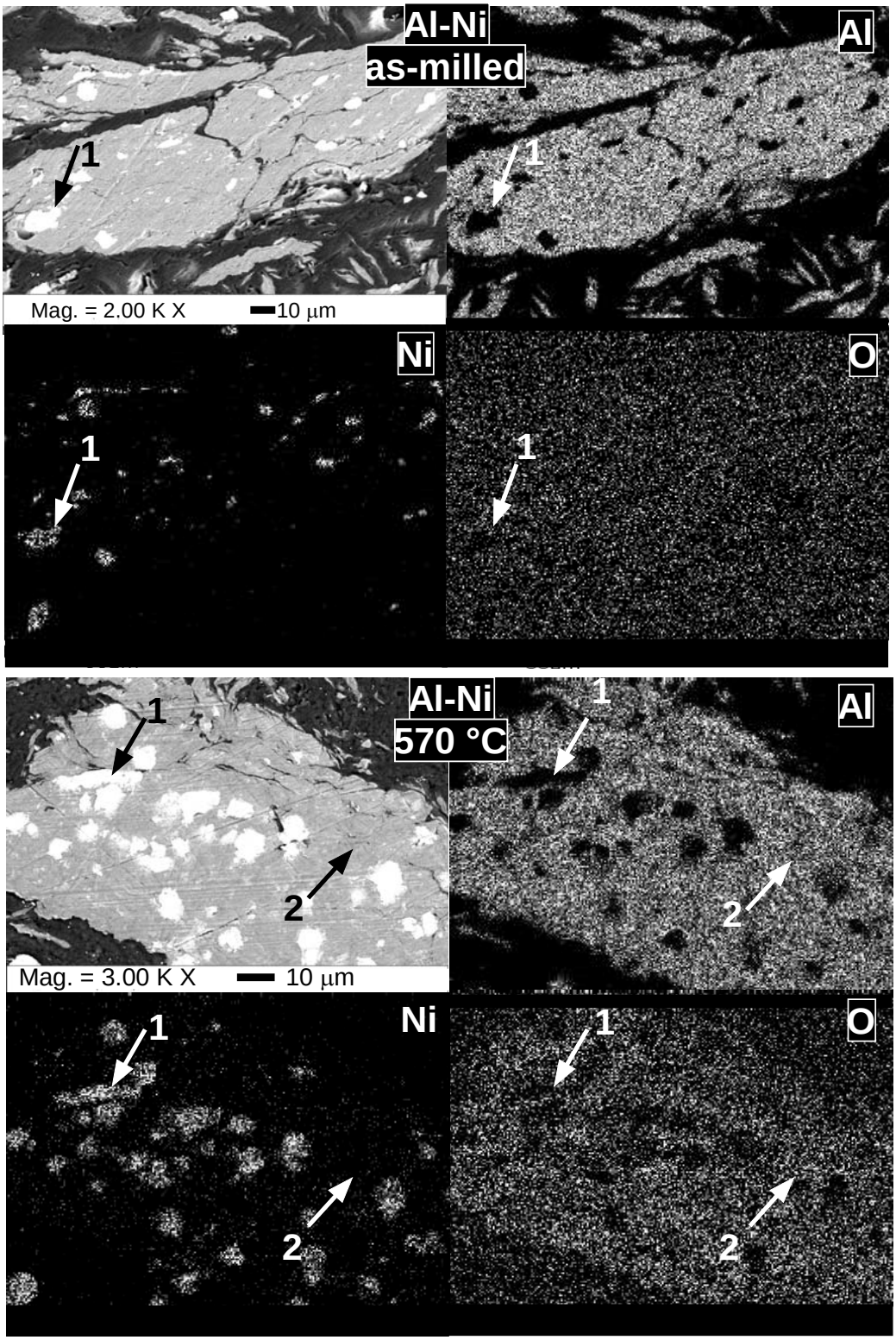

Figure 2.14 EDX maps of the as-milled and quenched from 570°C $Al_{0.9}Ni_{0.1}$ (20 min. milled) samples.

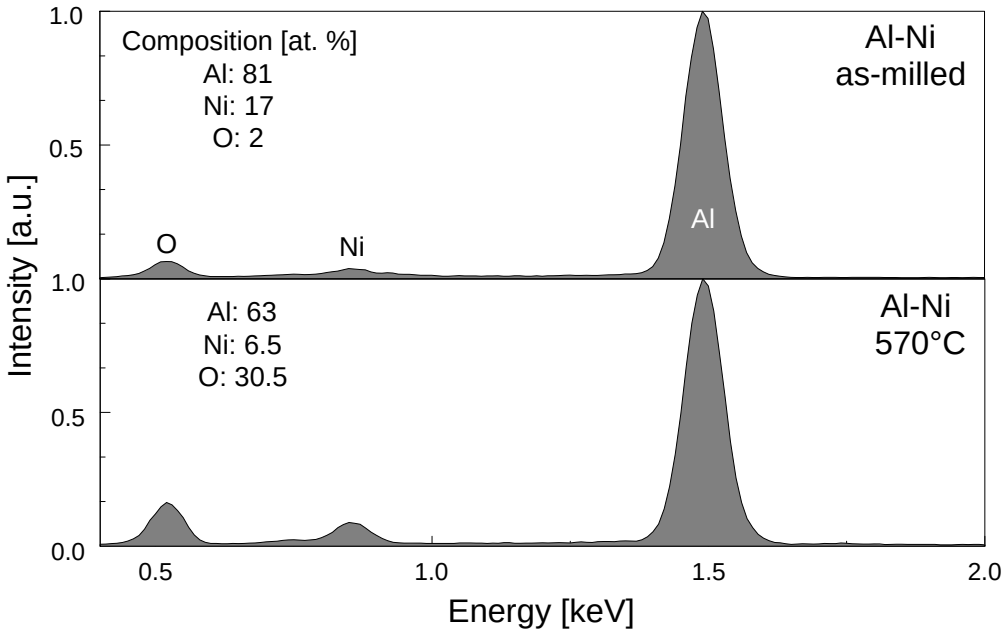

Figure 2.15 EDX spectra and inferred compositions of the as-milled and quenched from 570°C $Al_{0.9}Ni_{0.1}$ (20 min. milled) samples.

Table 2.3 Summary of Phases Detected Using XRD and EDX in Composite Materials Heated in Ar/O_2 Flow to and Recovered from Different Temperatures

Quenching/recovery temperature [°C]	Phases detected by XRD
$Al_{0.9}Fe_{0.1}$ (120 min milled)	
710	Al, Fe, $Al_{13}Fe_4$, FeAl
940	Al, Fe, $Al_{13}Fe_4$, FeAl, α-Al_2O_3
1495	FeAl, α-Al_2O_3, $Fe_{1.5}Al_{0.5}O_3$
$Al_{0.9}Zn_{0.1}$ (20 min milled)	
585	Al, Zn, ZnO, γ-Al_2O_3
640	Al, Zn, ZnO, γ-Al_2O_3, α-Al_2O_3
940	Al, Zn, ZnO, γ-Al_2O_3, α-Al_2O_3, $ZnAl_2O_4$
1495	α-Al_2O_3, $ZnAl_2O_4$
$Al_{0.9}Ni_{0.1}$ (20 min milled)	
570	Al, Ni, NiO, Al_3Ni, γ-Al_2O_3,
690	Al, Ni, NiO, Al_3Ni, γ-Al_2O_3, α-Al_2O_3
920	Al, Ni, NiO, Al_3Ni, γ-Al_2O_3, α-Al_2O_3
1495	α-Al_2O_3, $NiAl_2O_4$

2.4.5 Ignition Testing

Because of the relatively large particle sizes of the composite powders, thin coatings on the electrically heated filament could not be obtained without preliminary size classification of the powders. The composite powders were therefore size-classified prior to the ignition tests. The size fractions of Al-Fe, Al-Zn, and Al-Ni composite powders used for ignition experiments were passed through sieves with opening sizes of 43, 57, and 180 μm, respectively. It was confirmed by XRD analysis that the size classified samples have the same phase compositions as the starting powders. Note that ignition was not observed in experiments with any size-classified $Al{\cdot}Al_2O_3$ composite powders.

A set of typical photodiode traces recorded in ignition experiments is shown in Figure 2.16. In addition, a set of traces recorded during heating of an uncoated "blank" filament is also shown for comparison. The temperature profiles shown are obtained using linear extrapolation of the temperature ramp recorded in each experiment by the pyrometer within its calibration range of 600 – 930 ºC. This linear extrapolation is supported by calculations of the filament temperature based on the applied voltage, the impedance of the filament-containing circuit, and heat transfer between the filament and the surrounding air [43]. It remains valid while the radiation heat losses from the filament are substantially smaller than convection. Repeated experiments showed slight variations in the temperature ramp due to minor changes in the filament resistance and a somewhat varied battery capacity (as it discharges during experimentation), although the same initial settings were used.

Initially, the recorded photodiode traces show an increase in amplitude, typical for radiation of a gray body with a linearly increasing temperature. For the blank filament,

the initial rise in the photodiode signal continues until either the signal becomes saturated (as seen in Figure 2.16), or the filament melts and breaks apart. For the coated filament, the moment of powder ignition is associated with a sudden rise in the emission intensity. As shown in Figure 2.16, time derivatives of the photodiode traces were calculated to better identify this ignition moment. Note that the initial increase in the photodiode signal for the coated filament (with coating of $Al_{0.9}Fe_{0.1}$ shown in Figure 2.16), is delayed compared to that of the blank filament; this delay is due to the lower emissivity of the powder coating compared to the uncoated filament surface.

Once powders are ignited, the photodiode signal becomes saturated; therefore, the only useful data extracted from these experiments are the ignition moment and respective ignition temperature.

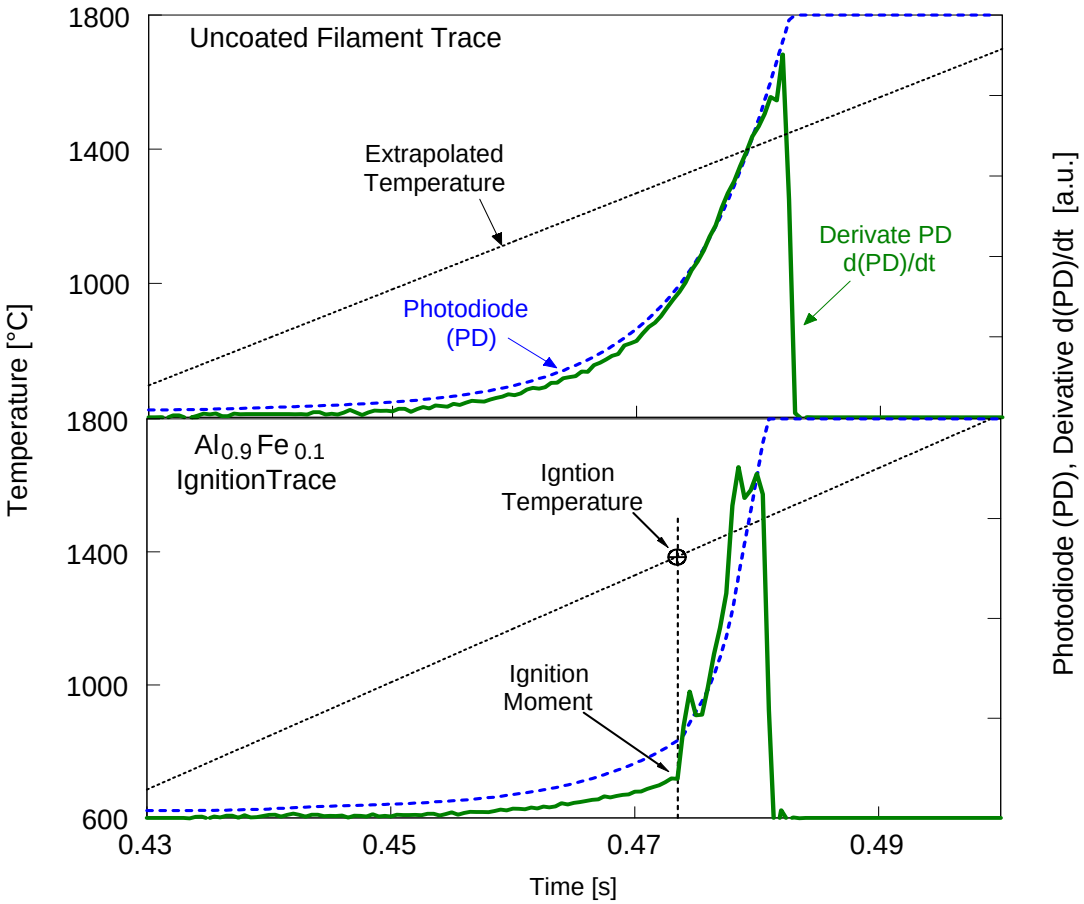

Figure 2.16 Ignition traces showing temperature, photodiode voltage, and its time-derivative for a powder-coated filament (bottom) and a blank filament (top).

Processing the data extracted from ignition experiments yields a plot of ignition temperature versus heating rate shown in Figure 2.17. For the range of heating rates tested, all composites ignited in a relatively narrow temperature range. At lower heating rates, the powders ignited at about 1006 K (733 °C), while at higher heating rates, the powders ignited at about 1065 K (792 °C). All composites ignite at the temperatures much lower than those observed for pure Al powders (10-14 μm nominal size), which ignited in the temperature range of 1800 - 1900 K for heating rates varied from about 200 to 8000 K/s [48]. The $Al{\cdot}Al_2O_3$ composite powders could not be ignited in the temperature range covered by the current experimental configuration.

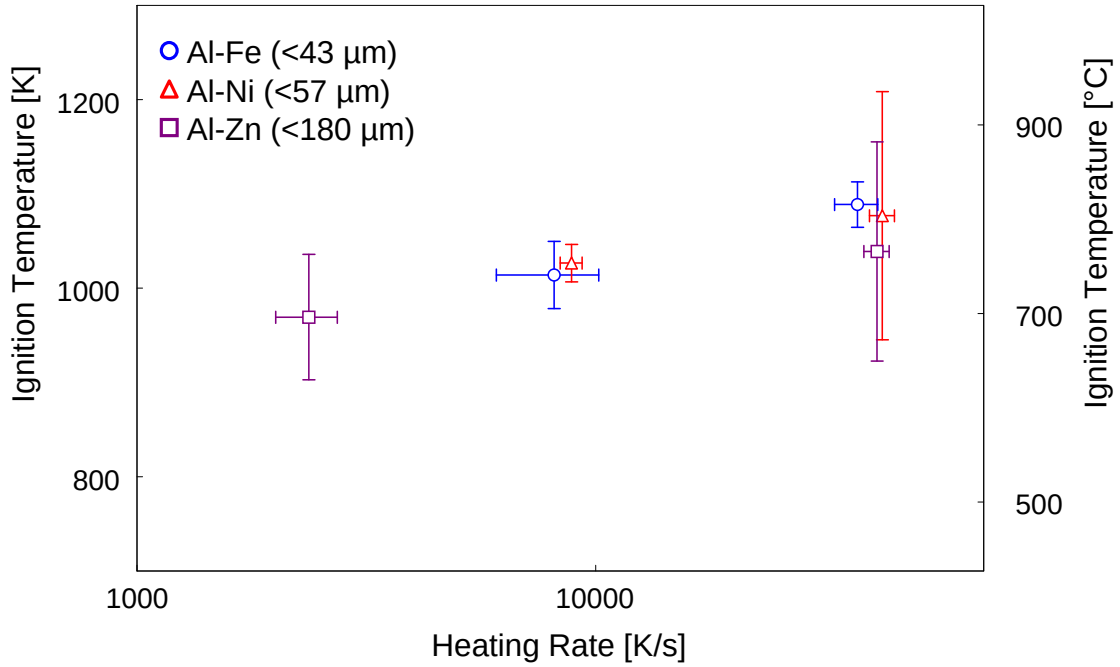

Figure 2.17 Ignition temperature versus heating rate for prepared composites of Al-Fe (120 min. milled) and Al-Zn and Al-Ni (both 20 min. milled).

2.5 Discussion

2.5.1 Sample Morphology and Phases

For Al-Zn and Al-Ni systems, only very short milling times (20 min.) resulted in the preparation of composite materials. Those composites, similarly to the 20-min milled $Al{\cdot}Al_2O_3$ composites, exhibited accelerated low-temperature oxidation kinetics as compared to a much finer, unmilled spherical aluminum powder [45, 46]. All 20-min milled powders had flake-like particle shapes. However, the flake aspect ratios were substantially closer to equiaxed than for conventional ~ 100-nm thick Al flakes used in pyrotechnic mixtures, as considered in earlier Al oxidation studies [47], in which low-temperature oxidation steps for Al flakes were also substantially higher than for spherical Al.

For Al-Zn and Al-Ni, longer milling times cause formation of homogeneous intermetallic phases; for $Al{\cdot}Al_2O_3$ composites, longer milling time results primarily in reduced dimensions of Al_2O_3 inclusions. For all materials prepared with longer milling times, particle shapes became more equiaxed and the low-temperature oxidation rates were substantially reduced.

The current results impose a limitation on mechanical milling as a manufacturing method for Al-based metal-metal composites, specifically suggesting that finer composite powders that might be of interest for practical applications cannot be obtained without simultaneously forming undesirable intermetallic and relatively unreactive phases. On the other hand, materials prepared by short milling times may be directly useful for preparation of consolidated reactive material components and structures, and as additives to various energetic formulations.

2.5.2 Reaction Mechanisms and Kinetics

Qualitatively, oxidation steps observed for the composite powders are similar to those observed for pure aluminum. However, reaction mechanisms may be substantially different. It should be noted first that the significant increase in the first oxidation step for all composite materials is hardly explained by the increase in the external particle surface, especially comparing the present TGA curves for the coarse composites with those for commercial, fine 1-5 μm Al powder [45]. However, similar strong initial oxidation steps observed for all 20-min milled samples, including the $Al{\cdot}Al_2O_3$ composites indicate the crucial role of the material morphology altered by ball milling. In particular, it is suggested that a developed grain boundary network that is not well distinguished in the present SEM images is rapidly formed when Al is ball-milled with an

additive. This grain boundary network results in a substantial increase of the Al surface available for oxidation at low temperatures, explaining the observed accelerated low-temperature oxidation. It is interesting that despite substantially increased low-temperature oxidation rates, $Al{\cdot}Al_2O_3$ composites fail to ignite when being rapidly heated, unlike 20-min milled Al-metal composite powders. Thus, it is concluded that low-temperature oxidation processes detected and quantified in DSC/TGA experiments must be supplemented by additional reactions, occurring at higher heating rates in order to describe thermally initiated ignition of the present materials.

Selective oxidation of Zn and Ni visible from the slow increase in the sample mass preceding the first Al oxidation step (Figure 2.6) suggests a possible alteration of the reactive Al interfaces present in the composite materials. The continuous presence of a melt above the eutectic temperature of 382 °C in the Al-Zn system and intermetallic reactions in the Al-Ni and Al-Fe systems can also affect the Al surface and ensuing Al oxidation. Such reactions occurring at higher heating rates could be accompanied with stronger composition gradients and more significant change in the interface chemistry, resulting in an even higher Al oxidation rate, ultimately causing ignition.

A striking indication of the altered oxidation mechanism comes from the elemental maps showing oxygen distribution in the particles quenched after the first oxidation step. The uniform increase in the oxygen concentration in the entire volume of the Al matrix rather than on its surface or in or around Zn or Ni inclusions is unexpected based on the conventional Al oxidation models considering growth and evolution of the protective surface oxide film. Clearly, Al morphology modified by metal inclusions drastically changes the mechanism of oxygen transport to Al, as compared to the

unmilled Al powders. Further insight in the reaction mechanisms can be gained from analysis of the kinetic trends for the observed intermetallic, oxidation, and ignition reactions.

Derivatives of the TGA traces (DTG) were used to construct Kissinger plots [49] using the DTG peak maxima. The resulting Kissinger plots are shown in Figure 2.18 (and respective activation energies are shown in Table 2.2). The results of the filament ignition experiments at different heating rates are also shown in Figure 2.18 for comparison. For the ignition data, each point represents an average of multiple individual measurements. The vertical and horizontal error bars represent respective standard deviations in the heating rate and ignition temperature among experimental data points. It is interesting to consider an extrapolation of kinetic trends observed in the low-heating rate thermo-analytical measurements into the much higher heating rates used in ignition experiments, as shown in Figure 2.18. This extrapolation is only meaningful if the reactions are governed by the same processes in both types of experiments. While no data are available to directly validate such an assumption, it is instructive to examine whether there are correlations between kinetic trends observed in a wide range of heating rates.

The activation energies corresponding to the first and second Al oxidation steps were previously assigned to the polymorphic transformation of amorphous to γ-Al_2O_3 and to growth of γ-Al_2O_3, respectively [45, 47]. For all composites, the activation energy for the first oxidation step is noticeably reduced compared to that identified for pure Al; however, the difference in the activation energy for the second step is only marginal. Incidentally, as apparent from the comparison with the ignition points in Figure 2.18, the

second Al oxidation step is irrelevant for the ignition processes for all materials: at high heating rates it is expected to occur at much higher temperatures than the observed ignition. Thus, it is reasonable to conclude that the metal inclusions reduce the stability and/or protective properties of amorphous alumina, which are critical for the ignition (and, probably, aging) behavior of the respective Al-based powders.

Comparing kinetic trends more specifically, it is observed that for all the systems, the ignition data do not line up with the first oxidation step. Note, though, that the measured ignition temperatures are those of the filament, and not of the powder coating. Powder temperatures could be somewhat lower than those of the filament, suggesting that the ignition points in the Kissinger plot could shift to the right side in Figure 2.18, if corrected to represent the powder temperature. It is also interesting to compare the kinetic trends observed for intermetallic reactions and those for ignition. For Al-Fe, the points indicating the exothermic intermetallic reaction line up very well with the ignition points in Figure 2.18, indicating that formation of the intermetallic phases could contribute to the ignition of particles for this material. Also, for Al-Fe, the intermetallic reactions at higher heating rates are expected to occur at lower temperatures than the observed ignition. However, as noted above, correction for the difference between the powder and filament temperatures can shift ignition points to the right side, making the correlation between the intermetallic reactions and ignition better.

The mechanism of apparently volumetric oxidation of aluminum matrix observed at low temperatures based on the elemental oxygen maps (Figures 2.11 and 2.14) remains unclear. A developed grain boundary network facilitated by the metal inclusions most likely plays the key role in this accelerated low-temperature oxidation. One possibility is

that the oxygen is rapidly supplied to metal inclusion additives, which oxidize and then serve as oxygen donors to the surrounding aluminum. It is also possible that multiple, ultrafine inclusions of Zn and Ni are present inside the Al matrix but are not resolved in the present SEM images. Such inclusion network would create paths for greatly accelerated grain boundary diffusion of oxygen, while the selective oxidation of Al (and thus, relative stability of the metal additive inclusion network maintaining the oxygen diffusion) could be explained by its greater oxygen affinity (greater heat of oxidation). In addition, it must be assumed that no protective alumina film is formed at the Al-metal interfaces, unlike Al interface with gaseous oxidizers. Thus, the transport limitations on the oxidation mechanisms become secondary to the thermodynamic driving forces.

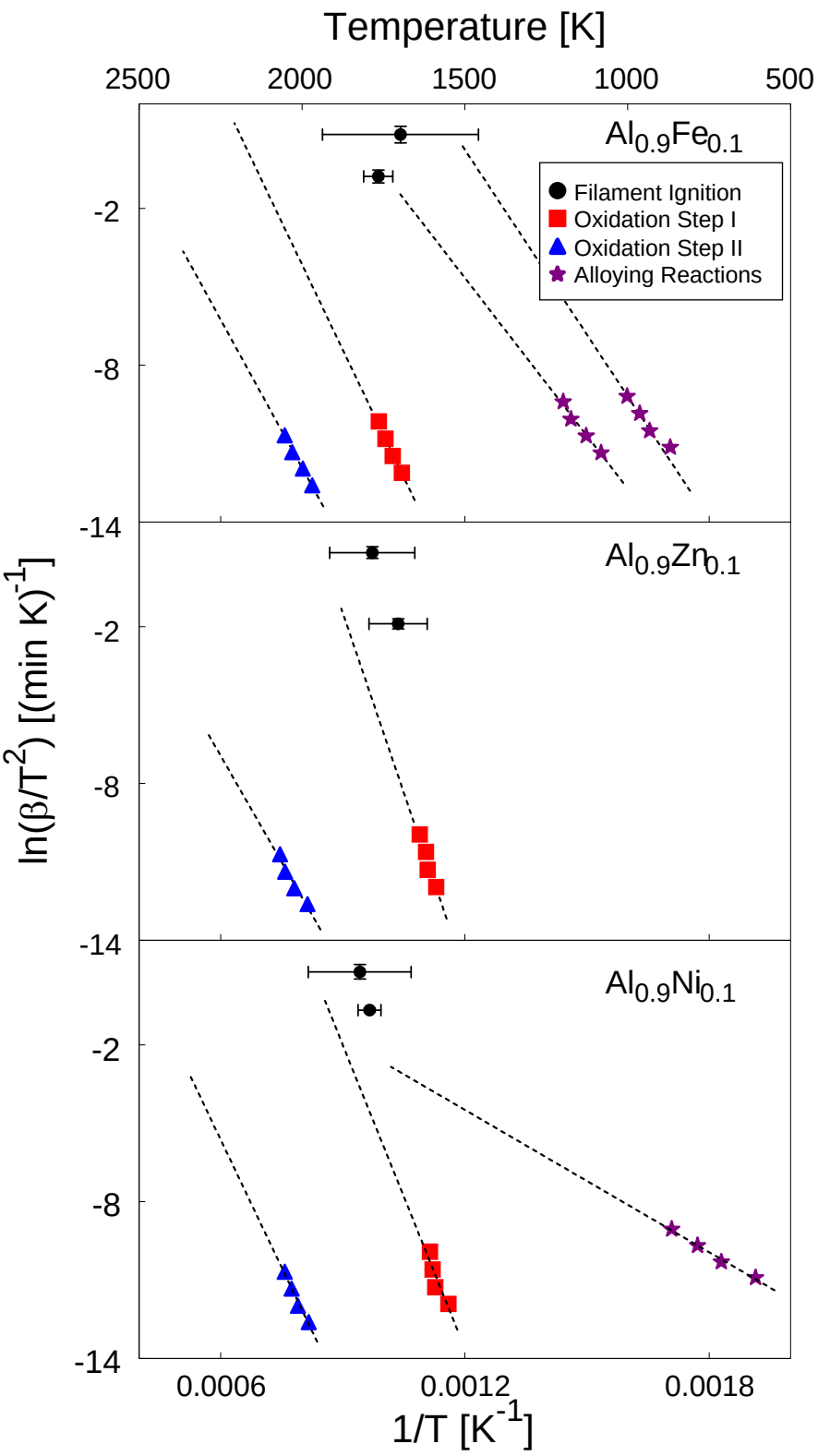

Figure 2.18 Kissinger plot comparing ignition and oxidation data for $Al_{0.9}Fe_{0.1}$, $Al_{0.9}Zn_{0.1}$, and $Al_{0.9}Ni_{0.1}$ composites.

2.6 Conclusions

Aluminum-based composites with Fe, Ni, and Zn additives were prepared by mechanical milling. For Ni and Zn, preparation of composites, while restricting formation of intermetallic phases, is only possible with very short milling times. Consequently, many Ni and Zn inclusions remain relatively coarse and particles are shaped as platelets (or coarse flakes) for both Al-Zn and Al-Ni composites prepared by ball milling. For Al-Fe, preparation of equiaxial particles is possible with fine Fe inclusions uniformly distributed in Al matrix.

The presence of Fe, Ni, or Zn inclusions in the ball-milled powders substantially changes ignition and low-temperature oxidation of the composite powders as compared to unmilled aluminum. For composite powders prepared at short milling times, ignition occurs at lower temperatures and low temperature oxidation is accelerated. For powders with identical compositions, but milled longer, containing intermetallic phases and a more homogenized Al matrix, the low temperature oxidation is impeded. Comparison of the prepared Al-metal composites with $Al{\cdot}Al_2O_3$ reference composites prepared with similar milling conditions suggests that the altered Al morphology, such as developed grain boundary network produced in the milled powders, is primarily responsible for their accelerated low-temperature oxidation. It is further observed that simply an increase in the low-temperature oxidation rate detected in DSC/TGA experiments is insufficient to achieve ignition of the material under rapid heating conditions. Thus, it is concluded that the improved ignition dynamics for the prepared Al-metal composites is due to a combination of the accelerated low-temperature oxidation with reaction mechanisms altered by the presence of metal inclusions.

For 20-min milled Al-Ni and Al-Zn composites, the oxidation begins with selective oxidation of Ni and Zn, respectively, and is followed by an Al oxidation step increased substantially compared to that observed for the pure Al at the same temperatures. For Al-Fe samples prepared with longer milling times, the first oxidation step is delayed and occurs after Al melting. The activation energies for the first oxidation step for all composite powders are different from that identified for the unmilled Al, indicating a difference in the reaction mechanisms. The subsequent oxidation steps are similar for the prepared composite and unmilled Al powders.

It is observed that the ignition is likely correlated with intermetallic reactions in Al-Ni and, possibly, Al-Fe composites. For all materials, a correlation between the first, low temperature Al oxidation step and ignition is also indicated. Unlike for the unmilled Al, for which oxidation at low temperatures results in growth and evolution of the protective surface oxide film, for the prepared Al-Zn and Al-Ni composites, the low temperature oxidation results in an effectively volumetric increase in the oxygen concentration in the Al matrix, but not in the inclusions of Zn and Ni, respectively.

CHAPTER 3

IGNITION AND COMBUSTION OF MECHANICALLY ALLOYED $Al_{0.47}Mg_{0.53}$ POWDERS WITH CUSTOMIZED PARTICLE SIZES

3.1 Abstract

Adding aluminum to propellants, pyrotechnics, and explosives is common to boost their energy density. A number of approaches have been investigated that could shorten aluminum ignition delay, increase combustion rate, and decrease the tendency of aluminum droplets to agglomerate. Previous work showed that particles of mechanically alloyed Al·Mg powders burn faster than similarly sized particles of pure aluminum. However, preparation of mechanically alloyed powders with particle sizes matching those of fine aluminum used in energetic formulations was not achieved. This work is focused on preparation of mechanically alloyed, composite Al·Mg powders in which both internal structures and particle size distributions are adjusted. Milling protocol is optimized to prepare equiaxial, micron-scale particles suitable for laboratory evaluations of their oxidation, ignition, and combustion characteristics. Oxidation of the prepared powders is studied using thermo-analytical measurements. Ignition is characterized experimentally using an electrically heated filament setup. Combustion is studied using a constant volume explosion setup for the powder cloud combustion, and a laser ignition setup for characterization of combustion rates and temperatures for individual particles. For the prepared materials, ignition and combustion characteristics are compared to those of pure Al. It is observed that the mechanically alloyed powders ignite at much lower temperatures than Al. Once ignited, the particles burn nearly as fast as Al, resulting in an overall improvement of the combustion performance.

3.2 Introduction

Metal-based, binary, mechanically alloyed and nanocomposite materials offer advantageous performance as fuel additives in energetic formulations for propellants, explosives, and pyrotechnics [9-11, 50, 51]. Recent research is focused on aluminum-based materials with reactivity enhanced compared to pure Al powders. These materials have high combustion enthalpies (typical of Al), with tailored density, high energy density, and reduced ignition delays (i.e., alloys or composites of Al·Mg, Al·Ti, etc.) [15, 16, 28-31]. In addition, research was active to produce nano-sized powders of reactive metals [52-54], which achieve high burn rates due to highly developed reactive surface [55]. New materials prepared by arrested reactive milling [56] combine advantages of conventional, micron-sized composite or alloyed powders with reactivity of energetic nanomaterials [3, 16, 38, 57-59]. In order for these materials to be practically useful, their particle size distribution should be adjusted to make them compatible with the existing protocols for preparation of energetic formulations. However, cold welding that often occurs due to the ductile nature of Al prevents synthesis of mechanically alloyed powders with useful size distributions. Process control agents (PCAs) have been used previously to avoid or minimize cold welding; similarly, smaller particle sizes can, in principle, be obtained by using smaller milling balls [32]. Still, Al-based mechanically alloyed powders with attractive compositions prepared to date [30, 33] were too coarse for practical applications. Long milling durations and increased PCA amounts can be used to further reduce particle size, but milling tools and PCAs contaminate the desired formulations [32].

This chapter discusses the preparation and characterization of mechanically alloyed Al·Mg powders with customized particle size distributions. Al·Mg alloys have been explored for applications in energetic materials for a long time. Some of the first applications were in pyrotechnic formulations [60-62] while more recently, such alloys were successfully added to propellants [63]. It has been reported that Al·Mg alloys ignite at much lower temperatures than pure Al [64, 65]. Combustion of alloys was also studied, with most detailed experimental observations on coarse particles with dimensions exceeding 100 μm [34, 66, 67]. It was reported that depending on composition, either Al or Mg determine the alloy combustion dynamics [68]; alternatively, a staged combustion behavior was described, in which Mg combustion preceded that of Al [69]. Despite significant attention to combustion characteristics of Al·Mg alloys [34-36], combustion of fine particles of such alloys has not been studied in detail, most likely because such fine particles are not readily available. Thus, enabling preparation of fine Al·Mg alloy powders by mechanical alloying, a very versatile materials manufacturing method, is of substantial interest. The issue is challenging primarily due to high ductility of Al, which tends to result in cold welding and coarse product particles. In previous research, elemental iodine was milled with aluminum resulting in particle size reduction [37]. In this work, iodine is used as an additional PCA enabling a better control over the particle shapes and sizes for an Al·Mg alloy. A 2-step ball milling technique is implemented with the first milling step used to achieve the desired structural and compositional refinement. Iodine is added and smaller milling balls are used for the second milling step aimed to reduce particle sizes. Combustion and

ignition of the prepared materials is investigated and correlations between different oxidation, ignition, and combustion characteristics are studied.

3.3 Experimental

3.3.1 Material Synthesis

Starting materials included elemental powders of Al (Atlantic Equipment Engineers, 99.8% pure, -325 mesh) and Mg (Alfa-Aesar, 99.8% pure, -325 mesh). Powders were blended and mechanically milled using a Retsch PM-400 MA planetary mill. Nominal powder composition was $Al_{0.47}Mg_{0.53}$, or 1:1 for Al:Mg by weight. The rotational speed was set to 350 rpm. The direction of rotation was set to reverse every 15 min.

The powders were milled in two steps. The first step was aimed to achieve compositional homogeneity between components as in conventional mechanical alloying. The second step was added to tailor the particle size distributions of the produced powders using additional PCA and altered milling conditions. The powder prepared in the two-step (2-step) milling was compared to a reference mechanically alloyed sample prepared in one step (1-step) with a duration equal to the total milling time of the 2-step procedure. Additional comparisons were made with the powder prepared using only the first step (1^{st} step) of the 2-step procedure.

For the 1^{st} step milling, elemental powders of Al and Mg were loaded in 0.5-l steel milling vials with 9.5-mm diameter hardened steel milling balls. Vials were filled in argon with a 30-g powder load and 300 g of milling balls (charge ratio of 10). 50 ml of hexane (C_6H_{14}) was added to each milling vial as a PCA. The milling duration was 120 min. This completed the 1^{st} step milling. For further processing, vials were opened in

argon and iodine (I_2, chips, Sigma Aldrich, 99% pure) was added as 4 wt. % of the initial powder load to serve as a new PCA. After adding iodine, the vials were closed and milled for 5 min. to clean the 9.5-mm milling balls, which were then removed and replaced with the same mass of 3-mm diameter steel milling balls. The balls were replaced inside an Ar-filled glovebox. The second, softer milling step was then performed to produce mechanically alloyed powder with the desired finer particle sizes. The duration of the second milling step was 60 min. The total milling time was, therefore, 185 min. This milling time was also used to prepare reference samples milled in a 1-step process. Other milling conditions corresponded to those used in the first step of the 2-step milling, while iodine (4 wt. %) was included with the starting blend of Al and Mg powders.

The prepared powders were removed from the milling vials in the Ar-filled glovebox. The powder was left in the glovebox overnight, where it was exposed to an environment with low oxygen concentration (~2%). This exposure passivated the powder surface so that the powder could then be recovered and handled in open air.

3.3.2 Material Characterization

Scanning electron microscopy (SEM) was used to study powder morphology using a Phenom Tabletop Microscope by FEI Technologies Inc. Backscattered electron images were taken to inspect particle shapes and sizes. Particle size distributions of the prepared composites were measured with low-angle laser light scattering using a Beckman-Coulter LS230 Enhanced Particle Analyzer. Powder suspensions for analysis were prepared in ethylene glycol ($C_2H_6O_2$) and sonicated to minimize particle agglomeration. Phase compositions of the samples were analyzed using X-ray Diffraction (XRD) on a Phillips

X'pert MRD powder diffractometer operated at 45 kV and 40 mA, using Cu K_α radiation (λ = 1.5438 Å). The patterns were collected between 10 and 85° at a rate of 0.625°/min.

Thermal stability and temperature-dependent phase transformations were studied using differential scanning calorimetry (DSC) and thermogravimetric analysis (TGA) using a Netzsch Simultaneous Thermal Analyzer STA409 PG with a DSC sample carrier and corundum sample crucibles. Oxidation experiments were performed in a mixed 1:1 ratio of oxygen (50 ml/min, Matheson, 99.98% purity) and ultra-high purity argon (50 ml/min, Matheson, 99.99%) at various heating rates between 5 and 40 K/min. Decomposition experiments were performed in argon only and at a heating rate of 5 K/min. Ignition of the prepared materials was analyzed using a heated filament ignition apparatus described in detail elsewhere [42, 43]. A thin layer of powder was coated onto a nickel-chromium alloy wire (manufacturer-specified working temperature range up to 1953 K). The wire was heated by a DC current and its temperature was monitored optically using an infrared pyrometer focused on its uncoated surface adjacent to the powder coating. Concurrently, light emission from the powder coating was measured using a photodiode sensor, in which a sharp onset of light emission was identified as the ignition instant. The temperature measured by the pyrometer at that instant was assumed to be the ignition temperature. Such experiments were conducted in air for a range of heating rates between 10^3 and 10^5 K/s. Ignition instant was also identified from videos recorded using a high-speed camera (MotionPro500 by Redlake) at 500 fps.

Combustion was studied using a constant volume explosion (CVE) setup for powder aerosol combustion, and a laser ignition setup for characterization of combustion rates and temperatures for individual particles. The details of the CVE experiments were

described elsewhere [70-72]. The aerosolized powders were ignited from the center of a nearly spherical 9.2-L vessel. The vessel was initially evacuated, after which the powder was introduced with an air blast by opening a solenoid valve connecting the vessel with a chamber filled with compressed air. After the air blast, ignition was triggered following a delay of 300 ms, provided to reduce turbulence. The targeted initial pressure in the explosion vessel prior to ignition was 1 atm. Combustion pressure traces were recorded using both static and dynamic transducers. The measured pressures traces are normalized by the initial pressure in the vessel (P/P_0). The rates of pressure rise, $d(P/P_0)/dt$, are also reported for the prepared composite and reference pure Al powder. (P/P_0) and $d(P/P_0)/dt$ are proportional to the flame temperature and combustion reaction rate, respectively [73].

For laser-ignited single particle combustion, the experimental technique is described in Refs. [74-76]. A vertically rising particle jet with low number density was generated using a vibratory powder feeder [77]. Particles ignited when crossing a CO_2 laser beam. Luminous streaks produced by the ignited particles were photographed. Four photomultiplier tubes (PMT, Hamamatsu H3164-10) were used to record the light emission from burning particles. The PMTs were equipped with interference filters (486, 532, 568, and 589 nm). Emission signals filtered at 532 and 589 nm were used for optical pyrometry. The 486 nm filter was selected to track one of the strongest AlO emission bands as an indicator of the intensity of the vapor-phase reactions. Because no substantial AlO emission occurs at 568 nm, the strength of the observed AlO emission was evaluated using the ratio of the signal intensities measured at 486 and 568 nm: $R_{AlO}=I_{486}/I_{568}$. Following Ref. [78], the measured ratio was normalized by its theoretical

value calculated for respective intensities of a black-body emitter at the same temperature as the measured particle temperature.

3.4 Results

3.4.1 Particle Sizes, Morphology, and Phase Composition

Figure 3.1 shows SEM images of the prepared powders. The image on the left shows the coarse powder obtained after the first, 120-min milling step. This milling time was selected based on the SEM images of the product showing equiaxial particles rather than flakes, with no apparent compositional contrast between Al and Mg (clearly visible at shorter milling times), and with no apparent detached Al or Mg particles. The powder prepared during the 1st milling step has a mean volumetric size of ~23 μm, as seen in Figure 3.2. The product of the 2-step milling is shown in the center image of Figure 3.1. The powder includes fine, equiaxial particles with rounded shapes and a narrow size distribution (Figure 3.2). The reduction in the mean volumetric particle size (from 23 to 12.5 μm, cf. Figure 3.2) caused by the second milling step is also apparent in Figure 3.1. To further validate the effectiveness of this modified, 2-step milling procedure, the powder was compared to a reference sample prepared in 1-step with the same milling time as the 2-step sequence, as shown in the right most image of Figure 3.1. The particles of the reference sample appear to have a broader size distribution compared to the powder prepared using the 2-step process. This is also apparent in the size distribution measurements in Figure 3.2. The 1-step powder is coarser and has a broader particle size distribution than the powder prepared by the 2-step milling, despite a similar volumetric mean.

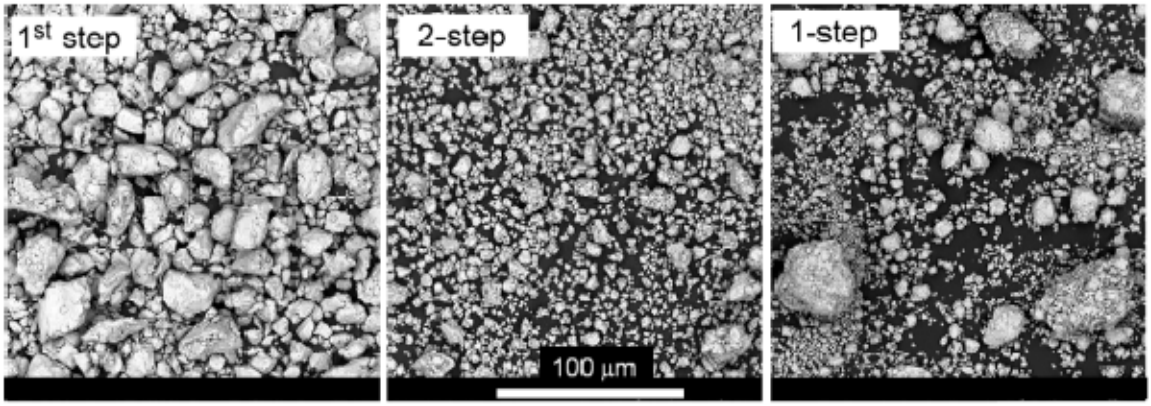

Figure 3.1 SEM images of Al·Mg powders: the product of the 1st, 120-min. milling step (left); the product of the 2-step milling, total time 185 min. (center), and product of the 1-step milling, total time 185 min. (right).

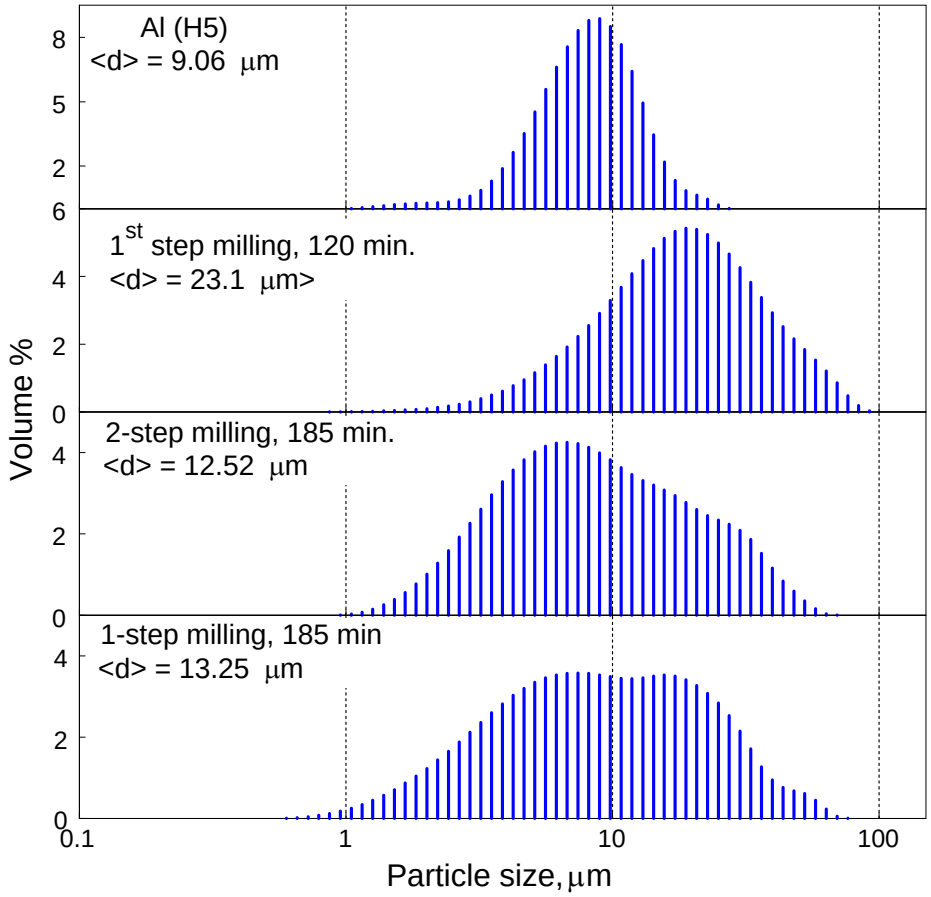

Figure 3.2 Particle size distributions of the products of the first milling step (120 min.), 2-step milling (185 min.), 1-step milling (185 min.), and pure Al powder (top) used as a reference in aerosol combustion experiments. Volume mean particle sizes are shown for each powder.

Figure 3.3 shows XRD patterns for the 1st step (120 min.) and 2-step (185 min.) milled powders as well as for a blended Al·Mg sample used as a reference. Peaks corresponding to pure Al and Mg are indicated in the plot. Remaining peaks have been identified as the γ - $Al_{12}Mg_{17}$ intermetallic. For the 1st step powder, the pattern shows that peaks of Al and Mg are present along with peaks corresponding to γ - $Al_{12}Mg_{17}$. For the 2-step powder, the pattern shows that all Mg is incorporated into $Al_{12}Mg_{17}$ phase mixed with the little remaining pure Al. The XRD pattern of the 2-step milled powder matches well the patterns for mechanically-alloyed Al-Mg powders reported previously [33].

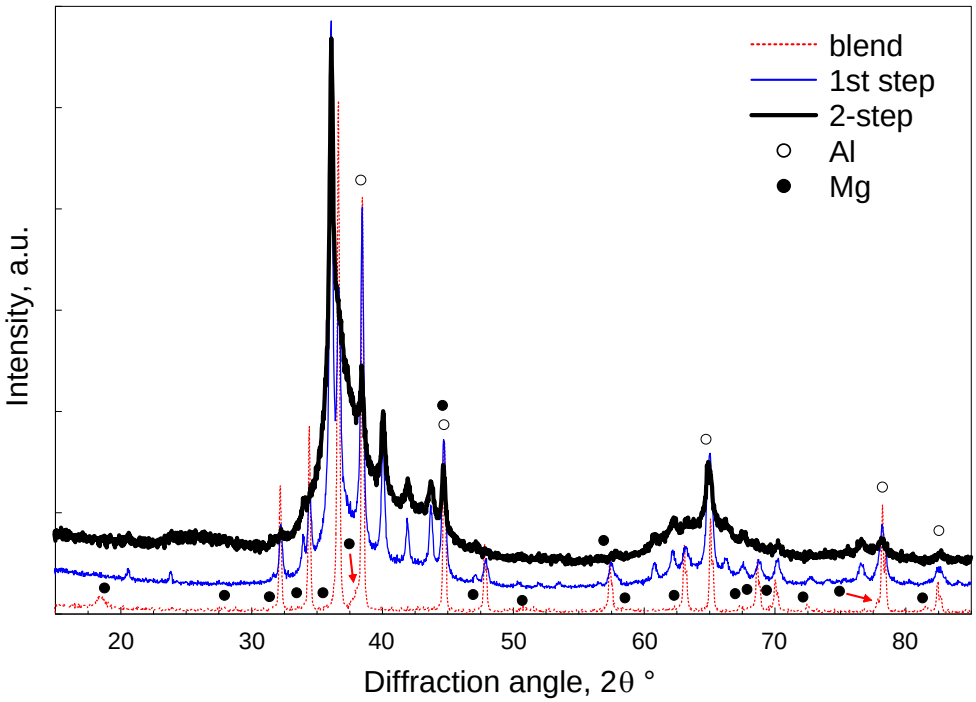

Figure 3.3 XRD patterns of an Al-Mg blend, 1st step (120 min.), and 2-step (185 min.) milled powders. Elemental Al and Mg phases are indicated in the plot. All other (unlabeled) peaks correspond to the γ - $Al_{12}Mg_{17}$ phase.

3.4.2 Ignition

Figure 3.4 shows the ignition temperatures of the prepared Al·Mg powders as a function of heating rate, with each point representing an individual ignition experiment. As expected for a thermally activated ignition mechanism, ignition temperatures increase slightly with increasing heating rates. Ignition temperatures are approximately 860 K at lower heating rates and 1060 K for higher heating rates. These temperatures are somewhat higher than 783 K reported for an Al-Mg alloy with similar composition but ignited by its slow heating [65]. For comparison, ignition temperatures for pure Al and Mg powders are also shown. Ignition temperatures of Al·Mg composites are much lower than ~1850 K reported for ignition of pure Al [48] at similar heating rates, and seem to be close to the ignition temperature of the pure Mg [43].

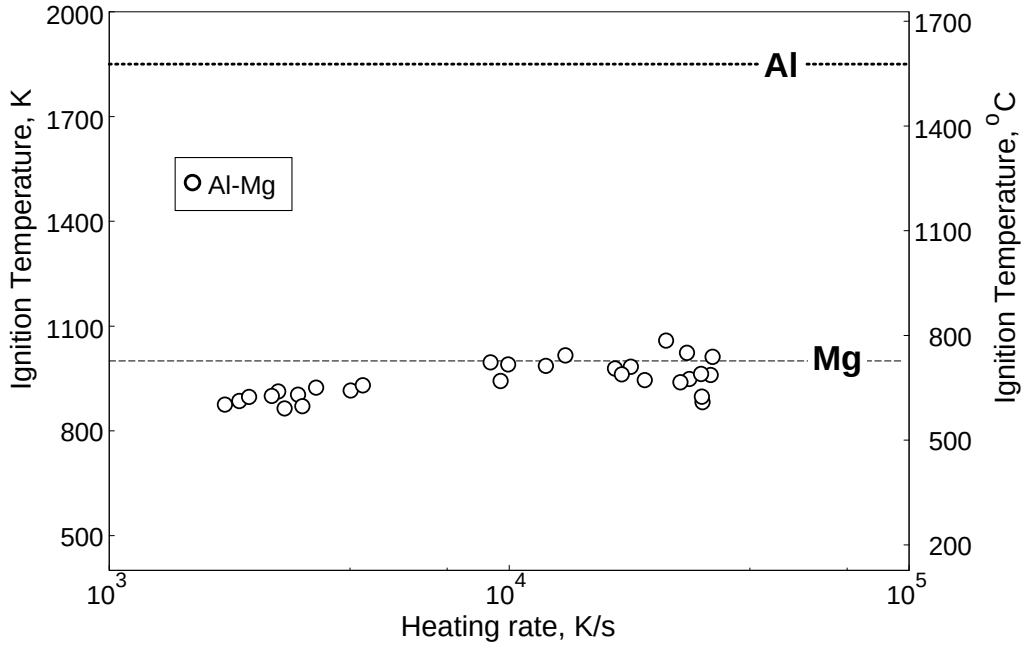

Figure 3.4 Ignition temperatures of Al·Mg powders prepared by the 2-step milling as a function of heating rate.

3.4.3 Thermal Analysis and Reaction Kinetics

DSC and TGA traces for the decomposition experiments performed in Ar at 5 K/min are shown in Figure 3.5. Poorly distinguished, intermetallic formation reactions can be observed at low temperatures in DSC. A weak exothermic feature is seen where sub-solidus reactions are expected compared to more detailed earlier measurements for the mechanically alloyed Al-Mg powders [33, 79]. An endothermic peak corresponding to the eutectic melting at ~450 °C (~723 K) is visible for both powders and occurs as expected from the binary Al-Mg phase diagram [79, 80]. At higher temperatures (after eutectic melting), poorly resolved exothermic features in DSC are observed and may be attributed to oxidation involving oxygen impurity in the flowing Ar gas environment. This oxidation results in a mass increase of about 2 % recorded by TGA for the 1st step milled powder. For the 2-step powder, the mass loss of ~2% occurring after eutectic melting is attributed to the release of I_2, similar to the I_2 release observed in mechanically milled Al·I_2 powders [78]. Assuming that the 2-step powder oxidizes similarly to the 1st step powder, it is reasonable to conclude that the entire iodine introduced during milling, i.e., 4 wt. % of the powder mass, is retained in the 2-step powder as prepared.

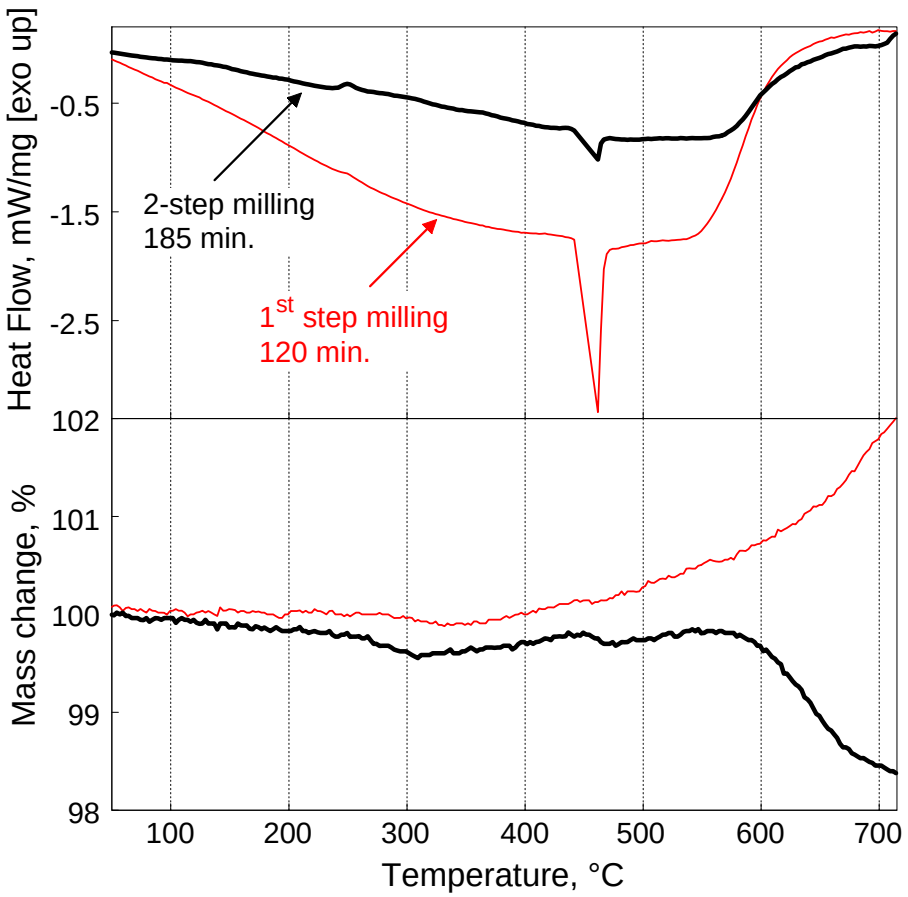

Figure 3.5 DSC and TGA traces for the decomposition experiments performed in Ar at 5 K/min for 1st and 2-step milled Al-Mg powders.

Figure 3.6 shows DSC and TGA traces for the Al·Mg powders prepared by 1- and 2-step milling, as well as powder prepared by the 1st step milling heated in the mixed O_2/Ar environment. For all traces, an endotherm corresponding to that of the eutectic melting at ~450 °C is observed [30, 33, 79-81]. An exotherm corresponding to the strong oxidation step in TGA is also observed consistently for all materials. For the composite prepared using the 2-step milling, the oxidation has an earlier onset than for the other samples. Both samples milled for 185 min (using both 1- and 2-step milling protocols) show exothermic peaks immediately after the eutectic melting. This post-eutectic melting exotherm is not present in the 1st step milled sample. The oxidation behavior

described in Ref. [81] for Al·Mg composites with a comparable composition is qualitatively similar to that observed for the latter (1st step) sample prepared in this project.

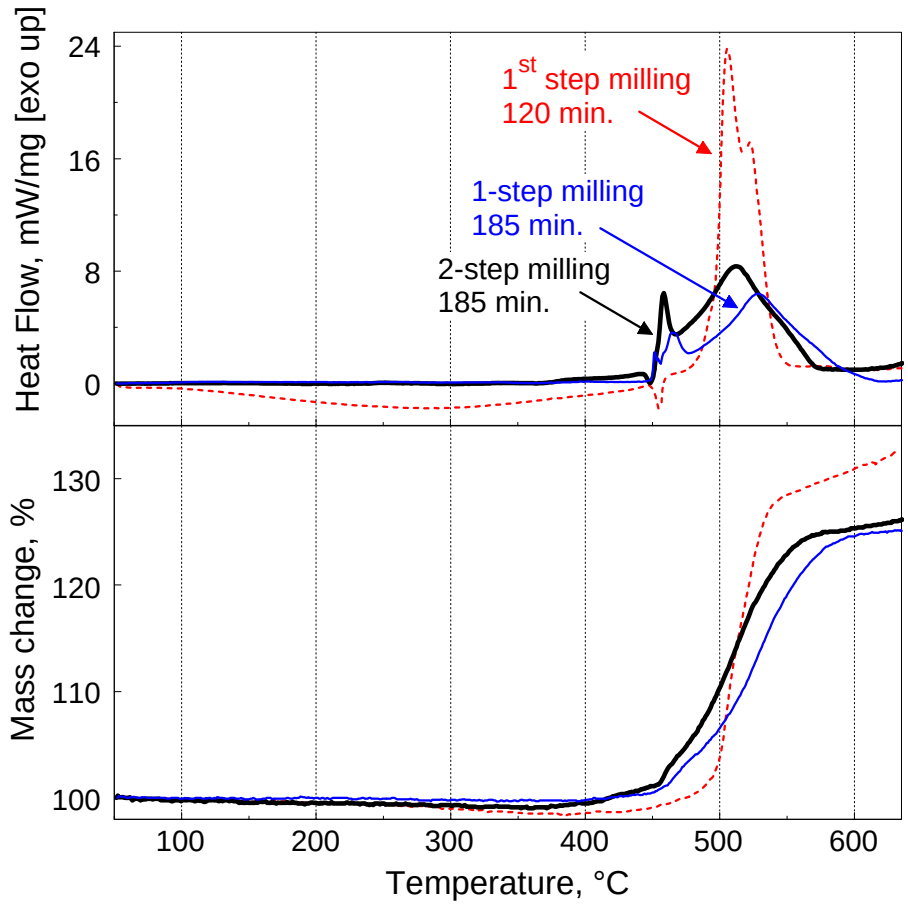

Figure 3.6 DSC traces for Al·Mg powders heated in oxygen at 5 K/min prepared using different milling procedures, including 1st step, 2-step, and 1-step milling.

The powder prepared using the 2-step procedure was heated in TGA in the same oxidative environment at different heating rates in the range of 5 – 40 K/min. Derivatives of TGA traces (DTG) at varying heating rates were used to construct Kissinger plots [49] using the DTG peak maxima. The resulting Kissinger plot (logarithm of heating rate, β, divided by temperature square vs. inverse temperature) is shown in Figure 3.7; it also

shows the results of the filament ignition experiments presented in Figure 3.4. From Figure 3.7, it is apparent that the points corresponding to the strong oxidation step do not line up with those of the filament ignition. This indicates that relatively strong exothermic processes detected in thermo-analytical measurements do not directly cause ignition of these powders. Further, one must consider that the measured filament ignition temperatures recorded are those of the filament and not of the powder coating, suggesting that the points seen in Figure 3.7 could shift more to the right side of the plot, if corrected to represent the actual powder temperature. Considering such a correction, it would appear that an event occurring at a lower-temperature (perhaps eutectic melting or formation of an intermetallic phase) may lead to ignition, e.g., by generating additional fresh surface in the sample.

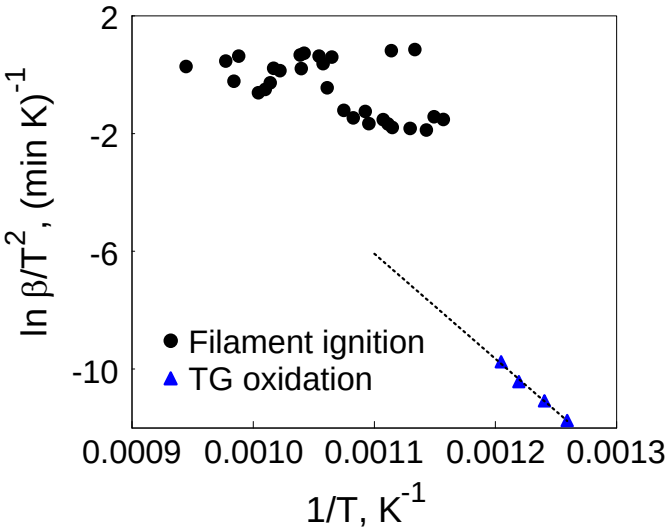

Figure 3.7 Kissinger plot comparing ignition and oxidation data for Al·Mg composites as a function of heating rate.

3.4.4 Powder Cloud Combustion

Both 1- and 2-step milled Al·Mg powders and reference Al (H5 powder by Valimet) powder were tested in the CVE experiment using the same initial powder mass loadings

of 4.65 g (corresponding to a fuel-rich mixture in the vessel). Results of these experiments are shown in Figure 3.8. The Al·Mg powder prepared using the 2-step milling technique has the highest pressure output and shortest ignition delay as compared to both the reference H5 Al and Al·Mg powder prepared by 1-step milling. A better performance of the 2-step milled powder as compared to the 1-step milled powder may be due to a narrower particle size distribution (cf. Figure 3.2), with fewer coarse particles hindering the reaction.

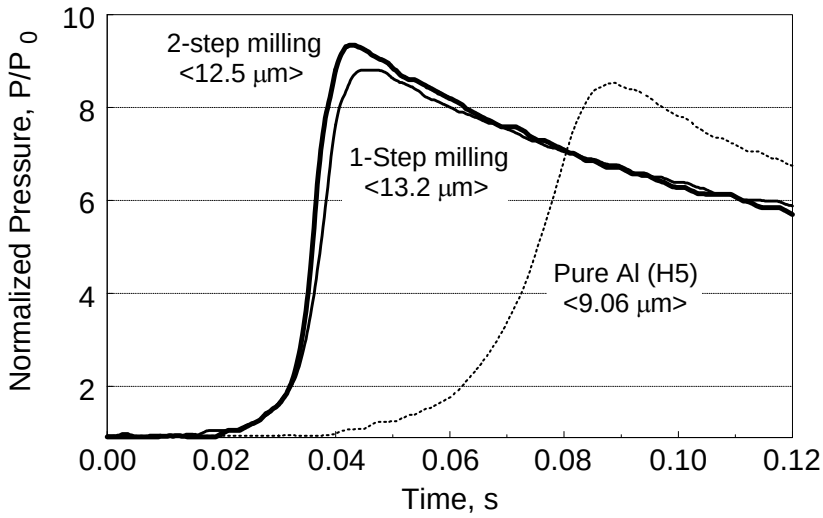

Figure 3.8 Normalized pressure as a function of time for 2-step (185 min.), single-step, and reference Al samples.

Table 3.1 summarizes the mean pressure and rate of maximum pressure rise ratio values for the prepared Al·Mg and reference H5 Al powder. Standard deviation values were calculated from repeated experiments. Al·Mg powders show higher $(P/P_0)_{max}$ and $[d(P/P_0)/dt]_{max}$ values than pure Al powder, indicating a higher flame temperature and combustion rate. For reference, explosion pressures calculated for the constant volume combustion using experimental powder loads in air are also shown in Table 3.1. The calculations used NASA CEA code [82] and Al-Mg alloys were treated as blended Al

and Mg powders. Initial pressure was assumed to be 1 atm and the reactants were taken at room temperature. The comparison of calculated and experimental pressures shows that the experimental pressures are systematically lower than the pressures predicted by the thermodynamic equilibrium for all materials, as expected because of incomplete combustion and heat losses.

Table 3.1 Summary of CVE Experiment Results (Data Represent Average Values ± Standard Deviations)

Sample	$(P/P_0)_{max}$	$[d(P/P_0)/dt]_{max}$; s^{-1}	(P/P_0)max calculated
Al·Mg (2-step)	9.02 ± 0.28	1135 ± 207	13.3
Al·Mg (1-step)	8.89 ± 0.49	1061 ± 166	13.3
pure Al (H5)	8.54 ± 0.33	439 ± 105	12.4

3.4.5 Single Particle Combustion

A photograph of burning particle streaks is shown in Figure 3.9 for the Al·Mg powder prepared by the 2-step milling. Several particle streaks observed in Figure 3.9 were produced by different particles fed successively through the laser beam during the time of exposure. Each well discerned streak represents a particle passing through the CO_2 laser beam. Most streaks include two separate bright portions and end with characteristic spearpoints.

A typical emission trace, a temperature trace obtained by 2-color pyrometry, and a ratio R_{AlO} for a burning Al·Mg particle are shown in Figure 3.10. Consistently with the visible streaks in Figure 3.9, emission traces in Figure 3.10 also show distinct peaks. The first peak corresponds to a higher temperature and lower level of AlO emission. The initial temperature increase is consistent with the emission intensity ramp. The first peak

is then followed by a second peak accompanied with a characteristic oscillatory emission pattern. This second peak is typically longer than the first one. The measured temperature and R_{AlO} are observed to slowly decrease until the final small peak (corresponding to a "spearpoint" in the photograph) is observed. The overall emission intensity level at which the spearpoints occur is substantially reduced compared to its peak value, so that both temperature and R_{AlO} measurements are no longer meaningful.

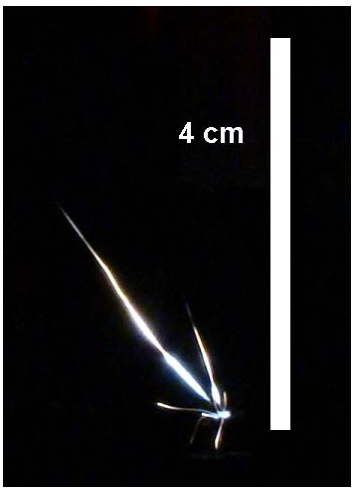

Figure 3.9 Burning particle streaks of Al·Mg powder prepared following the 2-step milling process and ignited in the CO_2 laser beam.

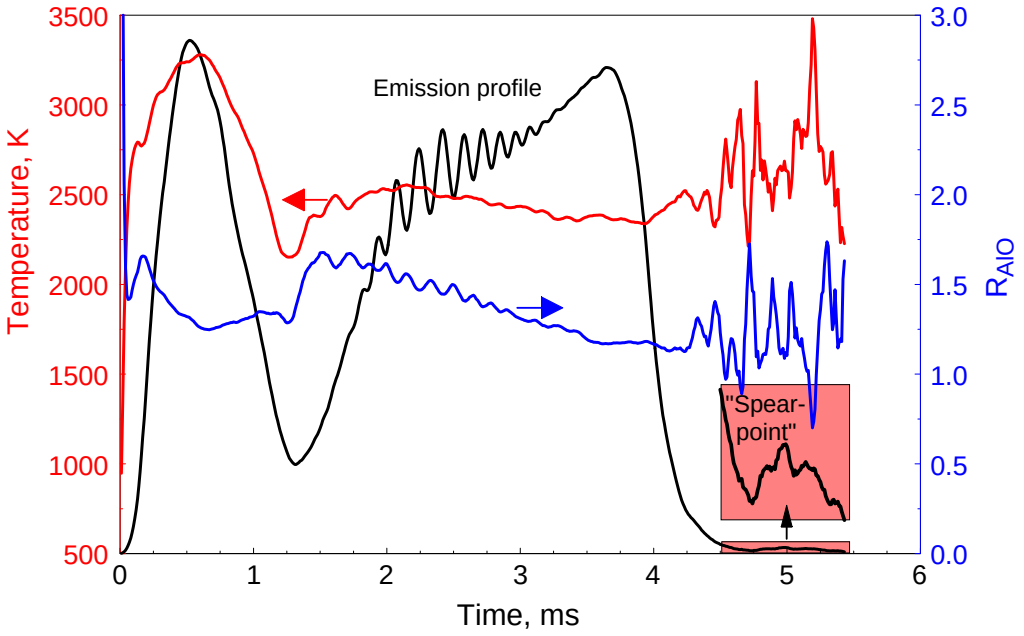

Figure 3.10 Emission signal (vertical scale is in arbitrary units, the axis is not shown), temperature, and an intensity ratio characterizing significance of the molecular AlO emission for a single laser-ignited particle of mechanically alloyed Al·Mg powder prepared following the 2-step procedure (185 min. milling time).

Slight delays in the ignition of Al·Mg particles can be observed in the photograph in Figure 3.9, i.e., luminous streaks do not always originate from the same area where the CO_2 beam was focused. These delays made it impossible to process the experimental data following the procedure outlined and used in Refs. [74-77], where the size of each particle was evaluated based on the amplitude of a light-scattering pulse, generated when particles crossed a low-power auxiliary laser beam placed just under the CO_2 laser beam. The poorly reproducible ignition timing made it impossible to correlate the light scattering and emission pulses and to quantify the size of each ignited particle. Instead, a methodology described in Ref. [83] was used to obtain a correlation between burn times and particle sizes. The main assumption in this data processing is that the larger size particles burn longer. First, recorded emission pulses were preliminarily inspected to

remove overlapping or closely spaced signals, which may not represent individual particle combustion events. Durations of the downselected pulses were then measured. The data on pulse durations representing burn times were logarithmically binned and correlated with the particle size distributions for the respective powders measured by Beckman-Coulter LS230 Enhanced Particle Analyzer. The volume-based particle size distributions shown in Figure 3.2 were transformed into number-based, cumulative distributions, to be directly compared to the burn time data shown in Figure 3.11. For reference, Figure 3.11 also shows the burn times measured elsewhere for the reference Al 10-14 μm powder [74-77], binned the same way as the results of the present measurements for Al·Mg powders. Once the size distributions are obtained in terms of particle number densities in respective size bins, the data shown in Figure 3.11 are recast in terms of particle burn times as a function of their size.

The particle size distributions are shown in Figure 3.12 in terms of cumulative number density as a function of particle size. These cumulative number density curves (Figure 3.12) were fitted using a log normal distribution function and correlated to the burn time. The final burn times as a function of particle sizes are shown in Figure 3.13. For both powders, the result is well represented by $t \sim d^n$ trends (shown as dashed lines). Burn times for Al·Mg particles greater than 2 μm are are slightly longer than those of the same size pure Al particles; however, the difference is rather small.

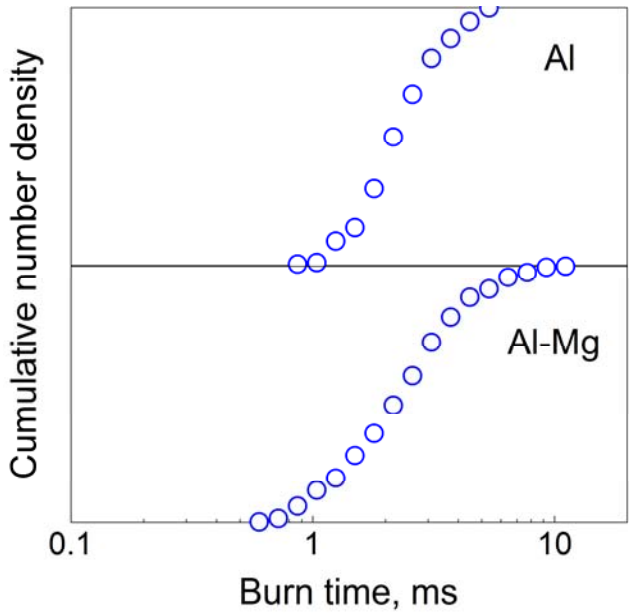

Figure 3.11 Cumulative number density vs. burn time for Al·Mg powder particles prepared following the 2-step milling procedure and for pure Al powder (10-14 μm nominal particle size).

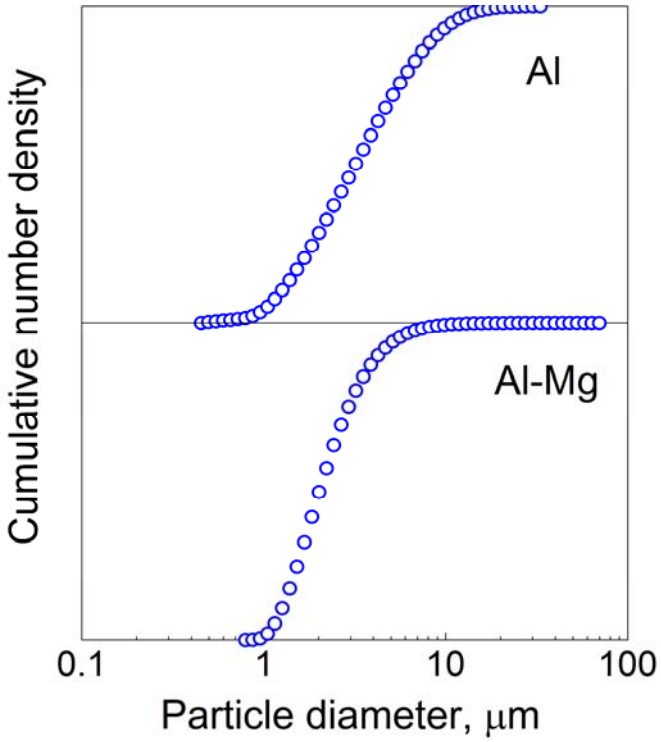

Figure 3.12 Cumulative number density vs. particle size for Al·Mg powder particles prepared following the 2-step milling procedure and for pure Al powder.

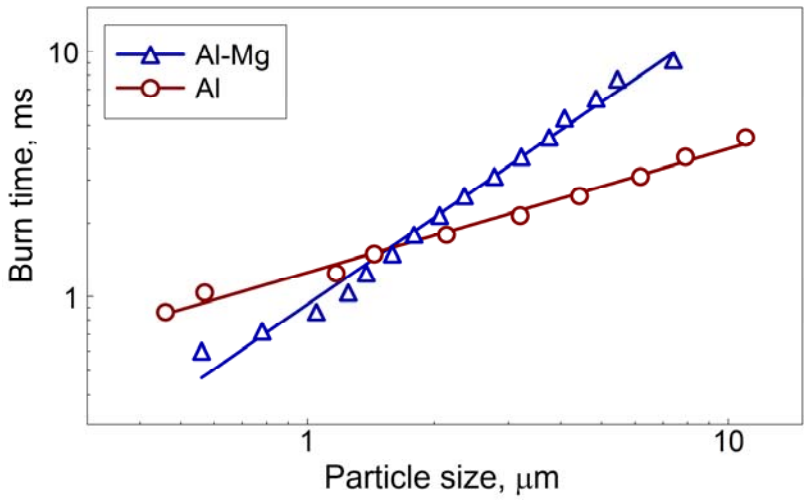

Figure 3.13 Particle burn time as a function of size for the Al·Mg powder prepared using the 2-step milling and for pure Al powder. Lines show respective d^n fits (n=0.5 for Al and n=1 for the Al·Mg alloy).

The temperature and AlO emission signals, such as shown in Figure 3.10, were averaged for each particle so that characteristic values could be assigned to the entire powder samples rather than individual particles. Average temperature values were calculated for each burn trace for the period of time when the emission signal varied within 50% and 100% of its peak value following the data processing described in [74-77]. The same procedure was used to calculate the average value of the normalized R_{AlO}. Resulting average values of R_{AlO} and temperature are shown in Figures 3.14 and 3.15, respectively. The data are shown for both the 2-step milled Al·Mg and pure Al powders. For Al combustion in air, R_{AlO} values greater than 1 indicate AlO vapor phase reactions. Values of R_{AlO} for Al·Mg powder are lower than those for pure Al, indicating substantial reduction in the importance of these vapor-phase reactions. Temperatures obtained for the Al·Mg powder are similar to those of pure Al. For both powders, despite substantial data scatter a slight increase in temperature is observed for particles with longer burn times. The increase in scatter in the calculated average temperatures for Al·Mg powder

could be attributed to the morphology of the as-milled powders as well as the ignition delay observed in Figure 3.9. Note that the emission signal changes noticeably during each particle combustion event, so that the average temperatures and R_{AlO} values provide only very approximate information on the related reaction mechanisms. A more detailed analysis of the burning particle temperature histories is of interest for future work.

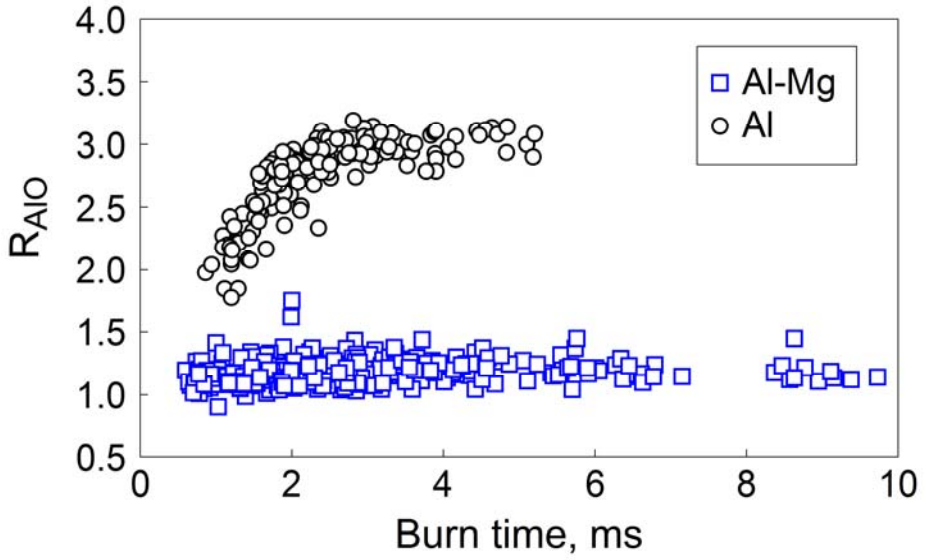

Figure 3.14 Normalized AlO ratio, R_{AlO}, values as a function of burn time for Al·Mg powder prepared using the 2-step milling and for pure Al powder.

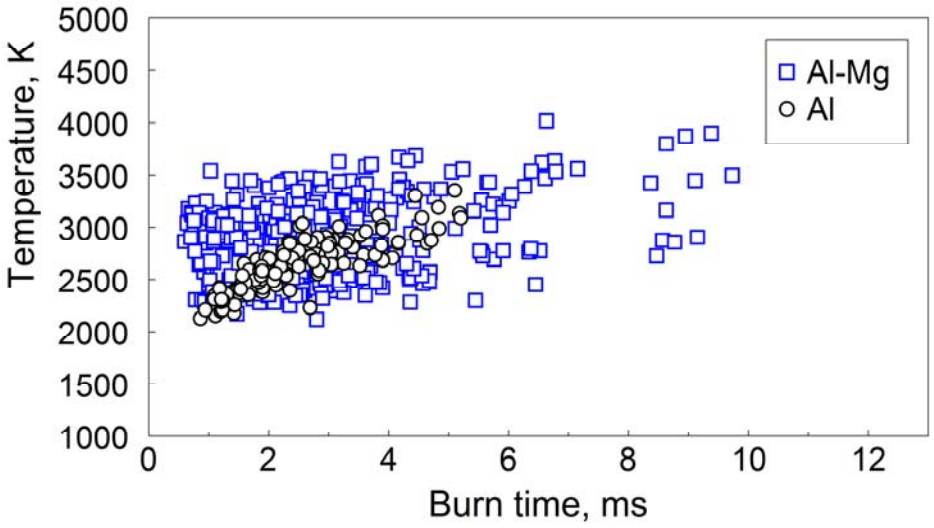

Figure 3.15 Combustion temperature as a function of burn time for Al·Mg powder prepared using the 2-step milling and for pure Al powder.

3.5 Discussion

Present experiments showed that iodine is a very effective PCA for mechanical alloying of Al·Mg powders. The powder particle sizes are reduced effectively (cf. Figures 3.1, 3.2) and with relatively short milling times. It is also shown that the 2-step milling offers a useful approach of tailoring particle sizes of mechanically alloyed powders without inducing substantial changes in their structure and causing their contamination by milling tools.

It was found that the initial nominal amount of I_2 added to the powder is retained in the prepared materials (as detected by TGA, cf. Figure 3.5). The effect of iodine on oxidation is not insignificant: the eutectic melting of Al-Mg alloys is immediately followed by substantial weight gain and energy release (Figure 3.5) only for the materials prepared with added iodine. It is likely that iodine-coated (or iodide containing) layers separate nano-scale grains or are embedded between consolidated metal flakes. Iodine from these layers is likely released causing formation of fresh surface; such fresh surfaces oxidize readily causing the exotherm observed for these materials to follow the eutectic melting. It is likely that this phenomenon is also important for ignition of the prepared Al·Mg alloys.

Added iodine may have another side benefit for the reactive materials, resulting in formation of halogenated combustion products with biocidal properties. Such products are desired for applications aimed to improve inactivation of aerosolized spores and bacteria in a blast [84-87].

Ignition temperatures for the prepared 2-step powders vary from approximately 860 to 1060 K for the range of heating rates covered in the present ignition experiments.

These temperatures are lower than the ignition temperatures reported for pure Al and close to those of pure Mg powders. Similar filament ignition experiments for mechanically alloyed Al-Mg powders reported previously [30] showed ignition temperatures of ~1020 K which are only slightly higher than the ignition temperatures reported here. The slight decrease in temperatures could be due to the morphological and particle size differences in the powders. The powders prepared in this work are finer and have a smoother surface than those described previously [30].

CVE results are generally consistent with a previous report of faster burn of Al·Mg alloys [30]. An improvement in both maximum pressure and rate of pressure rise for the prepared alloys as compared to the reference pure Al powder is significant in terms of possible practical applications of the developed material. The present work also offers a more detailed characterization of particle combustion. Results of the laser ignition experiments show that once ignited, Al particles burn faster than similarly sized particles of Al·Mg alloys. This is in agreement with recent measurements comparing combustion rates of Al and other materials [77]. An improvement in the pressure traces measured in CVE, as well as accelerated burn reported earlier based on aerosol combustion experiments [30, 88] are likely caused by a combination of the lowered ignition temperature and nearly unchanged burn rate.

The combustion mechanism of the prepared Al·Mg powders is clarified from the streaks and traces shown in Figures 3.9 and 3.10, respectively. A two-peak structure of the emission pulse suggests a 2-staged burn. Consistently with the earlier observations and proposed reaction mechanisms [69], it is suggested that Mg selectively burns first (stage I) followed by combustion of Al (stage II). This suggestion is supported by a

lower level of AlO emission during the initial portion of the emission pulse, corresponding to stage I. It is further supported by a characteristic oscillatory pattern observed during the stage II and common for Al particle combustion. This selective combustion of Mg is likely due to a lower vapor pressure of Mg compared to Al, enabling Mg vapors to react with surrounding air and consume all available oxygen, effectively starving Al combustion until Mg is consumed.

It is also interesting to compare the trends observed for particle burn times as a function of their diameter obtained in this work with similar trends reported previously. The same data set used to generate the trend reported in Figure 3.13 for pure Al was processed previously to report a somewhat weaker effect of particle diameters on their burn times [74, 75, 89]. The discrepancy with the present interpretation shown in Figure 3.13 is clearly attributed to the method used to process experimental data. When particle sizes were measured independently of their burn times [74, 75, 89], the results implied that at least for some particles, smaller particles burn longer than larger ones. Such data points, likely indicative of errors associated either with particle size measurement or with matching emission and scatter pulses, were processed differently in the present experiments. While real-time particle size measurements were not used, the particle size distribution that was used to process the present data was obtained by a much more accurate measurement. The stronger effect of particle sizes on their burn times obtained here, i.e., $t \sim d^{0.5}$ for Al and $t \sim d^{1}$ for Al·Mg alloy (rather than $t \sim d^{0.3}$ reported previously for Al), appears to be more reasonable and amenable to a theoretical interpretation.

A slight increase in the average flame temperature with particle size for both Al·Mg and pure Al powders is likely associated with an increased importance of the

stand-off vapor phase flame for larger particles. As discussed previously [90], the flame approaches the particle surface as the particle size decreases, eventually ceasing to exist for very fine particles. This changes the combustion regime from vapor-phase to surface reaction and is accompanied by reduction in the respective combustion temperature.

3.6 Conclusions

Preparation of mechanically alloyed powders of Al·Mg with fine particle sizes is feasible using a modified, 2-step milling technique that allows for simultaneous adjustment in both internal structures and particle size distributions. Particles suitable for laboratory evaluations of their oxidation, ignition, and combustion characteristics were prepared and characterized. Electron microscopy, x-ray diffraction patterns, and particle size distribution measurements showed that fine, equiaxial particles of Al·Mg with a homogeneous composition and a mean size of approximately 12.5 μm were produced. Filament ignition experiments of these mechanically alloyed powders conducted in air showed ignition temperatures in the range of 860 – 1060 K, which is significantly lower than ignition temperatures reported for pure Al powders which ignite at around 1850 K. Premixed flames in air were produced in the powder cloud combustion experiments and showed that a higher pressure output and shorter ignition delay can be achieved as compared to pure Al powders. Single particle laser experiments showed that once ignited, Al·Mg particles burn nearly as fast as pure Al particles of the same dimensions. It is also observed that the Al·Mg particles burn in a two-stage process proposed to include selective combustion of Mg followed by combustion of Al. Despite the slightly longer burn times, the improved ignition of Al·Mg particles and their high combustion

temperatures make them a viable replacement for pure Al powders in different energetic formulations.

CHAPTER 4

REACTIVE, MECHANICALLY-ALLOYED AL·MG POWDERS WITH CUSTOMIZED PARTICLE SIZES AND COMPOSITIONS

4.1 Abstract

Previous work showed that particles of mechanically alloyed Al·Mg powders burn faster than aluminum. However, such powders were coarser than fine aluminum commonly used in energetic formulations. This work addresses preparation of mechanically alloyed Al·Mg powders in which both internal structures and particle size distributions are adjusted. Powders with 50-90 at. % Al were prepared and characterized. Milling protocol was optimized to prepare equiaxial, micron-scale particles. Ignition temperatures measured using an electrically heated filament were much lower than those of pure Al powders and are close to those of Mg. Powders were aerosolized and ignited in air; the maximum pressure was higher, rates of pressure rise were greater, and ignition delays were shorter for the mechanically alloyed powders than for pure Al with directly comparable particle size distributions. Individual particle combustion experiments used laser ignition and showed that the alloyed particles burn in two stages, while the first stage is gradually disappearing with an increased Al concentration. The effect of particle size, d, on its burn time, t, for the prepared alloys is relatively well described by a $t \sim d^n$ law, where n is varying in the range of 1.1-1.5 for different compositions.

4.2 Introduction

Powders of Al and Mg with the heats of combustion of 834.9 kJ/mol and 607.6 kJ/mol, respectively, have long been known as attractive fuels for energetic formulations. Metal-

based, mechanically alloyed and nanocomposite powders may offer advantageous and custom-tailored performance as fuel additives in energetic formulations for propellants, explosives, and pyrotechnics [9-11, 50, 51]. Al·Mg alloys with varying compositions are also of interest as materials having high yield strength and an evolved grain boundary network [91, 92]. In addition, Al·Mg alloys are used in marine applications [93] for their corrosion-resistant properties and are of interest as hydrogen storage materials [94]. Aluminum-based powders prepared by mechanical milling, including alloys or composites of Al·Mg, Al-Ti, etc., with combustion characteristics enhanced compared to pure Al powders, have also been explored previously [15, 16, 28-31]. These materials are desirable because of the high combustion enthalpies (close to that of Al), with tailored density, reduced ignition delays, and faster burning rates. In order for these materials to be practically useful as drop-in replacements of aluminum powders as fuel additives, their particle size distribution should be adjusted to make them compatible with the existing protocols used for preparation of energetic formulations. In many current formulations, aluminum particles with sizes in the range of 1-15 μm are used. However, particle agglomeration that occurs due to the ductile nature of Al makes it difficult to prepare mechanically alloyed powders with such useful size distributions.

Process control agents (PCAs) have been used previously to avoid or minimize cold welding and therefore agglomeration; similarly, smaller particle sizes can, in principle, be obtained by using smaller milling balls [32]. Still, Al-based mechanically alloyed powders with attractive compositions prepared to date [30, 33] were too coarse for practical applications. Long milling durations and increased PCA amounts can be

used to further reduce particle size, but such milling conditions result in a substantial contamination of the mechanically milled materials [32].

In our recent study [95], a reactive powder with a composition of $Al_{0.47}Mg_{0.53}$ was prepared and its particle size distribution was adjusted using two stages of ball milling and adding a small amount of iodine as PCA for the stage 2, when particle size distribution was being custom-tailored.

The staged milling approach is being further explored in the present paper, where the range of Al/Mg compositions for mechanically alloyed powders with customized particle size distributions is extended. In particular, powders with greater aluminum concentrations, and thus higher combustion enthalpies, are prepared while their particle sizes remain adjustable. These powders offer an attractive combination of particle sizes, reaction enthalpies, and reaction rates. A two-stage, high-energy ball milling technique is implemented. The first milling stage is used to achieve the desired structural and compositional refinement. The second stage serves to achieve the desired particle size distribution. Combustion and ignition of the prepared materials are characterized using different techniques.

4.3 Experiment

4.3.1 Material Synthesis

Starting materials used in the synthesis of the composites included elemental powders of Al (Atlantic Equipment Engineers, 99.8% pure, -325 mesh) and Mg (Alfa-Aesar, 99.8% pure, -325 mesh). The material compositions varied systematically with the Al concentration ranging from 47 to 90 at. %. Powders were mechanically milled using a Retsch PM-400 MA planetary mill equipped with an air conditioner, which cools the

milling compartment. As described previously [95], the first stage of milling involved the preparation of mechanically alloyed Al·Mg powder. Powders of Al and Mg were loaded in steel milling vials in argon. 9.5 mm-diameter hardened steel milling balls were used. The powder charge was 30 g per vial and the ball to powder mass ratio was 10. A rotational speed was set to 350 rpm for 120 min. The rotation direction was changed every 15 min. 50 ml of hexane (C_6H_{14}) was added to each milling vial as a PCA.

The second stage of milling involved the addition of iodine (I_2, chips, Sigma Aldrich, 99% pure), at 4 wt. % of the initial powder load. The 9.5-mm balls were removed and replaced with the same mass of 3-mm hardened steel balls, which allowed for a softer milling necessary for particle size reduction.

The evolution of particle shapes and sizes is illustrated in Figure 4.1. Consistent with earlier observations, after the first milling stage the particles have lost their original shape, and after the formation and subsequent disappearance of flakes, the now work-hardened particles assume their steady-state, roughly equiaxed shape [95, 96]. The addition of iodine has an immediate and unexpected effect: an apparent increase in ductility causes particles to partially become flaky again. Only after an extended milling during the second stage do these flakes again disappear, and the final, now smaller, steady state particle size is achieved.

The reemergence of flakes suggests a rapid, mechanically-assisted interaction between iodine and the alloy surface. The subsequent disappearance of these flakes suggests that as the iodine is more uniformly distributed, the mechanical properties of the particles change, causing them to fracture more easily during milling, resulting in a smaller steady-state particle size.

Earlier work on mechanically milled Al-I_2 composite powders [37] did not explicitly reveal the formation of particular Al-I_2 phases, but did distinguish between "loosely" and "tightly" bound iodine, which may correspond to the respectively mechanically ductile and brittle products observed here.

The duration of the second milling stage required to achieve the desired particle size distribution was found to depend substantially on the material composition and on the cooling of the milling compartment. It was reported earlier that the temperature of the milling vial in an air-conditioned milling compartment was around 40-55 °C [96]. No temperature sensors were used in the present experiments; however, the effect of cooling was found to be significant based on experiments repeated at different times. Although the temperature in the laboratory housing the mill remained stable year-round, the humidity levels were substantially higher during summer and lower during winter. This affected the efficiency of the air conditioner, which yielded a noticeably lower temperature in the milling compartment during winter months. Respectively, it was observed that 65 min. was sufficiently long for the second milling stage for all materials during summer. However, during winter, 125 min. milling was required for the composition with 80 % Al and 185 min. was required for the one with 90 % Al in order to transfer formed flakes into equiaxial powder with the desired fine particle sizes.

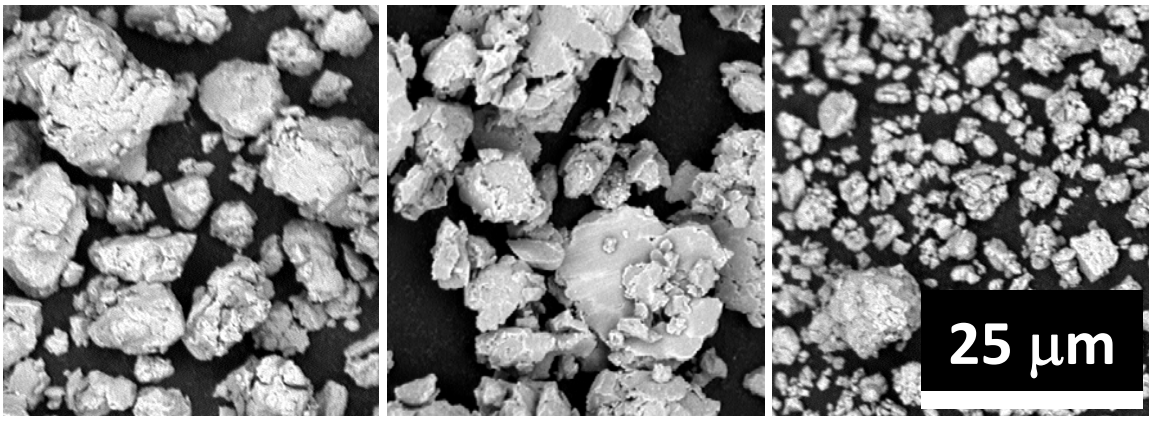

Figure 4.1 Particle evolution for an $Al_{0.7}Mg_{0.3}$ composite. Left: end of the first milling stage, center: immediately after the addition of iodine, right: final product after completion of the second milling stage.

4.3.2 Material Characterization

Scanning electron microscopy (SEM) was used to study powder morphology using a Phenom Tabletop Microscope by FEI Technologies Inc. Backscattered electron images were taken to inspect particle shapes and sizes. Particle size distributions of the prepared composites were measured with low-angle laser light scattering using a Beckman-Coulter LS230 Enhanced Particle Analyzer. Powder suspensions for analysis were prepared in ethylene glycol ($C_2H_6O_2$) and sonicated to minimize particle agglomeration. Phase compositions of the samples were analyzed using X-ray Diffraction (XRD) on a Phillips X'pert MRD powder diffractometer operated at 45 kV and 40 mA, using Cu K_α radiation (λ = 1.5438 Å). The patterns were collected between 10 and 85° at a rate of 0.625°/min.

Particle ignition temperatures were measured using a heated filament experiment described in detail elsewhere [29, 43]. A thin layer of powder was coated onto a nickel-chromium alloy wire (manufacturer-specified working temperature range up to 1953 K). The wire was heated by a DC current and its temperature was monitored optically using an infrared pyrometer focused on its uncoated surface adjacent to the powder coating.

Concurrently, light emission from the powder coating was measured using a photodiode sensor, in which a sharp onset of light emission was identified as the ignition instant. The temperature measured by the pyrometer at that instant was taken as the ignition temperature. Such experiments were conducted in air for a range of heating rates between 10^3 and 10^5 K/s. The ignition instant was also identified from videos recorded using a high-speed camera (MotionPro500 by Redlake) at 500 fps.

Combustion of aerosolized powders was studied using a constant volume explosion (CVE) setup. The details of the CVE experiments were described elsewhere [70-72]. The aerosolized powders were ignited from the center of a nearly spherical 9.2-L vessel. The vessel was initially evacuated, after which the powder was introduced with an air blast by opening a solenoid valve connecting the vessel with a chamber filled with compressed air. After the air blast, ignition was triggered following a delay of 300 ms, provided to reduce turbulence. The targeted initial pressure in the explosion vessel prior to ignition was 1 atm. Combustion pressure traces were recorded using both static and dynamic transducers. The measured pressures traces were normalized by the initial pressure in the vessel (P/P_0). The rates of pressure rise, $d(P/P_0)/dt$, were also reported for the prepared composites and for reference pure Al powder. (P/P_0) and $d(P/P_0)/dt$ are proportional to the flame temperature and combustion reaction rate, respectively [73].

Individual particle combustion was studied using an experimental setup where particles are ignited in a CO_2 laser beam, as described in detail in Refs. [74-77]. The powder was fed into the laser beam using a vibratory feeder described elsewhere [70, 90]. Ignited particle streaks were photographed; their emission was monitored using a set of four photomultiplier tubes (PMT, Hamamatsu H3164-10). The PMTs were equipped

with interference filters (486, 532, 568, and 589 nm). Emission signals filtered at 568 nm were used to determine particle burn times. Emission signals filtered at 532 and 589 nm were used for optical pyrometry. The 486 nm filter was selected to track one of the strongest AlO emission bands as an indicator of the intensity of the vapor-phase reactions. Because no substantial AlO emission occurs at 568 nm, the strength of the observed AlO emission was evaluated using the ratio of the signal intensities measured at 486 and 568 nm: $R_{AlO}=I_{486}/I_{568}$. Following Ref. [78], the measured ratio was normalized by its theoretical value calculated for respective intensities of a black-body emitter at the same temperature as the measured particle temperature. For each powder, the measured particle size distributions were obtained in terms of particle number densities in respective size bins then recast in terms of particle burn times as a function of their size. This data processing method was discussed in detail in Refs. [83, 95].

4.4 Results

4.4.1 Particle Sizes, Morphology, and Phase Composition

SEM images, such as shown in Figure 4.2, were used to preliminarily inspect the prepared powders. For all compositions, the images show fine, equiaxial particles with rounded shapes. No apparent detached Al and Mg particles are visible, indicating a homogeneous mixing between the two phases. Particle sizes for each composition are comparable to each other, indicating that the same milling protocol worked acceptably for all material compositions.

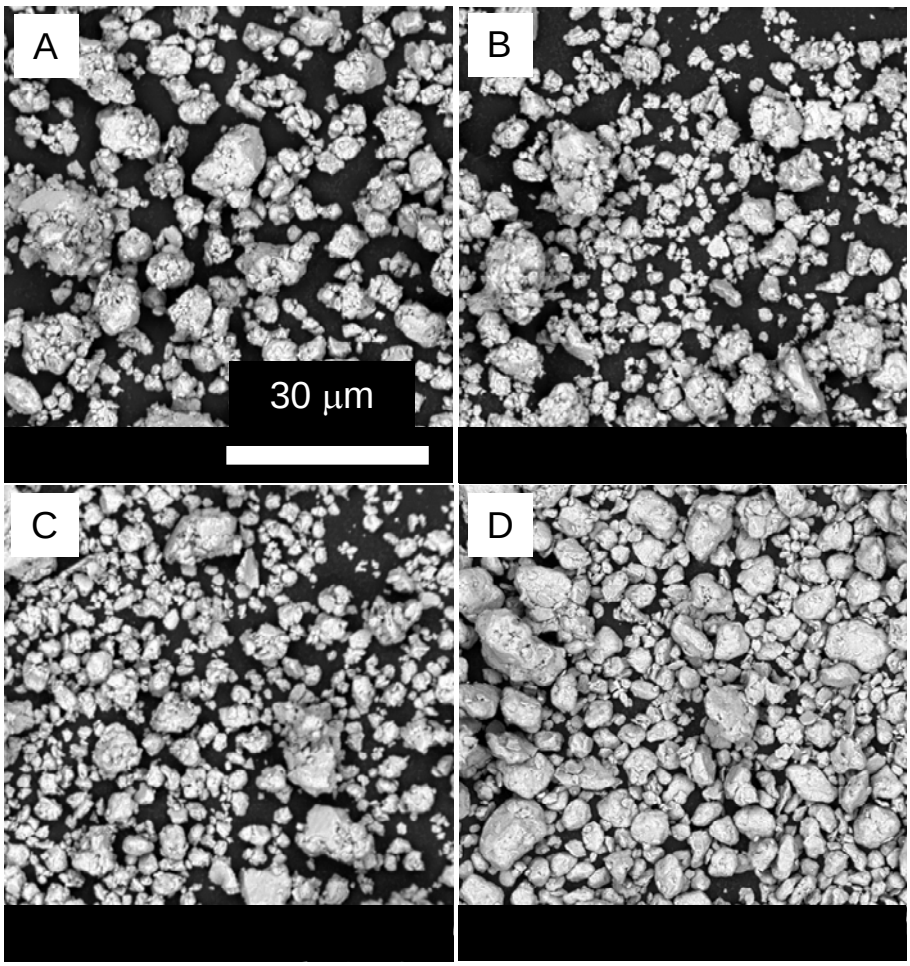

Figure 4.2 Back-scattered SEM images of powders of different Al/Mg compositions: 47/53 (A), 70/30 (B), 80/20 (C), and 90/10 (D).

Reduction in the particle sizes occurring during the second milling stage is illustrated in Figure 4.3 for the $Al_{0.47}Mg_{0.53}$ composition. Particle size distribution for the powders prepared in the 1st milling stage is compared to that for the same powder after the 2-stage milling. A clear reduction in particle size is observed. The powder prepared during the 1st milling stage has a mean volumetric size of ~23 μm. After the second (size reduction) milling stage, the powder has a mean volumetric size of 12.5 μm. The product of the 2-stage milling is shown on the top left image of Figure 4.2.

Particle size distributions for all prepared powders are shown in Figure 4.4. Also shown in Figure 4.4 is the size distribution of a pure Al powder used as a reference in the aerosol combustion experiments. For all mechanically alloyed powders, mean volumetric particle sizes are less than 13 μm. Different powder batches were prepared for each composition, and the particle size distributions shown in Figure 4.4 were observed to be well-reproducible.

X-ray diffraction (XRD) of the prepared composites shows that Mg is incorporated into the $Al_{12}Mg_{17}$ intermetallic phase mixed with the remaining pure Al [95] for the 47/53 compositions. With increasing Al concentrations, the peaks of the intermetallic phase decrease and elemental Al peaks become more prominent, as expected.

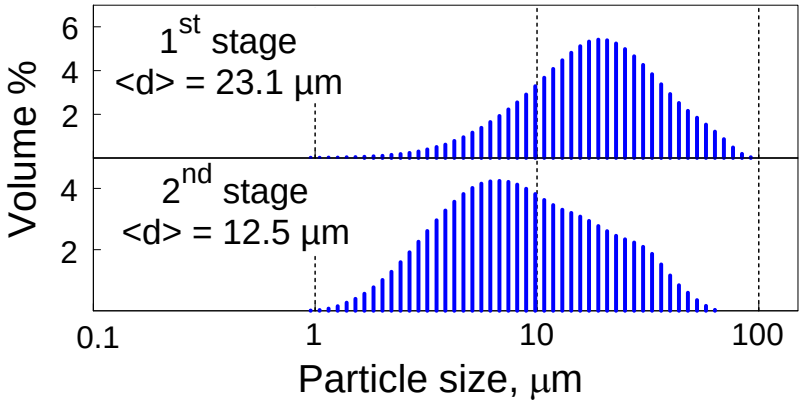

Figure 4.3 Particle size distributions showing products after the 1st milling stage (after 120 min.) and the 2-stage milling sample (after 185 min.) for $Al_{0.47}Mg_{0.53}$ powder.

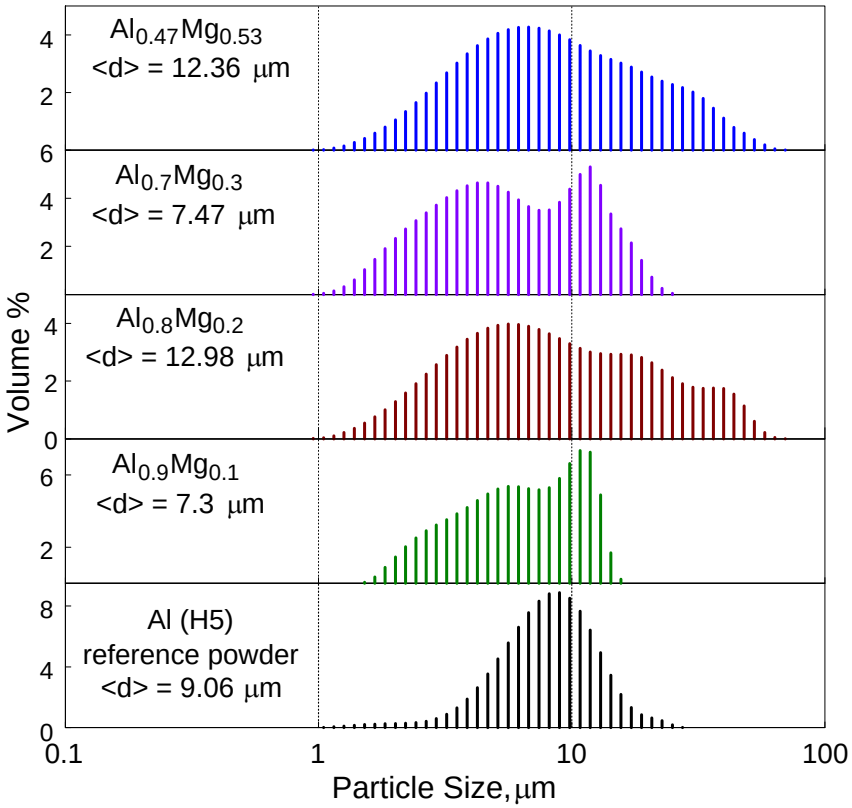

Figure 4.4 Particle size distributions showing final, 2-stage products of different Al/Mg powder compositions and reference Al powder (bottom) used in aerosol combustion experiments.

4.4.2 Ignition

Figure 4.5 shows the ignition temperatures of the prepared Al·Mg powders coated on an electrically heated filament as a function of heating rate. Each point represents an individual ignition experiment. As expected for a thermally activated ignition mechanism, ignition temperatures increase slightly with increasing heating rates. Ignition temperatures are approximately 860 K at lower heating rates and 1060 K for higher heating rates. These temperatures are somewhat higher than 783 K reported for an Al·Mg alloy with similar composition but ignited by slow heating in a furnace [65]. For comparison, the ignition temperature for pure Mg powder is also shown (as a dashed

line). Ignition temperatures of Al·Mg composites are much lower than ~1850 K reported for ignition of pure Al [48] at similar heating rates, and seem to be close to the ignition temperature of the pure Mg [43]. The reduced ignition temperatures are most likely due to the modified surface oxide formed on the surface of the alloy particles, which is less protective than Al_2O_3.

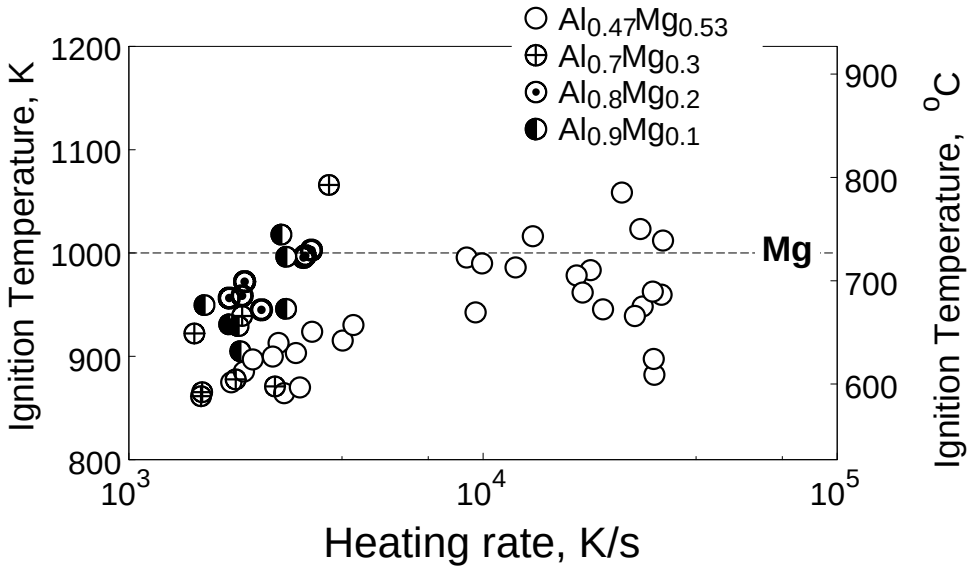

Figure 4.5 Ignition temperatures as a function of heating rate for mechanically-alloyed Al/Mg powders and reference values for elemental Al and Mg.

4.4.3 Aerosol Combustion

Figure 4.6 shows results of CVE experiments used to study the aerosol combustion characteristics of the prepared powders in terms of the normalized pressure, defined as P/P_0, where P is the measured pressure and P_0 is the pressure in the vessel before ignition. The value of P_0 was close to 1 atm for all runs. The maximum pressure, P_{max}, and the maximum rate of pressure rise, dP/dt_{max}, were obtained for each run as indicative

of the energy release and rate of reaction, respectively. The same initial mass loading of 4.65 g (corresponding to a fuel-rich mixture in the vessel) was used for all powders. To put the results in perspective, pure Al powder (H5 by Valimet) was also tested. Figure 4.6 shows that all the prepared Al/Mg compositions outperform pure Al in terms of both the maximum pressure and rate of pressure rise. It is also observed that all prepared Al·Mg composites ignite faster than pure Al, indicating shorter ignition delays—a characteristic often desired in reactive systems.

Comparing the Al/Mg powders to each other, there is an apparent pattern that can be observed for the 47/53, 70/30, and 90/10 compositions, showing an increase in the ignition delay with increasing Al concentrations. The 80/20 composition seems to fall outside of the general trend formed by other Al·Mg powders. This particular composition ignites much faster than the 70/30 composition. The maximum pressure for all the Al/Mg compositions appears to be hardly affected by the Al concentration, remaining for all powders higher than for the pure Al.

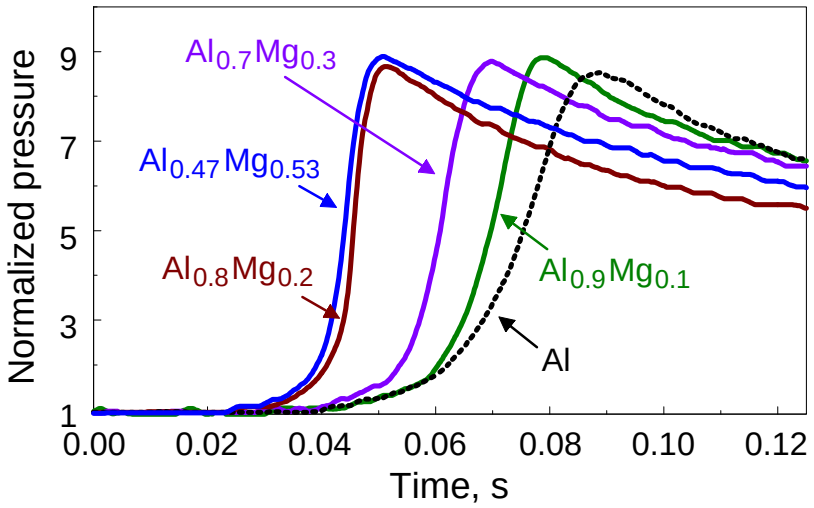

Figure 4.6 Normalized pressure traces for all prepared Al/Mg composites and reference Al powder. Igniter (hot wire in the center of the vessel) was initiated at the time equal to 0 s.

Table 4.1 shows the mean values of maximum pressure and rate of pressure rise for the prepared Al/Mg composites and reference Al powder. Standard deviation values were calculated from repeated experiments. Supporting data from Figure 4.6, Al·Mg powders show higher $(P/P_0)_{max}$ and $[d(P/P_0)/dt_{max}$ values than pure Al powder, indicating a higher flame temperature and combustion rate. For reference, explosion pressures calculated assuming the thermodynamic equilibrium for the constant volume combustion using experimental powder loads in air are shown in Table 4.1. Calculated adiabatic flame temperatures are also shown. The calculations used NASA CEA code [82], and Al·Mg alloys were treated as blended Al and Mg powders. Initial pressures were assumed to be 1 atm and the reactants were taken at room temperature. The comparison of calculated and experimental pressures shows that the experimental pressures are systematically lower than the pressures predicted by the thermodynamic equilibrium for all materials, as expected because of incomplete combustion and heat losses.

Table 4.1 Summary of CVE Experiment Results (Data Represent Average Values ± Standard Deviations)

Sample	$(P/P_0)_{max}$	$[d(P/P_0)/dt_{max}$; s^{-1}	P_{max} calculated; atm	T_{ad} calculated; K
$Al_{0.47}Mg_{0.53}$ <d> = 12.36 μm	9.02 ± 0.28	1135 ± 207	13.28	3900
$Al_{0.70}Mg_{0.30}$ <d> = 7.47 μm	8.87 ± 0.19	815 ± 124	12.95	3874
$Al_{0.80}Mg_{0.20}$ <d> = 12.98 μm	9.04 ± 0.64	1311 ± 116	12.97	3862
$Al_{0.90}Mg_{0.10}$ <d> = 7.3 μm	9.01 ± 0.15	594 ± 87	12.70	3849
pure Al (H5) <d> = 9.06 μm	8.54 ± 0.33	439 ± 105	12.41	3826

4.4.4 Single Particle Combustion

Photographs of burning particle streaks are shown in Figure 4.7 for the Al·Mg powders with different compositions. Particles were carried by a vertically rising air flow and crossed a CO_2 laser beam directed horizontally. The beam was focused to about 300 μm (0.3 mm) diameter and the laser power was set to 20 W, ensuring reliable ignition for all materials.

Several particle streaks observed in Figure 4.7 were produced by different particles fed successively through the laser beam during the time of exposure. Each well discerned streak represents a particle passing through the CO_2 laser beam. Most streaks include two separate bright portions and end with characteristic spearpoints (as illustrated in Figure 4.7), although this feature appears to diminish with increasing Al concentrations. Also, as the compositions near that of pure Al, the initial bright portion seems to diminish and a bright final portion of the streak becomes more prominent.

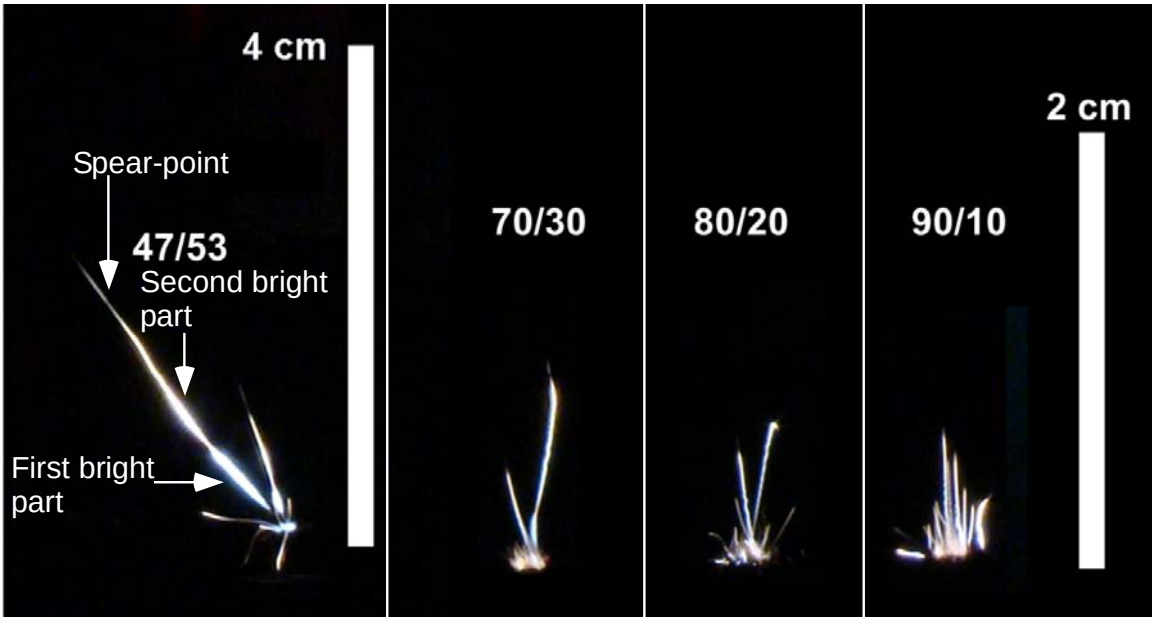

Figure 4.7 Burning particle streaks of Al·Mg powders prepared and ignited in the CO_2 laser beam. The scale bar for 70/30, 80/20, and 90/10 compositions is the same.

Typical emission traces measured at 568 nm, temperature traces obtained by 2-color pyrometry, and ratio R_{AlO} characterizing intensity of the molecular AlO emission for burning Al·Mg particles are shown in Figure 4.8. The ratio R_{AlO} is defined as the ratio of the measured emission signals at 486 and 568 nm over the same ratio of the emission signals calculated for a black body emitter. When a strong AlO line is observed at 486 nm, this ratio becomes greater than 1, indicating the vapor-phase combustion.

Consistent with the visible streaks in Figure 4.7, a strong, relatively narrow initial peak is also observed for emission traces in Figure 4.8, particularly for higher Mg concentrations. The first peaks correspond to higher temperatures and lower levels of AlO emission. The initial temperature increases are consistent with the emission intensity ramps. The first peak, clearly seen in the traces of particles with 47/53 and 70/30 Al/Mg ratio, becomes narrower and nearly disappears as the aluminum concentration increases. This first peak is followed by a second peak with a characteristic oscillatory emission pattern. This second peak is typically longer than the first one and comprises the entire emission signal for the particles with high Al concentrations.

For the particle size selected in Figure 4.8, (ca. 5 μm), the emission pulses decrease in duration with increasing Al concentrations. The effect of particle size on burn time for different prepared powders is further illustrated in Figure 4.9 and discussed below.

The measured temperatures and R_{AlO} ratios are observed to slowly decrease throughout the duration of the oscillatory emission pattern until the final small peak (corresponding to a "spearpoint" in the photograph) is observed. The overall emission

intensity level at which the spearpoints occur is substantially reduced compared to its peak value, so that both temperature and R_{AlO} measurements are no longer meaningful.

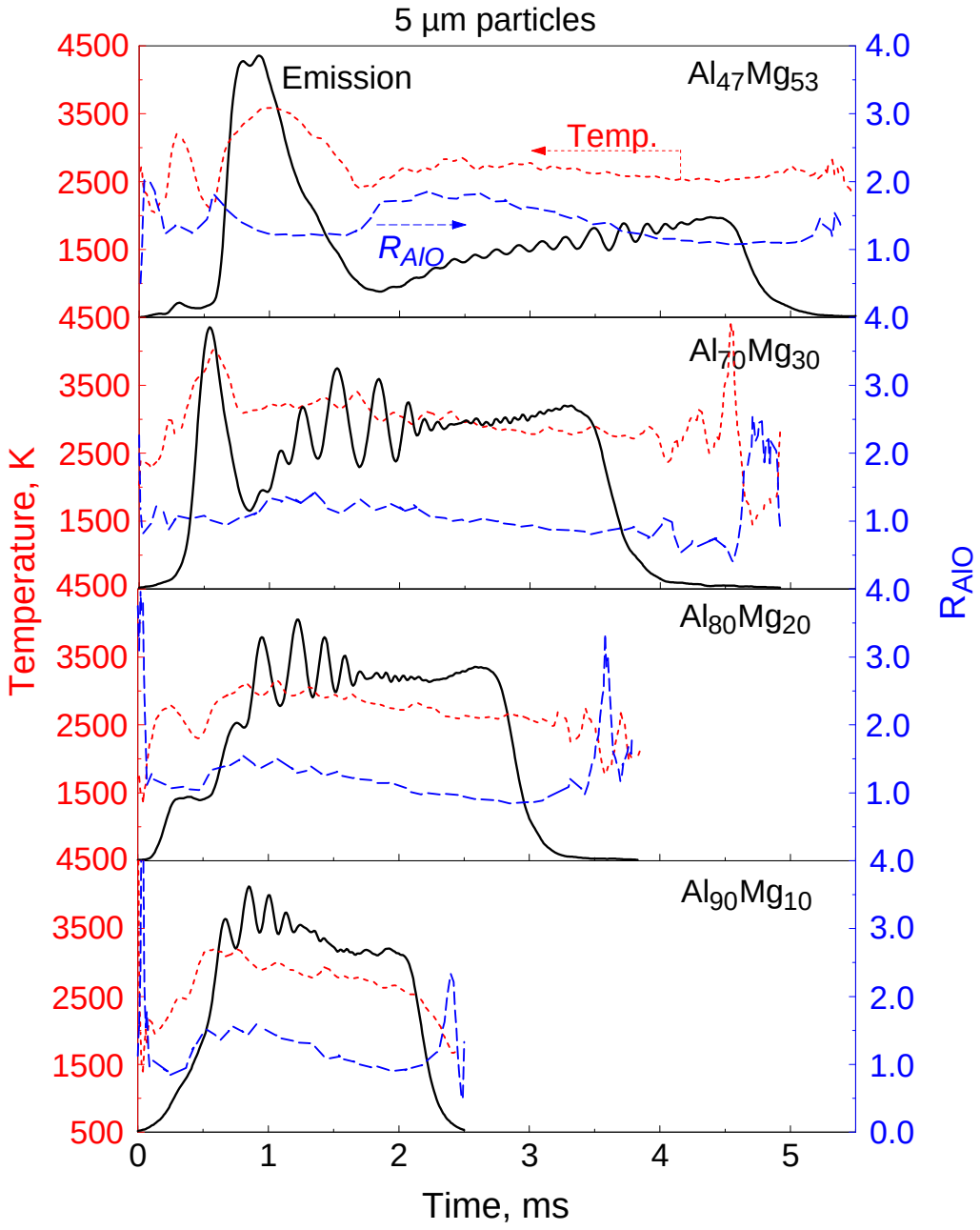

Figure 4.8 Emission signals (vertical scales in arbitrary units, axes not shown), temperatures, and intensity ratios characterizing significance of the molecular AlO emission for a single laser-ignited particle of mechanically-alloyed Al·Mg powders.

Slight delays in the ignition of Al·Mg particles can be observed in the photographs in Figure 4.7, i.e., luminous streaks do not always originate from the same area where the CO_2 beam was focused. These delays made it impossible to process the experimental data following the procedure outlined and used in Refs. [74-77], where the size of each particle was evaluated based on the amplitude of a light-scattering pulse, generated when particles crossed a low-power auxiliary laser beam placed just under the CO_2 laser beam. The poorly reproducible ignition timing made it impossible to correlate the light scattering and emission pulses and quantify the size of each ignited particle. Instead, the methodology described in Refs. [83, 95] was used to obtain a correlation between burn times and particle sizes. The main assumption in this data processing is that the larger size particles burn longer. First, recorded emission pulses were preliminarily inspected to remove overlapping or closely spaced signals, which may not represent individual particle combustion events. Durations of the downselected pulses were then measured. Second, the data on pulse durations representing burn times were logarithmically binned and correlated with the particle size distributions for the respective powders measured by Beckman-Coulter LS230 Enhanced Particle Analyzer. The volume-based particle size distributions shown in Figure 4.3 were transformed into number-based, cumulative distributions, and directly compared to the burn time data as explained previously. Once the size distributions were obtained in terms of particle number densities in respective size bins, the data were then recast in terms of particle burn times as a function of their size. The final burn times as a function of particle sizes are shown in Figure 4.9. For each powder, the obtained trend is overlapped with the trend obtained for a pure aluminum powder. The data for pure aluminum for Figures 4.9

– 4.11 were taken from measurements reported earlier [89] and re-processed following the present methodology to be directly comparable to the results for the Al·Mg powders.

For all alloyed powders, the results are well represented by $t \sim d^n$ trends (shown as solid lines), where t is the burn time, d is the particle diameter, and the exponent n is generally greater than 1. The observed effect of particle size on burn time is stronger for alloys than for aluminum. Generally, for finer particles the burn times for the Al·Mg alloys are shorter than for the pure Al. The size threshold for which the burn times for the alloyed powders become longer than for pure Al increases for alloys with greater Al concentrations: it is approximately 2 μm for the 47/53 Al/Mg composition, 4 μm for both 70/30 and 80/20 compositions, and 5 μm for the 90/10 composition.

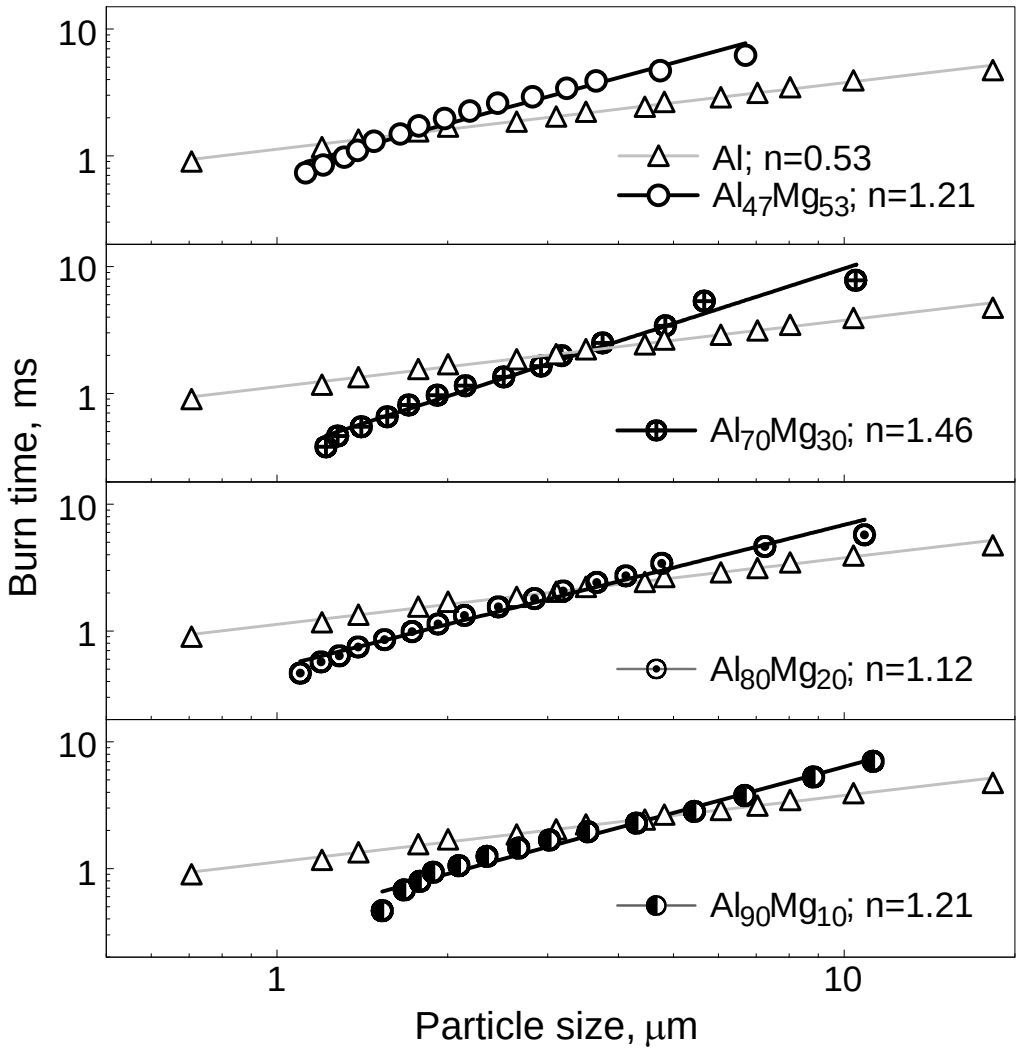

Figure 4.9 Particle burn time as a function of size for the mechanically-alloyed Al·Mg and for pure Al powders. Lines show respective $t \sim d^n$ fits.

The recorded traces of temperature and R_{AlO}, showing the intensity of molecular AlO emission, such as shown in Figure 4.8, were averaged for each particle and then among the particles in each pulse duration bin. For both parameters, average values were calculated for each burn trace for the period of time when the emission signal varied from 50% to 100% of its peak value, following the method described earlier [74-77]. Resulting average values of temperatures and R_{AlO} are shown in Figures 4.10 and 4.11, respectively. Note that such values do not represent the entire particle combustion event;

instead, they characterize the portion of the event with the strongest emission of the burning particle. The results are superimposed with the data for pure Al [89]. The error bars in Figures 4.10 and 4.11 show standard deviations from the average values for each point.

With increasing Al concentrations, temperatures appear to decrease and approach those reported for pure Al [74, 75, 89]. For all powders, despite substantial data scatter, a slight increase in temperature is observed for larger particle sizes. The scatter in the calculated average temperatures for Al·Mg powders could be attributed to the morphology of the as-milled powders as well as the ignition delays observed in Figure 4.7. For combustion of Al in air, R_{AlO} values greater than 1 indicate intensity of the vapor phase reactions. Values of R_{AlO} for Al·Mg powders are lower than those for pure Al, indicating a reduction in the importance of such vapor-phase reactions. For all Al·Mg powders prepared, R_{AlO} are lower than those reported for pure Al [74, 75, 89]. For each Al·Mg powder, R_{AlO} slightly increases with increasing particle sizes. The values of R_{AlO} appear to increase slightly for both the highest and lowest Al concentrations. Note that the emission signals change noticeably during each particle combustion event, so that the average temperatures and R_{AlO} values provide only very approximate information on the related reaction mechanisms. A more detailed analysis of the burning particle temperature histories may be considered in the future work.

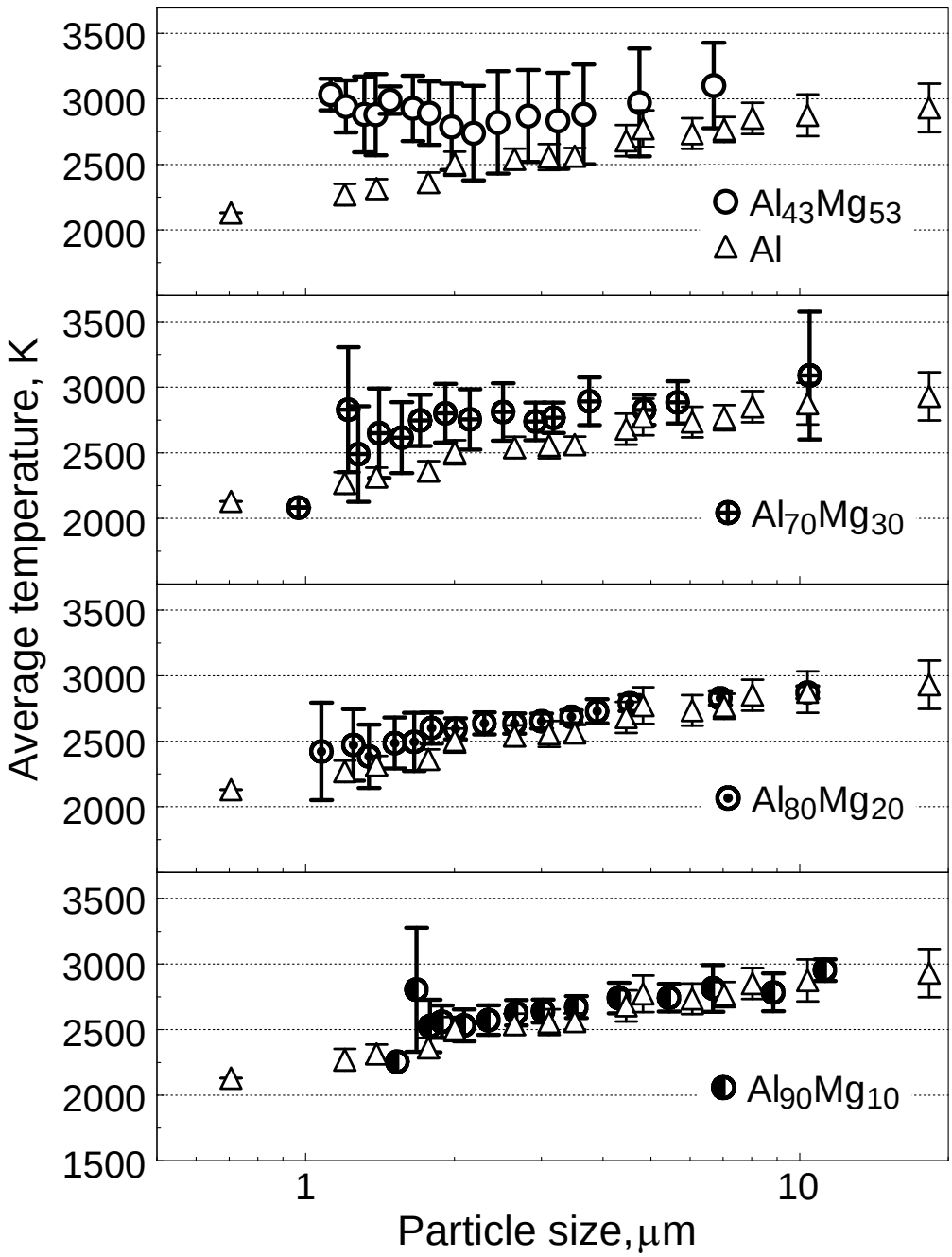

Figure 4.10 Combustion temperatures as a function of particle size for the mechanically-alloyed Al·Mg and for pure Al powders.

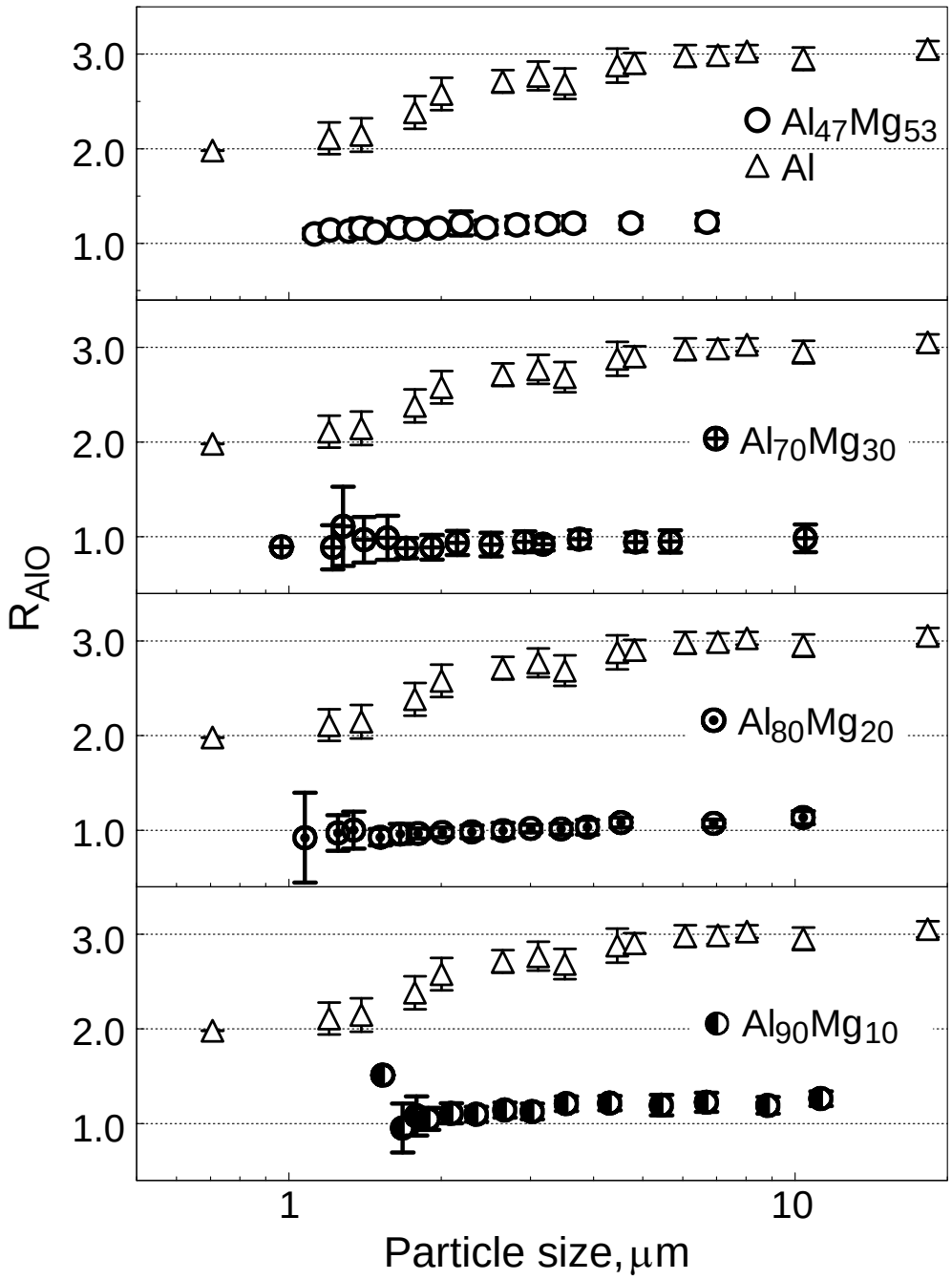

Figure 4.11 Normalized AlO ratio, R_{AlO}, values as a function of particle size for the mechanically-alloyed Al·Mg and for pure Al powders.

4.5 Discussion

Present experiments supported the use of iodine as a very effective PCA for mechanical alloying of Al·Mg powders with a broad range of compositions. The powder particle sizes are reduced effectively, even for the more Al-rich compositions (cf. Figures 4.1-4.4). The milling times required to achieve the desired fine particles are reasonably short, making the process amenable for practical applications. It is also shown that the 2-stage milling introduced previously [95] remains an effective approach for custom-tailoring particle sizes of the mechanically alloyed Al·Mg powders without inducing substantial changes in their structure and causing their contamination by milling tools. The inclusion of iodine may offer an added benefit for some of the reactive materials, resulting in formation of halogenated combustion products with biocidal properties. Such products are desired for applications aimed to improve inactivation of aerosolized spores and bacteria in a blast [84-87]. For some applications, e.g., propellants, addition of halogens to metal-based fuel additives may not be desirable although the amounts of added iodine are relatively small and may not result in appreciable corrosive effects of changes in handling and processing these fuel additives. Alternative techniques aimed at adjustment of the particle sizes of mechanically alloyed powders may involve different milling sequences and milling aides. For example, adding small amounts of hard particles, such as boron or silicon can be explored.

CVE results are generally consistent with a previous report of faster burn of Al·Mg alloys [30]. An improvement in both maximum pressure and rate of pressure rise for the prepared alloys as compared to the reference pure Al powder is significant in terms of possible practical applications of the developed material. Note that these

improvements are likely due to the achieved finer particle size for the mechanically alloyed powder, which became directly comparable to the reference aluminum. An improvement in the pressure traces measured in CVE experiments, as well as an overall accelerated burn rate reported earlier based on similar aerosol combustion experiments [30, 88], are likely caused by a combination of the lowered ignition temperature and nearly unchanged burn rate.

The combustion mechanisms of the prepared Al·Mg powders are clarified from the streaks and traces shown in Figures 4.7 and 4.8, respectively. A two-peak structure of the emission pulse suggests a 2-staged burn, most likely indicating an initial Mg-dominated combustion event followed by combustion of the remaining Mg-depleted Al, similar to earlier observations made for commercially available Al·Mg alloy particles burning in a H_2-O_2-Argon flame [97]. The Mg-dominated burning stage gradually disappears with increasing Al concentrations, as expected. The characteristic oscillatory pattern observed during stage II and typical of the Al particle combustion becomes shorter as the particle compositions approach that of the pure Al, as shown by the particle emissions traces in Figure 4.8 (for ca. 5 μm particles) and further supported by the trends shown in Figure 4.9. It is also interesting to compare the trends observed for particle burn times as a function of their diameters obtained in this work with similar trends reported previously [89, 95]. A stronger effect of particle sizes (diameter d) on their burn times (t) is observed here, i.e., $t=a\cdot d^{n,}$ with $n = 0.5$ for Al and $n \approx 1.2$, 1.5, 1.1, and 1.2 for prepared Al/Mg compositions 47/53, 70/30, 80/20, and 90/10, respectively. The values of both coefficient a and exponent n are summarized in Table 4.2. All exponents for alloys are greater than for the $t\sim d^{0.3}$ trend reported previously for Al and appear to be

more reasonable and amenable to a theoretical interpretation. It is unclear, however, why neither exponents *n* nor coefficients *a* given in Table 4.2 are changing consistently with the alloy composition. One possible explanation is that the two observed stages of particle combustion, one dominated by Mg and the other by Al, are not independent of each other. It is possible that the combustion mechanisms for the two stages change as a function of the alloy composition. If confirmed in future work, such complex effects can be used to adjust the alloy composition in order to carefully tailor the performance of the produced powder depending on the specific practical requirements.

A slight increase in the average flame temperature for greater particle sizes and for increased Al content is likely associated with an increased importance of the stand-off vapor phase flame for larger particles as discussed previously [90, 95].

Somewhat higher R_{AlO} values observed for the lowest and highest Al concentrations (Figure 4.11), may indicate a growing effect of the vapor phase reactions for the powder that is the most similar to pure Al, and for the powder with the most vigorous combustion assisted by Mg, respectively.

Future work is desired to investigate kinetics of intermetallic reactions and heterogeneous oxidation for the mechanically alloyed powders, so that the mechanisms of such low-temperature exothermic processes can be correlated with their respective ignition mechanisms, mostly responsible for their improved combustion performance. Preliminary experiments, which are not discussed in the present manuscript, indicate that the preparation of these powders can still be modified to further improve their combustion characteristics. The improvements are mostly attributable to further reduction of particle sizes and reduction in the agglomeration of the prepared

mechanically alloyed powders. Note that the improvements mentioned here are incremental and may be addressed once detailed requirements for such powders are identified based on specific applications.

Table 4.2 Burn Time and Size Power Law Correlations Showing Values for Coefficient *a* and Exponent *n* in Rate Law, $t=ad^n$. (*t* in ms, *d* in μm).

Sample	$t=ad^n$	
	a	**n**
$Al_{0.47}Mg_{0.53}$	0.77	1.21
$Al_{0.70}Mg_{0.30}$	0.35	1.46
$Al_{0.80}Mg_{0.20}$	0.52	1.12
$Al_{0.90}Mg_{0.10}$	0.39	1.21
pure Al (H5)	1.13	0.53

4.6 Conclusions

Preparation of mechanically alloyed Al·Mg powders with a broad range of compositions and with desired fine particle sizes and shapes is feasible using a modified, 2-stage milling technique that allows for a simultaneous adjustment in both internal structures and particle size distributions. Particles suitable for laboratory evaluations of their oxidation, ignition, and combustion characteristics were prepared and characterized. Aluminum concentration varied from less than 50 to 90 at. %. Electron microscopy, x-ray diffraction patterns, and particle size distribution measurements showed that fine, equiaxial Al·Mg particles with homogeneously mixed components and mean sizes

between 7 - 13 μm can be prepared reproducibly. Ignition temperatures for all prepared alloys are much lower than those of pure Al powders and are close to those of Mg. Powders were aerosolized and ignited in air; the powder cloud combustion experiments showed that a higher maximum pressure, greater rates of pressure rise, and shorter ignition delays can be achieved for the mechanically alloyed powders, as compared to the pure Al powders with directly comparable particle size distributions. Individual particle combustion experiments show that the mechanically alloyed particles burn in two stages, while the first stage is gradually disappearing with an increased Al concentration. The effect of particle size, d, on its burn time, t, for the prepared alloys is relatively well described by a $t \sim d^n$ law, where n is varying in the range of 1.1 - 1.5 for different compositions. It is observed that for particles greater than a few μm, the overall burn time decreases slightly with an increase in the aluminum concentration. The gas phase reactions resulting in production of molecular AlO emission are weaker for the prepared powders than for pure Al, but become increasingly more important as compositions approach that of pure Al. The maximum flame temperatures of the prepared mechanically alloyed powders are the same or higher than for pure Al powders with similar size distributions.

CHAPTER 5

IGNITION AND COMBUSTION OF AL·MG ALLOY POWDERS PREPARED BY DIFFERENT TECHNIQUES

5.1 Abstract

Alloys of aluminum and magnesium have long been explored as potential reactive materials and replacements of pure aluminum powders in energetic formulations. It has been recently shown that mechanical alloying (MA) can be used to prepare a range of Al·Mg powders with different compositions and particle sizes. Conventionally, such alloys are prepared by melt processing; however, no direct comparisons of combustion characteristics of such alloys prepared using different methods are available. This work is aimed at comparing the oxidation, ignition, and combustion characteristics between two powders of Al•Mg with similar bulk compositions and particle sizes: one produced via MA, and another, produced via grinding of a cast alloy. Particle size distributions are measured using low-angle laser light scattering. Electron microscopy and x-ray diffraction are used to examine particle morphology and phase makeup, respectively. Thermal analysis is used to identify the low-temperature reactions that could affect ignition. Ignition behavior of the two powders is studied using a heated filament ignition apparatus. Constant volume explosion experiments are performed to compare effectiveness and rate of combustion of aerosolized alloy particles. A laser ignition setup is used to characterize combustion rates and temperatures for individual alloy particles. Low-temperature exothermic features were observed for the MA powder but not for the cast-alloyed powder in thermo-analytical experiments. MA powders had slightly lower ignition temperatures than cast-alloyed powders. Aerosol combustion experiments

showed a substantial increase in both the maximum pressure and rate of pressure rise for the MA powders as compared to the cast alloyed powders. In single particle laser ignition experiments, MA particles ignited more readily than cast alloyed particles. MA powders burned in a staged sequence, with the first stage dominated by combustion of Mg and the second stage representing primarily combustion of Al. No similar staged combustion behavior was observed for the cast-alloyed powders, which generated very short emission pulses with a relatively low brightness, and thus might not have burned completely. It is proposed that the difference in the structure and morphology between the MA and cast alloyed particles results in different ignition and combustion scenarios.

5.2 Introduction

Metals and alloys offer advantageous performance as fuel additives in energetic formulations such as propellants, explosives, and pyrotechnics [9-11, 50, 51]. Recent research is focused on aluminum-based materials that exhibit an enhanced reactivity compared to pure Al powders. The reduced ignition delays, faster burn rates, and tailored densities in alloys, including Al·Mg, Al·Ti, etc. make them attractive fuel additives [15, 16, 28-31, 42]. Specifically, Al·Mg alloys have long been explored for applications in energetic materials. Aluminum offers its high combustion enthalpy and temperature while Mg is thought to accelerate ignition. Some of the early applications were in pyrotechnic formulations [60-62] while more recently, such alloys were successfully added to propellants [63]. It has been reported that Al·Mg alloys ignite at much lower temperatures than pure Al [64, 65]. Combustion of Al·Mg alloys was also studied, with most detailed experimental observations on coarse particles with dimensions exceeding 100 μm [34, 66, 67]. It was proposed that depending on

composition, either Al or Mg determine the alloy combustion dynamics [68]; alternatively, a staged combustion behavior was described, in which Mg combustion preceded that of Al [69].

Recently, mechanically alloyed (MA) powders of Al·Mg were prepared with various compositions and tunable, fine particle sizes [95, 98]. Investigations into the combustion characteristics of these powders showed that lower ignition temperatures, shorter burn times, higher combustion temperatures, and reduced ignition delays can be achieved compared to pure Al powders.

Despite significant interest to combustion characteristics of Al·Mg alloys [34-36, 95, 98], the quantitative information regarding their burn rates and combustion temperatures remains limited. In particular, there is no side-by-side comparison of combustion characteristics of such alloys prepared using different techniques, e.g., MA [30, 95, 96, 98] vs. cast alloyed powders available commercially. Both materials may contain the same bulk Al·Mg compositions; however, the structures and phase compositions may be different. MA powders are likely to contain nanocomposite structures and poorly crystalline solid solution phases. Conversely, cast-alloyed powders are expected to contain well-crystallized intermetallics. The effect of such structural and morphological differences on the ignition and combustion of alloys is unknown. This work compares an Al·Mg powder prepared by mechanical alloying with a commercially available cast alloyed powder; the powders have identical bulk compositions and similar particle size distributions.

5.3 Materials

5.3.1 Material Selection and Synthesis

Two Al·Mg powders with the same 1/1 Al/Mg mass ratio were used. The first powder, referred to as "cast alloy", was provided by Matsys Corporation and prepared by grinding of a commercially available cast alloy. The second powder was prepared via mechanical milling using starting materials of elemental powders of Al (Atlantic Equipment Engineers, 99.8% pure, -325 mesh) and Mg (Alfa-Aesar, 99.8% pure, -325 mesh). Powders were milled using a Retsch PM-400 MA planetary mill equipped with an air conditioner. Powders of Al and Mg were loaded in steel milling vials in argon. 9.5 mm-diameter hardened steel milling balls were used. The powder charge was 30 g per vial and the ball to powder mass ratio was 10. A rotational speed was set to 350 rpm for 120 min. The rotation direction was changed every 15 min. 50 ml of hexane (C_6H_{14}) was added to each milling vial as a PCA. This preparation has been described previously [95, 98].

5.3.2 Material Characterization

Scanning electron microscopy (SEM) was used to study powder morphology using a Phenom Tabletop Microscope by FEI Technologies Inc. Backscattered electron images were taken to inspect particle shapes and sizes. Particle size distributions of the prepared composites were measured with low-angle laser light scattering using a Beckman-Coulter LS230 Enhanced Particle Analyzer. Powder suspensions for analysis were prepared in ethylene glycol ($C_2H_6O_2$) and sonicated to minimize particle agglomeration. The surface area of the powders was measured using a Quantachrome Monosorb BET surface area analyzer. Phase compositions of the samples were analyzed using X-ray Diffraction

(XRD) on a PANalytical Empyrean diffractometer equipped with a position sensitive detector operated at 45 kV and 40 mA using Cu K_α radiation (λ=1.5438˚ A). A spinning-stage sample holder was used for all XRD measurements at scan angles ranging from 5 to 90°.

Particle ignition temperatures were measured using a heated filament experiment described in detail elsewhere [42, 43]. A thin layer of powder was coated onto a nickel-chromium alloy wire (manufacturer-specified working temperature range up to 1953 K). The wire was heated by a DC current and its temperature was monitored optically using an infrared pyrometer focused on its uncoated surface adjacent to the powder coating. Concurrently, light emission from the powder coating was measured using a photodiode. A sharp onset of light emission was identified as the ignition instant. The temperature measured by the pyrometer at that instant was taken as the ignition temperature. Such experiments were conducted in air for a range of heating rates between 10^3 and 10^5 K/s. The ignition instant was also identified from videos recorded using a high-speed camera (MotionPro500 by Redlake) at 500 fps.

Combustion of aerosolized powders was studied using a constant volume explosion (CVE) setup. The details of the CVE experiments were described elsewhere [70-72]. The aerosolized powders were ignited from the center of a nearly spherical 9.2-L vessel. The vessel was initially evacuated, after which the powder was injected with an air blast, which also filled the vessel to $P_0 \approx 1$ atm. The blast was produced by opening a solenoid valve connecting the vessel with a chamber filled with compressed air. After the air blast, ignition was triggered following a delay of 300 ms, provided to reduce turbulence. An electrically heated tungsten wire serves as an igniter. Combustion

pressure traces were recorded using both static and dynamic transducers. The measured pressures traces were normalized by the initial pressure in the vessel (P/P_0). The rates of pressure rise, $d(P/P_0)/dt$, were also obtained for the prepared composites and for reference pure Al powder. Values of (P/P_0) and $d(P/P_0)/dt$ are roughly proportional to the flame temperature and combustion reaction rate, respectively [73].

Individual particle combustion was studied using an experimental setup where particles are ignited in a CO_2 laser beam, as described in detail in Refs. [74-77]. The powder was fed into the laser beam using a vibratory feeder described elsewhere [77, 99]. Ignited particle streaks were photographed; their emission was monitored using a set of three photomultiplier tubes (PMTs), two Hamamatsu R3896-03 and one R636-10. The PMTs were equipped with interference filters (700, 800, and 900 nm). The powder flow was illuminated by an auxiliary 785-nm laser diode and the PMT filtered at 800 nm picked up the scattered signal. For particles, which did not ignite only a scattered 800-nm signal was collected, with no simultaneous emission signals at 700 and 900 nm. Thus, a fraction of ignited particles was determined for each powder. Emission signals filtered at 700 nm were used to determine particle burn times. Emission signals filtered at 700 and 900 nm were used for optical pyrometry. For each powder, the measured particle size distributions were obtained in terms of particle number densities. The particle size distributions were correlated with the measured distribution of the particle burn times to obtain the burn time as a function of the particle size. This data processing method was discussed in detail elsewhere [98, 100].

5.4 Results

5.4.1 Particle Morphology, Sizes, and Phase Composition

SEM images, such as shown in Figure 5.1, were used to inspect the mechanically and cast-alloyed powders. The powder particle sizes are comparable for both powders, while the MA powder appears to have a broader particle size distribution. This is further evidenced by the measured particle size distributions shown in Figure 5.2. The mean volumetric size for the MA powder is 36.5 μm. The cast alloy powder has a more narrow distribution with a mean volumetric size of ~24 μm. For the MA powder, no apparent detached Al and Mg particles are visible, indicating a homogeneous mixing between the two phases. Also shown in Figure 5.2 are size distributions for sieved MA powders used for combustion experiments. A 25-μm sieve was used to classify the powder. The mean volumetric particle sizes for the fine and coarse fractions are ~14 and 49 μm, respectively. The measured BET surface areas were respectively 0.5 and 0.3 m^2/g, for the MA and cast-alloyed powders, supporting SEM and the size distribution measurements showing comparable particle sizes for both powders.

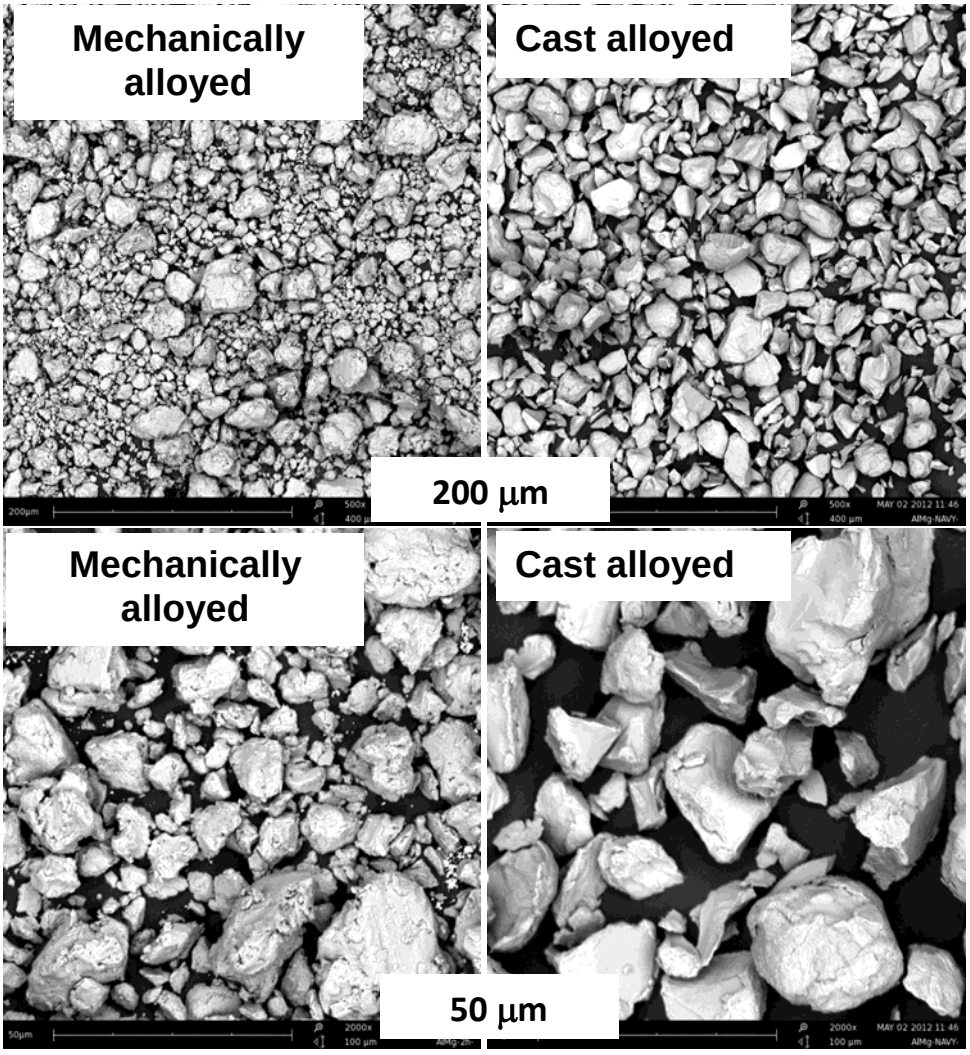

Figure 5.1 SEM images of Al·Mg powders: MA (left) and cast alloyed (right) powders. The images on the bottom row show higher magnifications of the respective powders.

X-ray diffraction (XRD) patterns for both powders are shown in Figure 5.3. Also shown in Figure 5.3 is pattern for a blend of Al·Mg. The cast alloyed powder shows complete presence of $Al_{12}Mg_{17}$ intermetallic phase with no other phases present. For the MA powder, a strong background indicative of the poorly crystalline phases is apparent. The pattern shows that Mg is only partially incorporated into the $Al_{12}Mg_{17}$ intermetallic phase mixed with the remaining pure Al and Mg [95].

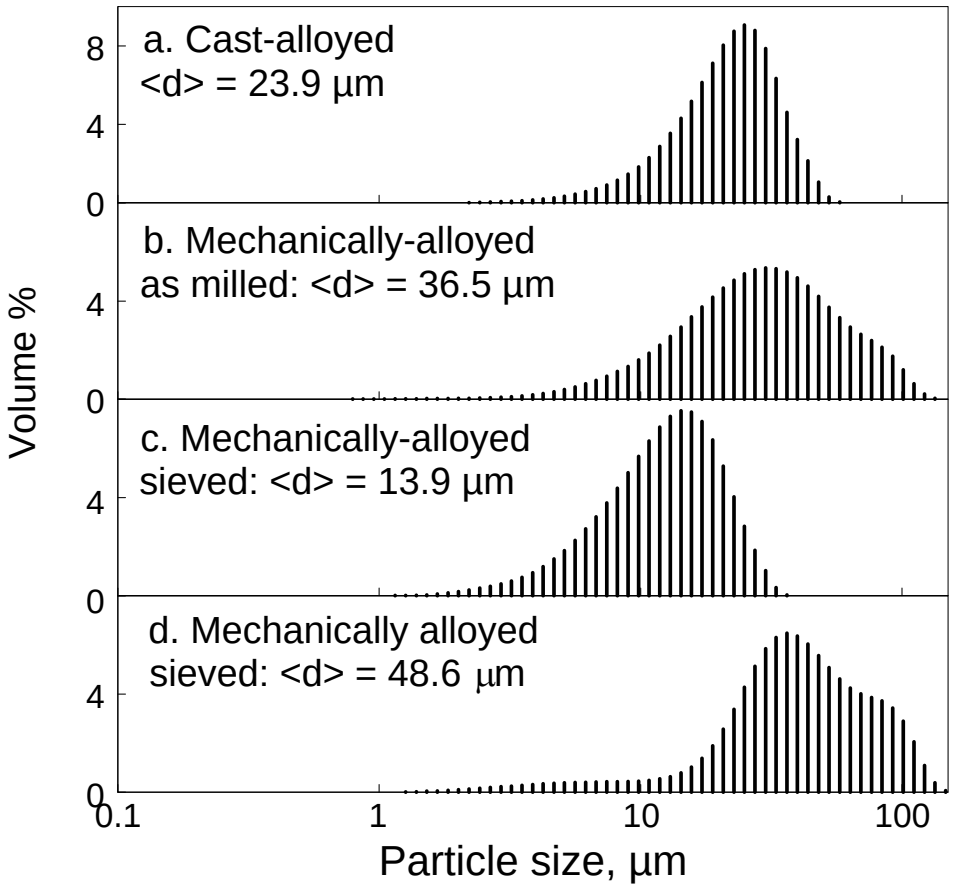

Figure 5.2 Particle size distributions for as-milled MA and as-received cast alloy powders. Also shown are the size distributions of MA powders used in combustion experiments.

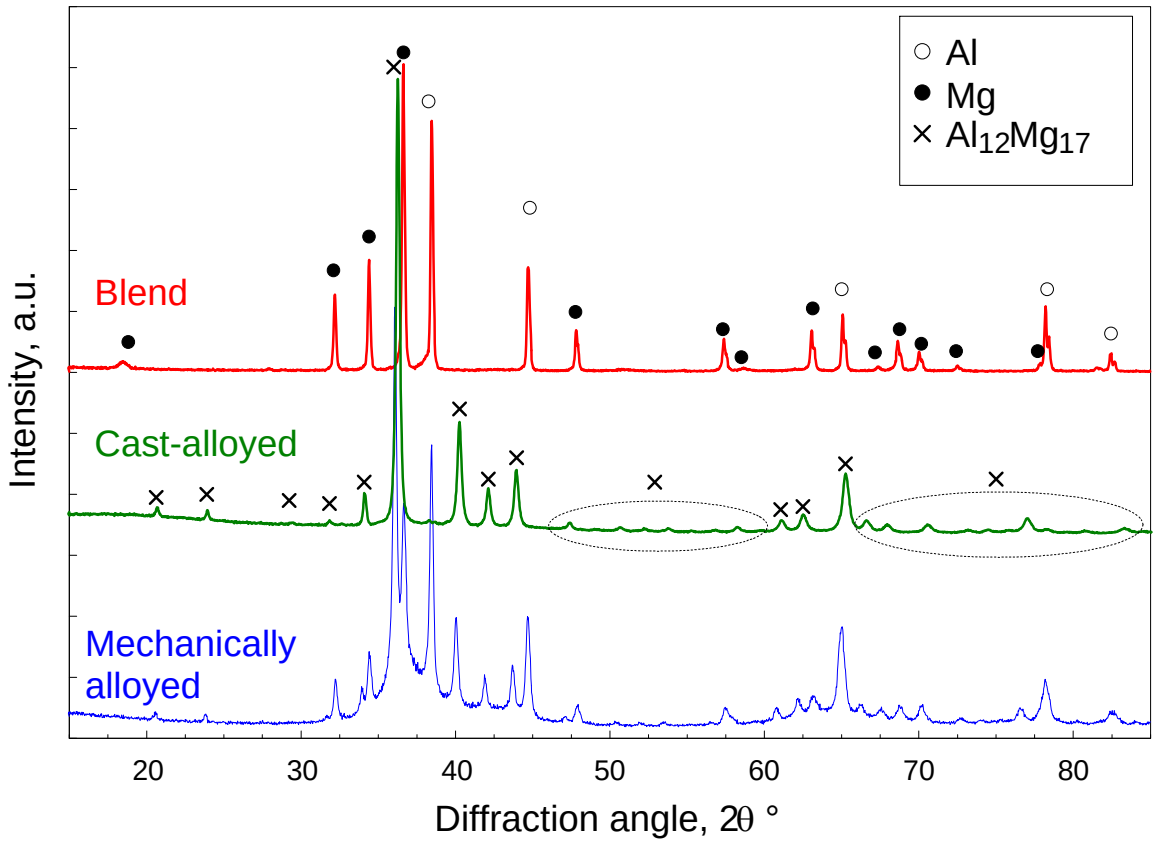

Figure 5.3 XRD patterns of an Al-Mg blend, MA and cast alloyed powders. Elemental Al and Mg phases are indicated in the plot. All other (unlabeled) peaks correspond to the γ - $Al_{12}Mg_{17}$ phase.

5.4.2 Ignition

Figure 5.5 shows ignition temperatures of the alloyed Al·Mg powders coated on an electrically heated filament as a function of the heating rate. Each point represents an individual ignition experiment. For the MA powder, ignition temperatures show a scatter at low heating rates. At higher heating rates, ignition temperatures fall between 925-1025 K. For the cast alloy, ignition temperatures range from 950-1175 K for the range of heating rates shown. In general, the ignition temperatures for MA are slightly lower than for the cast alloyed powders.

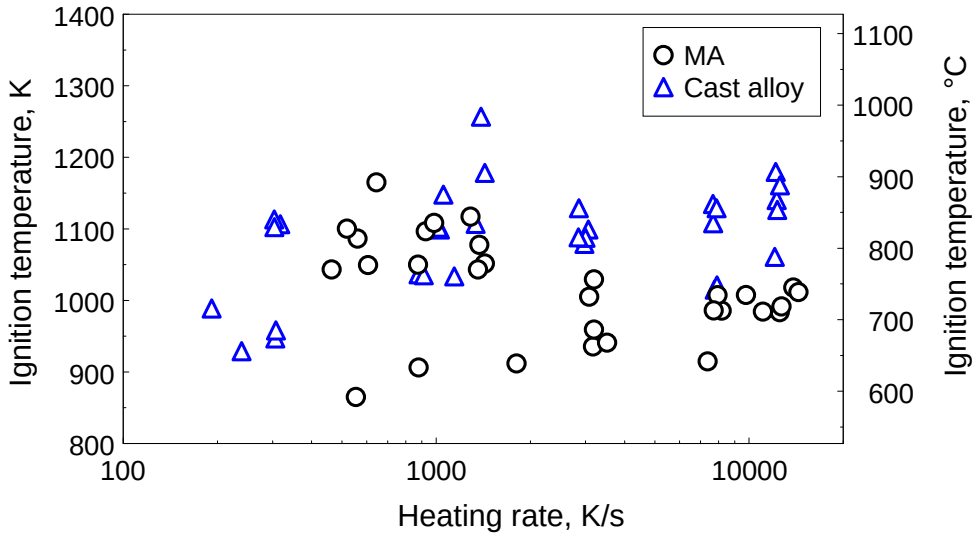

Figure 5.4 Ignition temperatures as a function of heating rate for MA and cast alloy powders.

5.4.3 Thermal Analysis

Baseline corrected DSC traces for the samples heated in argon at 5 K/min are shown in Figure 5.5. For the MA powder, weak exothermic features are seen where sub-solidus reactions are expected. The first exothermic peak with a maximum at ~110 °C and another with a maximum at ~ 260 °C are similar to the features reported in more detailed earlier measurements for the MA Al-Mg powders [33, 79]. The cast alloy powder shows no features in the DSC trace in this low-temperature region. Heating to higher temperatures in DSC for both powders showed eutectic melting at ~ 450 °C (~ 723 K).

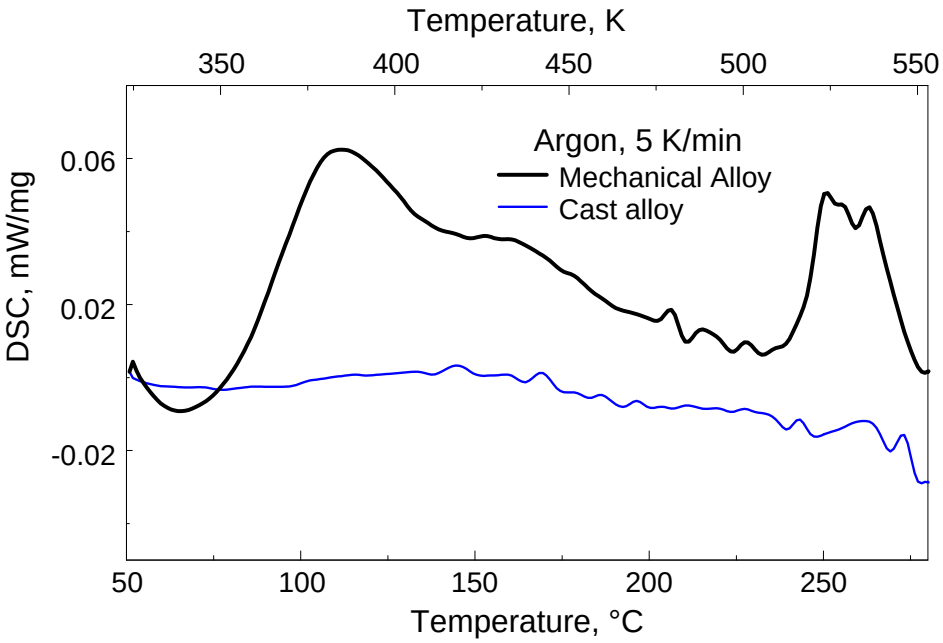

Figure 5.5 DSC traces for MA and cast alloyed powders heated in argon at 5 K/min.

5.4.4 Aerosol Combustion

Figure 5.6 shows characteristic pressure traces recorded in CVE experiments for both materials. The time zero corresponds to the initiation of the igniter. MA powder outperforms the cast alloyed powder in terms of both the maximum pressure and rate of pressure rise. The MA powder ignites faster than the cast alloy, resulting in a shorter ignition delay—a characteristic often desired in reactive systems.

The maximum pressure, P_{max}, and the maximum rate of pressure rise, dP/dt_{max}, were obtained for each run as indicative of the energy release and rate of reaction, respectively. The same initial mass loading of 4.65 g (corresponding to a fuel-rich mixture in the vessel) was used for all powders.

Table 5.1 shows the mean values of maximum pressure and rate of pressure rise for the mechanically and cast alloyed powders. Standard deviation values were calculated from repeated experiments. Supporting data from Figure 5.6, the MA powder

shows higher $(P/P_0)_{max}$ and $[d(P/P_0)/dt_{max}$ values than the cast alloyed powder, indicating a higher flame temperature and combustion rate.

To verify whether the difference between MA and cast alloyed powder is primarily driven by the difference in the particle size distribution, an additional MA powder batch was prepared and size classified using a 25 μm sieve. The initial size distribution of the new batch was identical to that shown in Figure 5.2b. The size distributions for the size classified MA powder fractions are shown in Figure 5.2c and d. Experiments with the size classified MA powders showed the same or even greater maximum pressures and rates of pressure rise as with the initial powder (See Table 5.1). An improvement in the pressure readings is likely associated with a shorter time passed from the powder preparation to its testing in CVE (as shown in Table 5.1). While the aging of the prepared Al·Mg alloys may be a concern for the future studies, the experiments with the size classified MA powders show clearly that the particle size is not the dominant factor explaining a better performance of MA compared to the cast alloyed powders.

For reference, explosion pressures calculated assuming the thermodynamic equilibrium for the constant volume combustion using experimental powder loads in air are also shown in Table 5.1. Calculated adiabatic flame temperatures are also shown. The calculations used NASA CEA code [82], and Al·Mg alloys were treated as blended Al and Mg powders. Initial pressures were assumed to be 1 atm and the reactants were taken at room temperature. The comparison of calculated and experimental pressures shows that the experimental pressures are systematically lower than the pressures

predicted by the thermodynamic equilibrium for all materials, as expected because of incomplete combustion and heat losses.

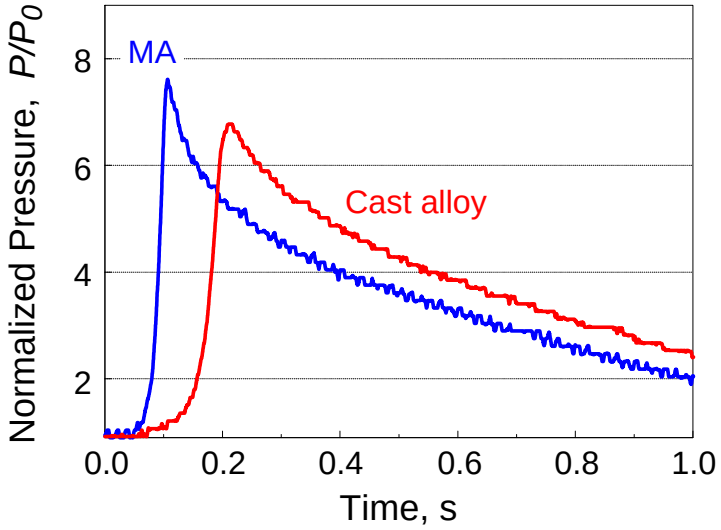

Figure 5.6 Normalized pressure as a function of time for MA and cast alloy powders ignited in CVE.

Table 5.1 Summary of CVE Experiment Results (data represent average values ± standard deviations).

Sample	**Age of MA powders used in experiment, months**	**$(P/P_0)_{max}$**	**$[d(P/P_0)/dt]_{max}$; s^{-1}**	**P_{max} calculated; atm**	**T_{ad} calculated; K**
MA	4	7.55 ± 0.22	326 ± 53	13.5	3915
MA: size classified; <25 μm	1.5	9.22	1035		
MA: size classified; >25 μm	1.5	7.92 ± 0.34	452 ± 70		
Cast alloyed	-	6.84 ± 0.49	169 ± 52		

5.4.5 Single Particle Combustion

Photographs of burning particle streaks are shown in Figure 5.7 for both MA and cast alloyed powders. Particles were carried by a vertically rising air flow and crossed a CO_2 laser beam directed horizontally. The beam was focused to about 300 μm (0.3 mm) diameter and the laser power was set to 20 W.

Several particle streaks observed in Figure 5.7 were produced by different particles fed successively through the laser beam during the time of exposure. Each well discerned streak represents a particle passing through the CO_2 laser beam. For the MA powder, most streaks emit bright light immediately exiting the laser beam. After the initial bright portion, an oscillatory feature is prominent in most of the streaks, as illustrated in Figure 5.7. For the cast alloyed powder particle streaks, no bright emission is observed immediately after particles exit the CO_2 laser beam. The streaks become bright later on; however, oscillatory emission patterns are not observed. Visually, the streaks produced by the cast alloyed powder appear dimmer compared to the MA powder streaks.

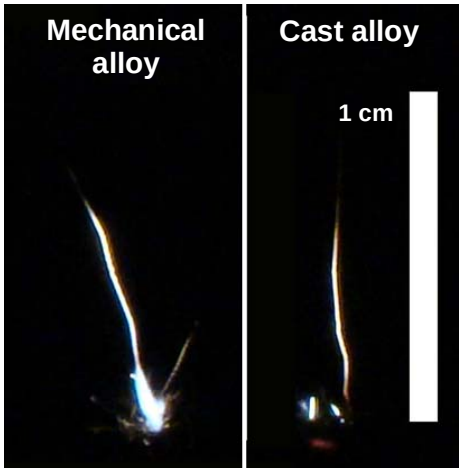

Figure 5.7 Burning particle streaks of Al·Mg powders prepared by mechanical and cast alloying ignited in the CO_2 laser beam.

For each experiment, a sequence of emission peaks was recorded, representing emission produced by individual particles. Fragments of such records for both MA and cast alloyed powders are shown in Figure 5.8. Emission was simultaneously measured by three filtered PMTs; respectively, three traces are shown for each material. The 800-nm signal is amplified by the light particles scattered from the 785-nm laser diode, while both 700 and 900-nm filtered signals are observed only for incandescent particles.

For the MA powder, most emission peaks are observed simultaneously for all three filtered signals, confirming emission from the ignited particles. Conversely, for the cast alloyed powders only some of the pulses were simultaneously observed for all three signals. Many pulses observed in the trace filtered at 800 nm were not accompanied by simultaneous pulses in the other two recorded filtered traces. Such pulses were assigned to particles that did not ignite. To quantify the difference between the two powders, several one-second records (selected to include multiple emission peaks) were taken and the percent of particles that ignited (i.e., exhibited all three simultaneous filtered emission peaks compared to all particles producing 800-nm filtered emission peaks) were calculated. For the MA powder, nearly 84 % of all particles passing the laser beam ignited compared to only 47 % of particles for the cast alloy.

The pulse shapes were also remarkably different for the two materials. For MA particles, most pulses have characteristic two-peak structure with an oscillatory pattern, consistent with the photographed emission streaks. For cast alloyed particles, no two-peak pulses were detected; the pulses were short and showed no brightness oscillations.

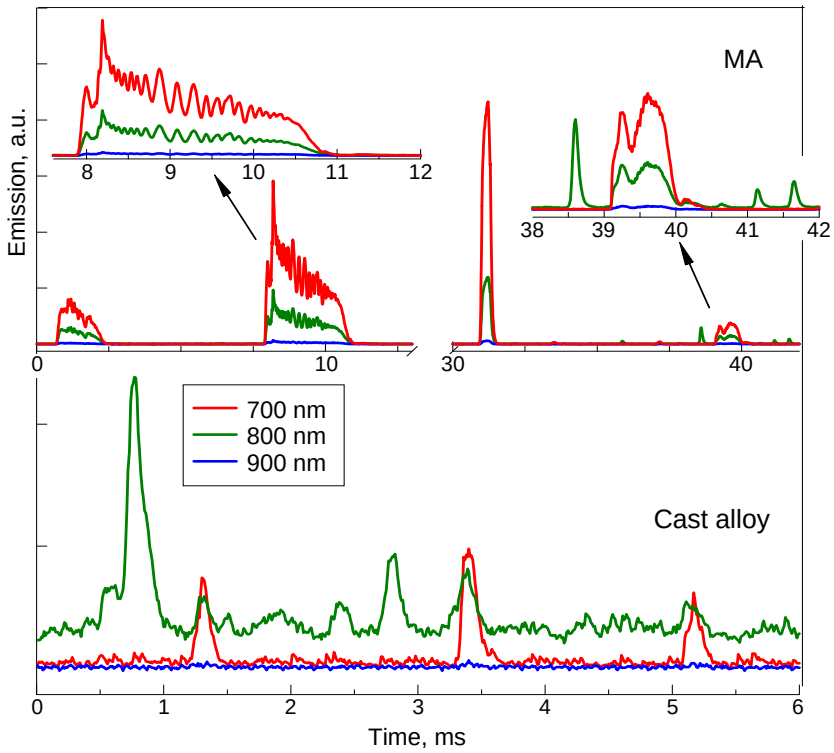

Figure 5.8 Emission pulses showing 3 PMT wavelengths for both mechanically-alloyed and cast-alloyed powders.

A magnified view of the emission trace measured at 700 nm for an MA particle is shown in Figure 5.9. In addition, the corresponding temperature trace obtained by 2-color pyrometry is shown. Consistently with the visible streaks in Figure 5.7, a strong, relatively narrow initial emission peak is observed. This first peak corresponds to a higher temperature and is followed by a second peak with a characteristic oscillatory emission pattern. The second peak is typically longer than the first, the temperature during the second peak remains nearly steady. This observed two-peak structure has been associated with a staged combustion, in which the first peak is dominated by combustion of Mg, while the second peak represents primarily combustion of Al [69, 95, 98].

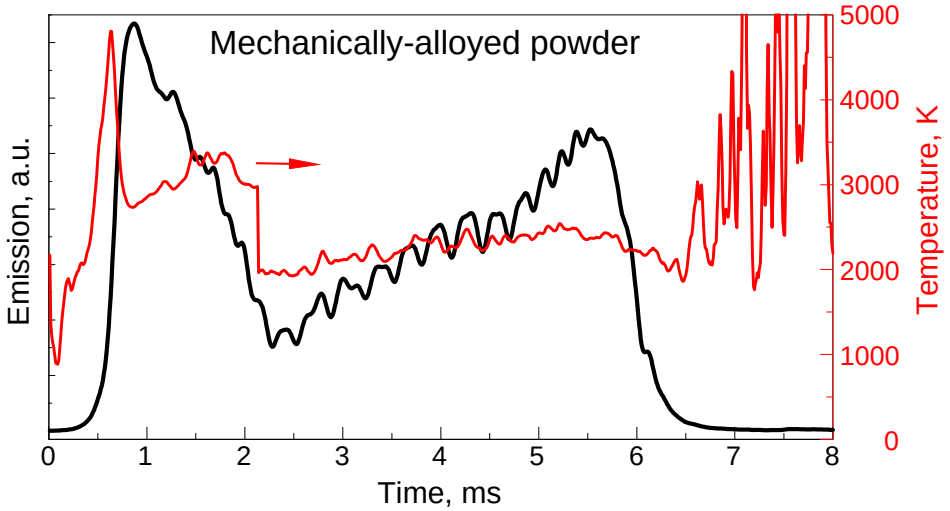

Figure 5.9 Emission signal (vertical scale is in arbitrary units) and temperature for a single, laser-ignited particle of MA Al·Mg powder.

A methodology described in Refs. [98, 100] was used to obtain a correlation between particle emission peak durations (proportional to their burn times) and particle sizes. Emission traces filtered at 700 nm were used for this correlation. The main assumption in this data processing is that the larger size particles burn longer. First, recorded emission pulses were preliminarily inspected to remove overlapping or closely spaced signals, which may not represent individual particle combustion events. Durations of the downselected pulses were then measured. The data on pulse durations (representing burn times) were logarithmically binned and correlated with the particle size distributions for the respective powders measured by Beckman-Coulter LS230 Enhanced Particle Analyzer. The volume-based particle size distributions shown in Figure 5.2 were transformed into number-based, cumulative distributions, and directly compared to the emission peak durations as explained previously and shown in Refs. [98, 100]. Once the size distributions were obtained in terms of particle number densities in respective size bins, the data were recast in terms of particle pulse durations as a function

of their size using interpolation between individual points. The final trends are shown in Figure 5.10. The plotted durations for cast alloy are substantially shorter than for the MA particles; however, this difference is unlikely to represent the true difference in the burn rates. Instead, as shown above, the cast alloy particles may not have burned completely, exhibiting short single-peak pulses, compared to double peak pulses produced by MA particles.

Also shown in Figure 5.10 are data reported previously for the MA Al·Mg powders with the same composition as used in the present study, for which an additional size reducing milling step was used with iodine added as a process control agent [95, 98]. The measurements reported earlier were made using a different PMT and filter selecting 568-nm emission. While the slopes of the trends showing pulse durations vs. particle size for MA are close to each other, it is striking that the earlier measurement produced a noticeably longer burn time compared to the present data for the effectively the same powder.

Additional experiments were performed to better understand the difference between the present and earlier measurements. In these additional experiments, laser ignited particles were monitored for both MA powders prepared for this study and the powder used in the previous work [95, 98], which has the same bulk Al/Mg composition but was additionally milled using 3-mm diameter steel balls for an hour with added 4 wt. % of iodine as a PCA. In addition to the filtered PMTs used here, a set of PMTs filtered at 532, 568, and 589 nm was used to collect particle emission for both powders. The emission times for a fixed number of particles determined using signals from the 700-nm and 568-nm PMTs were obtained and compared to each other for each powder. Emission

times were averaged over the entire set of the recorded particle emission pulses. The resulting average emission times for the powder used in the present experiments were consistent between the data sets collected at 700 and 568 nm. However, the emission times measured by different sensors differed from each other for the powder prepared for the earlier project, with particle sizes reduced by additional milling in presence of iodine. In the latter case, the average emission time measured at 568 nm was more than twice greater than that measured at 700 nm.

The difference is likely assigned to different sensitivity of different light sensors, which must be material-dependent. This observation, although not fully understood, illustrates that the emission times measured in such experiments cannot be directly translated into burn times, although comparisons between the measurements for different powders using the same detector remain valid.

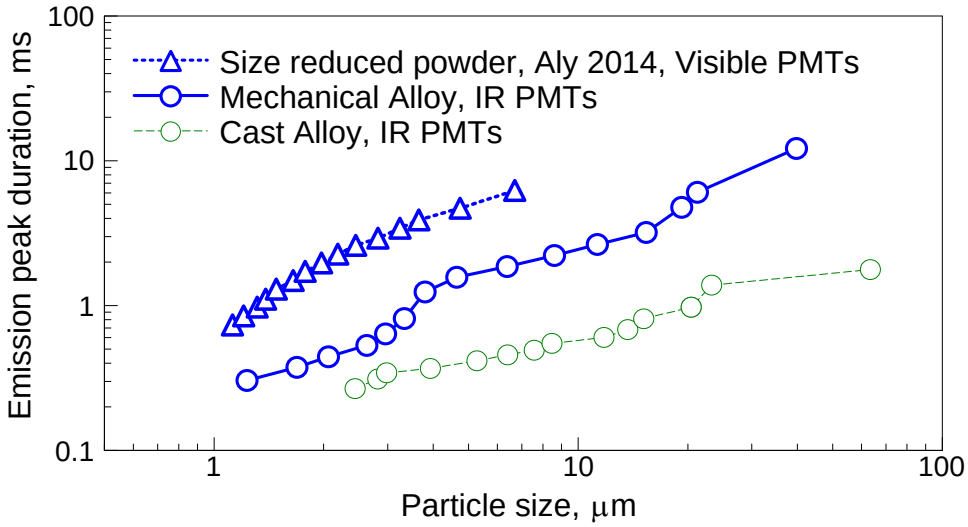

Figure 5.10 Particle emission peak durations as a function of size for the mechanically-alloyed and cast-alloyed powders. Also shown is the trend for size reduced Al·Mg powders from Refs. [95, 98].

The recorded temperature traces were averaged for each particle for the entire duration of the recorded emission pulse. These particle-average temperatures were further averaged over all particles in each pulse duration bin. Results are shown in Figure 5.11. Despite relatively large error bars showing standard deviation from the average temperature for each bin, the data suggest that temperatures are highest and exceed 3000 K for a narrow range of particle sizes, close to 2 μm. The average particle temperatures decrease noticeably, to about 2000 K, for coarser particles. Note that the temperatures reported in Figure 5.11 are somewhat lower than those reported earlier for the nominally the same MA particles [95, 98]. This difference is because the present results are obtained by averaging the temperature over the entire pulse duration, whereas in the previous report [95, 98] the temperatures were averaged during the time the emission pulse amplitude was above its half peak value.

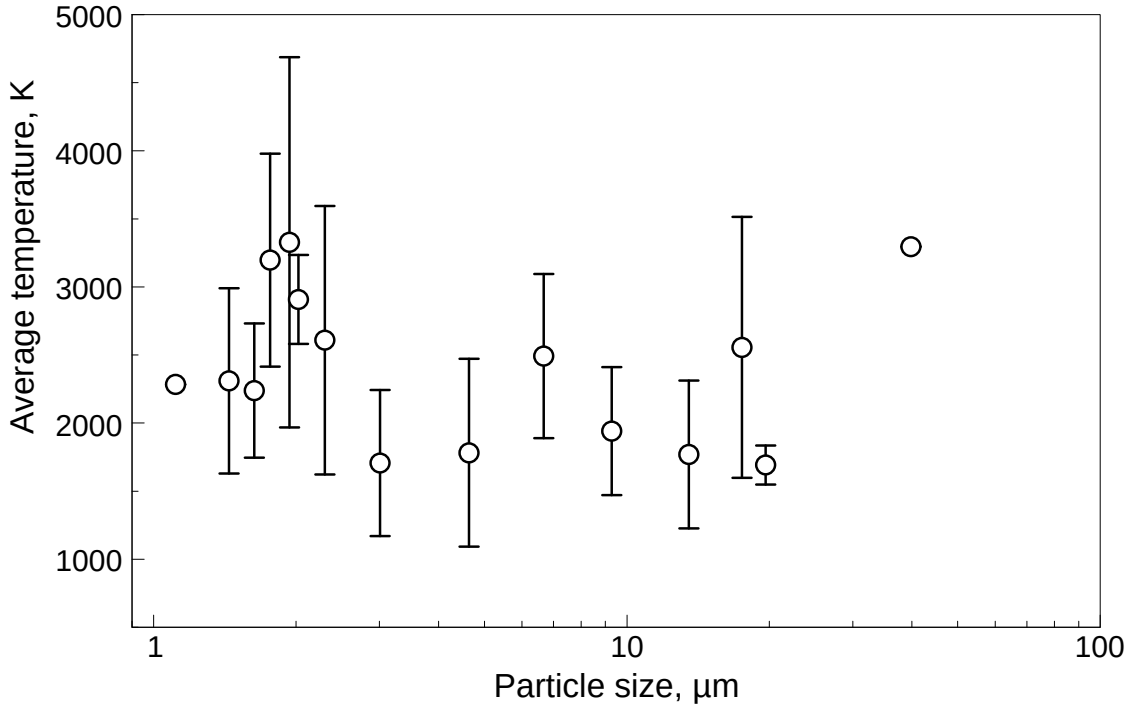

Figure 5.11 Combustion temperatures as a function of particle size for the prepared MA powder.

5.5 Discussion

In terms of practical applications, the present results show consistently that MA Al·Mg powders are more attractive reactive materials compared to their cast alloyed analogs. Ignition delays are reduced, burn rates are increased, and the reaction efficiency is improved based on the CVE experiments (Figure 5.6, Table 5.1). Slightly reduced ignition temperatures for the MA powders are also observed (Figure 5.4), which can be attributed to the additional exothermic reactions of formation of intermetallic phases during pre-heating of MA powders, as observed in DSC (Figure 5.5). However, the substantially greater burn rates observed in CVE experiments and, especially, qualitative differences in the particle combustion behavior in the laser ignition experiments (Figures

5.7, 5.8, and 5.10) are hard to reconcile with the relatively small difference in ignition temperatures detected for the two materials in the filament ignition tests.

It is suggested that the difference in the initial phase make-up and structure of the alloy particles (Figure 5.3) results in a different initiation and combustion regime, causing the observed differences in the combustion characteristics of the MA and cast alloy particles. The effect may only partially be related to the difference in the enthalpy of formation of the uniform $Al_{12}Mg_{17}$ intermetallic in the cast alloy vs. finely mixed Al and Mg in the composite MA powder. Indeed, the heat of formation of $Al_{12}Mg_{17}$ is reported to be close to -3.6 kJ/mol atom [101], a value essentially negligible compared to the heats of oxidation of Al or Mg (-837.8 and -600 kJ/mol atoms, respectively [102]. More likely, the difference in combustion is associated with the rate-dependent processes, including formation of the intermetallic phases upon heating in the MA powder and reaction of intermetallic and mixed Al/Mg composite. The formation of intermetallic is limited by the condensed phase diffusion. The diffusion coefficient of Mg in a molten Al can be estimated as $D = 9.9 \cdot 10^{-8} exp\left(-\frac{71,600}{RT}\right) \left[\frac{m^2}{s}\right]$ [103]. Considering temperature to be at the melting point of aluminum (close to the expected ignition point for these alloys), one obtains a diffusion coefficient of approximately $9.6 \cdot 10^{-9}$ m^2/s. For a micron-sized particle, the characteristic time of diffusion becomes close to 0.1 ms; the diffusion time exceeds 10 ms for a 10 μm particle. On the other hand, the heating time required to bring a room-temperature particle to the melting point of aluminum is close to 1 ms for the heating rate of 10^6 K/s, achieved in the laser ignition experiments (and close to those anticipated in CVE experiments). Thus, the time of the pre-ignition temperature ramp is comparable to the time of diffusion, so that formation of the intermetallic may not have

been completed in the MA particles before they were ignited. The evaporation of Mg from pure Mg inclusions is expected to occur at a different rate compared to that from the $Al_{12}Mg_{17}$ melt, which could explain a difference in the initial emissivity of the ignited MA (very bright) and cast alloy (dim) particles (Figure 5.7). Certainly, studies of activity of Mg in Al-Mg alloys show negative deviations from ideal behavior [104] suggesting a reduced vapor pressure of Mg compared to the ideal solution with the same Mg concentration. Conversely, the vapor pressure above pure Mg inclusions should be noticeably higher and unaffected by the presence of aluminum. This difference in the Mg vapor pressure can explain the pronounced initial, Mg-dominated combustion stage observed for the MA but not for the cast alloyed particles.

In addition, during the pre-heating, passivated oxidized layers form on the particle surface. The properties of such layers may be different for the pure Al and Mg vs. the oxidizing intermetallic phase. Further, oxidized layers are also formed during heterogeneous combustion. The structure and diffusion resistance of such layers are expected to depend on the structure and composition of the underlying metal or alloy. Because for larger particles, the diffusion times become comparable to the total measured burn times, such layers growing during combustion could have different properties for the MA and cast alloyed particles. Thus, not only ignition but also combustion would be affected by the structure and morphology of the alloyed particles.

Finally, it is of interest to comment on the observed effect of particle size on the average flame temperature (Figure 5.11). High temperatures observed for a relatively narrow range of particle sizes suggest that such particles were primarily burning in the vapor phase. However, reduction in the average temperature for the coarser particles

may be surprising. It could be explained by two-staged burn, where only the first stage dominated by evaporation of Mg occurs in the vapor phase. During the first stage, limited surface reaction could still have occurred producing alumina-based passivated layer on surface of the composite particles. As a result, subsequent reactions could be dominated by heterogeneous oxidation.

5.6 Conclusions

Aluminum-magnesium alloys were prepared by mechanical alloying and compared with materials prepared by cast alloying using powders with similar particle size distributions. MA powders had slightly lower ignition temperatures than cast-alloyed powders. In thermo-analytical measurements conducted in an inert environment, low-temperature exothermic features were observed for the MA powder but not for the cast-alloyed powder. These features were associated with the formation of intermetallic phases. Aerosol combustion experiments showed a substantial increase in both the maximum pressure and rate of pressure rise for the MA powders as compared to the cast alloyed powders. The effect was shown not to be caused by minor difference in the particle size distributions for the two materials. In single particle laser ignition experiments, MA particles ignited more readily than cast alloyed particles. MA powders burned in a staged sequence, with the first stage dominated by combustion of Mg and the second stage representing primarily combustion of Al. No similar staged combustion behavior was observed for the cast-alloyed powders, which generated very short emission pulses with a relatively low brightness, and thus might not have burned completely. It is proposed that the difference in the structure and morphology between the MA and cast

alloyed particles results in different ignition and combustion scenarios. Ignition is assisted by a weakly exothermic intermetallic reaction, generating a new material structure. More importantly, combustion occurs differently for a homogeneously mixed cast alloyed material and for the nano-composite produced by mechanical milling. At high heating rates, the MA powder structure may not have time to homogenize, resulting in a higher vapor pressure of Mg above Mg inclusions compared to that above a homogeneous liquid Al-Mg alloy. Composite structure can also cause different morphology, composition, and diffusion resistance of the oxidized surface layers formed during ignition and heterogeneous combustion. The latter differences cause different characteristics of heterogeneous combustion observed for MA and cast alloyed powder particles.

CHAPTER 6

CONCLUSIONS

Several reactive, mechanically milled materials were prepared and characterized. These powders contained Al and another metal (Fe, Ni, Zn, and Mg). Each prepared nanocomposite or alloyed material served as a high energy density material or additive to different energetic formulations.

For powders of Al·Fe, Al·Ni, and Al·Zn, it was illustrated that a small percentage of additive (10 at. %) to Al yielded altered ignition and combustion characteristics after very short milling times. For Ni and Zn, preparation of composites, while restricting formation of intermetallic phases, is only possible with very short milling times (120 min for Al·Fe and 20 min. for Al·Ni and Al·Zn). Thus, many Ni and Zn inclusions remain relatively coarse and particles are shaped as platelets (or coarse flakes) for both Al·Zn and Al·Ni composites prepared by ball milling. For Al·Fe, preparation of equiaxial particles was possible with fine Fe inclusions uniformly distributed in Al matrix. The presence of Fe, Ni, or Zn inclusions in the powders substantially changes ignition and low-temperature oxidation of the composite powders as compared to unmilled aluminum. The ignition of these composite materials occurs at lower temperatures, and low temperature oxidation is accelerated.

For powders with identical binary compositions, but milled longer, and thus containing intermetallic phases and a more homogenized Al matrix, the low temperature oxidation is impeded. Comparison of the reactive Al-metal composites with inert $Al{\cdot}Al_2O_3$ reference composites prepared with similar milling conditions suggests that the altered Al morphology, such as developed grain boundary network produced in the

milled powders, is primarily responsible for their accelerated low-temperature oxidation. It is further observed that simply an increase in the low-temperature oxidation rate detected in DSC/TGA experiments is insufficient to achieve ignition of the material under rapid heating conditions. Thus, it is concluded that the improved ignition dynamics for the prepared Al·metal composites is due to a combination of the accelerated low-temperature oxidation with reaction mechanisms altered by the presence of metal inclusions.

For 20-min. milled Al·Ni and Al·Zn composites, the oxidation begins with selective oxidation of Ni and Zn, respectively, and is followed by an Al oxidation step increased substantially compared to that observed for the pure Al at the same temperatures. For Al·Fe samples prepared with longer milling times, the first oxidation step is delayed and occurs after Al melting. The activation energies for the first oxidation step for all composite powders are different from that identified for the unmilled Al, indicating a difference in the reaction mechanisms. The subsequent oxidation steps are similar for the prepared composite and unmilled Al powders.

It is observed that the ignition is likely correlated with intermetallic reactions in Al·Ni and, possibly, Al·Fe composites. For all materials, a correlation between the first, low temperature Al oxidation step and ignition is also indicated. Unlike for the unmilled Al, for which oxidation at low temperatures results in growth and evolution of the protective surface oxide film, for the prepared Al·Zn and Al·Ni composites, the low temperature oxidation results in an effectively volumetric increase in the oxygen concentration in the Al matrix, but not in the inclusions of Zn and Ni, respectively.

Similarly, to the Al·Fe, Ni, and Zn composites mentioned above, mechanically alloyed powders of Al·Mg (1:1 by weight) were prepared, with the added goal of producing fine particle sizes. Reducing particle size became feasible using a modified, 2-step milling technique that allows for simultaneous adjustment in both internal structures and particle size distributions. Single-step milling used previously enables one to fine tune mixing between Al and other metal additives (e.g., Fe, Ni, and Zn), but is not capable of altering the size of the produced powder particles. Electron microscopy, x-ray diffraction patterns, and particle size distribution measurements showed that fine, equiaxial particles of Al·Mg with a homogeneous composition and a mean size of approximately 12.5 μm were produced by the 2-step milling. Filament ignition experiments of these mechanically alloyed powders conducted in air showed ignition temperatures in the range of 860 – 1060 K, which is significantly lower than ignition temperatures reported for pure Al powders which ignite at around 1850 K. Powders of Al·Mg ignite at temperatures lower than those of the Al·Fe, Ni, and Zn (between 960 – 1060 K) previously prepared. Premixed flames in air were produced in the powder cloud combustion experiments and showed that a higher pressure output and shorter ignition delay can be achieved as compared to pure Al powders. Single particle laser ignition experiments showed that once ignited, Al·Mg particles burn nearly as fast as pure Al particles of the same dimensions. It is also observed that the Al·Mg particles burn in a two-stage process proposed to include selective combustion of Mg followed by combustion of Al. Despite the slightly longer burn times, the improved ignition of Al·Mg particles and their high combustion temperatures make them a viable replacement for pure Al powders in different energetic formulations.

A more detailed study of mechanically alloyed Al·Mg powders with a broad range of compositions and desired fine particle sizes and shapes was feasible using the modified, 2-stage milling technique. Aluminum concentration was varied from less than 50 to 90 at. %. Electron microscopy, x-ray diffraction patterns, and particle size distribution measurements showed that fine, equiaxial Al·Mg particles with homogeneously mixed components and mean sizes between 7 - 13 μm can be prepared reproducibly. Ignition temperatures for all prepared Al·Mg alloys are much lower than those of pure Al powders and are close to those of Mg. Powders were aerosolized and ignited in air; the powder cloud combustion experiments showed that a higher maximum pressure, greater rates of pressure rise, and shorter ignition delays can be achieved for the mechanically alloyed powders, as compared to the pure Al powders with directly comparable particle size distributions. Similar to the study of 1:1 Al·Mg powders discussed previously, individual particle combustion experiments for the range of compositions showed that the mechanically alloyed particles also burn in two stages, with the first stage gradually disappearing with increased Al concentrations. The effect of particle size, d, on its burn time, t, for the prepared alloys is relatively well described by a $t \sim d^n$ law, where n is varying in the range of 1.1 - 1.5 for different compositions. It is observed that for particles greater than a few μm, the overall burn time decreases slightly with an increase in the aluminum concentration. The gas phase reactions resulting in production of molecular AlO emission are weaker for the prepared powders than for pure Al, but become increasingly more important as the aluminum concentration increases. The maximum flame temperatures of the prepared mechanically alloyed powders are the same or higher than for pure Al powders with similar size distributions.

Finally, an Al·Mg powder prepared by mechanical alloying was directly compared with a material prepared by grinding a cast alloy. Powders with the same both bulk compositions and similar particle size distributions for both mechanically alloyed and cast alloy metals were used. It was shown that mechanically alloyed powders had slightly lower ignition temperatures than cast-alloyed powders. In thermo-analytical measurements conducted in an inert environment, low-temperature exothermic features were observed for the mechanically alloyed powder but not for the cast-alloyed powder. These features were associated with the formation of intermetallic phases, similar to those observed with Al·Fe and Ni composites previously. Aerosol combustion experiments showed a substantial increase in both the maximum pressure and rate of pressure rise for the mechanically alloyed powders as compared to the cast alloyed powders. The effect was shown not to be caused by minor difference in the particle size distributions for the two materials. In single particle laser ignition experiments, mechanically alloyed particles ignited more readily than cast alloyed particles. Mechanically alloyed powders burned in a staged sequence, with the first stage dominated by combustion of Mg and the second stage representing primarily combustion of Al. No similar staged combustion behavior was observed for the cast-alloyed powders, which generated very short emission pulses with a relatively low brightness, and thus might not have burned completely.

It is proposed that the difference in the structure and morphology between the mechanically alloyed and cast alloyed particles results in different ignition and combustion scenarios. Ignition is assisted by a weakly exothermic intermetallic reaction, generating a new material structure. More importantly, combustion occurs differently for

a homogeneously mixed cast alloyed material and for the nano-composite produced by mechanical milling. At high heating rates, the mechanically alloyed powder structure may not have time to homogenize, resulting in a higher vapor pressure of Mg above Mg inclusions compared to that above a homogeneous liquid Al-Mg alloy. Composite structure can also cause different morphology, composition, and diffusion resistance of the oxidized surface layers formed during ignition and heterogeneous combustion. The latter differences lead to different characteristics of heterogeneous combustion observed for mechanically alloyed and cast alloyed powder particles.

In summary, it was shown that the mechanical alloying of metallic additives to Al produces powders with enhanced ignition and burn characteristics compared to pure Al powders. With these improvements in reactivity, the mechanically alloyed materials can be used as drop-in replacements to pure Al powders in various energetic formulations such as propellants, explosives, and pyrotechnics. Future research can be directed at more detailed studies of the combustion mechanisms of such materials. It would be of interest to investigate the ageing mechanisms of such powders as ageing would also affect ignition and combustion characteristics. Finally, the commercialization of the preparation of these powders would assist in the ease of their use as fuel additives.

REFERENCES

[1] J. P. Agrawal, *High Energy Materials: Propellants, Explosives and Pyrotechnics*, New York, NY: Wiley-VCH, 2010.

[2] P. F. Pagoria, G. S. Lee, A. R. Mitchell, and R. D. Schmidt, "A review of energetic materials synthesis," *Thermochimica Acta,* vol. 384, pp. 187-204, 2002.

[3] E. L. Dreizin, "Metal-based reactive nanomaterials," *Progress in Energy and Combustion Science,* vol. 35, pp. 141-167, 2009.

[4] T. B. Brill and K. J. James, "Kinetics and mechanisms of thermal decomposition of nitroaromatic explosives," *Chemical Reviews,* vol. 93, pp. 2667-2692, 1993.

[5] D. M. Badgujar, M. B. Talawar, S. N. Asthana, and P. P. Mahulikar, "Advances in science and technology of modern energetic materials: An overview," *Journal of Hazardous Materials,* vol. 151, pp. 289-305, 2008.

[6] C. M. Tarver, "Chemical Kinetic Modeling of HMX and TATB Laser Ignition Tests," *Journal of Energetic Materials,* vol. 22, pp. 93-107, 2004/04/01 2004.

[7] V. I. Rozenband and N. I. Vaganova, "A strength model of heterogeneous ignition of metal particles," *Combustion and Flame,* vol. 88, pp. 113-118, 1992.

[8] E. L. Dreizin, "Effect of Phase Changes on Metal-Particle Combustion Processes," *Combustion, Explosion, and Shock Waves,* vol. 39, pp. 681-693, 2003.

[9] A. Gany and D. W. Netzer, "Fuel performance evaluation for solid-fueled ramjet," *International Journal of Turbo and Jet Engines,* vol. 2, pp. 157-168, 1985.

[10] B. Palaszewski and R. Powell, "Launch vehicle perfomance using metallized propellants," *Journal of Propulsion and Power,* vol. 10, pp. 828-833, 1994.

[11] B. Palaszewski, "Metallized propellants for the human exploration of Mars," *Journal of Propulsion and Power,* vol. 8, pp. 1192-1199, 1992.

[12] K. C. Walter, D. R. Pesiri, and D. E. Wilson, "Manufacturing and performance of nanometric Al/MoO_3 energetic materials," *Journal of Propulsion and Power,* vol. 23, pp. 645-650, 2007.

[13] A. Prakash, A. V. McCormick, and M. R. Zachariah, "Synthesis and reactivity of a super-reactive metastable intermolecular composite formulation of $Al/KMnO_4$," *Advanced Materials,* vol. 17, pp. 900-903, 2005.

[14] W. L. Perry, B. C. Tappan, B. L. Reardon, V. E. Sanders, and S. F. Son, "Energy release characteristics of the nanoscale aluminum-tungsten oxide hydrate metastable intermolecular composite," *Journal of Applied Physics,* vol. 101, 2007.

[15] D. Stamatis, Z. Jiang, V. K. Hoffmann, M. Schoenitz, and E. L. Dreizin, "Fully dense, aluminum-rich Al-CuO nanocomposite powders for energetic formulations," *Combustion Science and Technology,* vol. 181, pp. 97-116, 2009.

[16] M. Schoenitz, T. S. Ward, and E. L. Dreizin, "Fully dense nano-composite energetic powders prepared by arrested reactive milling," *Proceedings of the Combustion Institute*, 2005, pp. 2071-2078.

[17] T. M. Tillotson, A. E. Gash, R. L. Simpson, L. W. Hrubesh, J. H. Satcher Jr, and J. F. Poco, "Nanostructured energetic materials using sol-gel methodologies," *Journal of Non-Crystalline Solids,* vol. 285, pp. 338-345, 2001.

[18] A. E. Gash, T. M. Tillotson, J. H. Satcher Jr, L. W. Hrubesh, and R. L. Simpson, "New sol-gel synthetic route to transition and main-group metal oxide aerogels using inorganic salt precursors," *Journal of Non-Crystalline Solids,* vol. 285, pp. 22-28, 2001.

[19] A. E. Gash, T. M. Tillotson, J. H. Satcher Jr, J. F. Poco, L. W. Hrubesh, and R. L. Simpson, "Use of epoxides in the sol-gel synthesis of porous iron(III) oxide monoliths from Fe(III) salts," *Chemistry of Materials,* vol. 13, pp. 999-1007, 2001.

[20] K. B. Plantier, M. L. Pantoya, and A. E. Gash, "Combustion wave speeds of nanocomposite Al/Fe_2O_3: The effects of Fe_2O_3 particle synthesis technique," *Combustion and Flame,* vol. 140, pp. 299-309, 2005.

[21] A. E. Gash, J. H. Satcher Jr, R. L. Simpson, and B. J. Clapsaddle, "Nanostructured energetic materials with sol-gel methods," *Material Research Symposium Proceedings*, pp. 55-66, 2003.

[22] S. R. Gangopadhyay S, Subramanian S, Gangopadhyay K, Hasan S., "Ordered nanoenergetic thermites as self-assembled nanostructures with tunable combustion properties," US Patent, 2007.

[23] S. Subramaniam, Hasan, S., Bhattacharya, S., Gao, Y., Apperson, S., Hossain, M., "Self-assembled nanoenergetic composites," *Material Research Society Symposium* 2006, pp. 9-14.

[24] E. Ma, C. V. Thompson, L. A. Clevenger, and K. N. Tu, "Self-propagating explosive reactions in Al/Ni multilayer thin films," *Applied Physics Letters,* vol. 57, pp. 1262-1264, 1990.

[25] A. J. Gavens, D. Van Heerden, A. B. Mann, M. E. Reiss, and T. P. Weihs, "Effect of intermixing on self-propagating exothermic reactions in Al/Ni nanolaminate foils," *Journal of Applied Physics,* vol. 87, pp. 1255-1263, 2000.

[26] K. J. Blobaum, M. E. Reiss, J. M. Plitzko Lawrence, and T. P. Weihs, "Deposition and characterization of a self-propagating CuOx/Al thermite reaction in a multilayer foil geometry," *Journal of Applied Physics,* vol. 94, pp. 2915-2922, 2003.

[27] K. J. Blobaum, A. J. Wagner, J. M. Plitzko, D. Van Heerden, D. H. Fairbrother, and T. P. Weihs, "Investigating the reaction path and growth kinetics in CuO_x/Al multilayer foils," *Journal of Applied Physics,* vol. 94, pp. 2923-2929, 2003.

[28] E. Beloni, V. K. Hoffmann, and E. L. Dreizin, "Combustion of decane-based slurries with metallic fuel additives," *Journal of Propulsion and Power,* vol. 24, pp. 1403-1411, 2008.

[29] Y. L. Shoshin and E. L. Dreizin, "Particle combustion rates for mechanically alloyed Al-Ti and aluminum powders burning in air," *Combustion and Flame,* vol. 145, pp. 714-722, 2006.

[30] Y. L. Shoshin, R. S. Mudryy, and E. L. Dreizin, "Preparation and characterization of energetic Al-Mg mechanical alloy powders," *Combustion and Flame,* vol. 128, pp. 259-269, 2002.

[31] X. Zhu, M. Schoenitz, and E. L. Dreizin, "Mechanically alloyed Al-Li powders," *Journal of Alloys and Compounds,* vol. 432, pp. 111-115, 2007.

[32] C. Suryanarayana, "Mechanical alloying and milling," *Progress in Materials Science,* vol. 46, pp. 1-184, 2001.

[33] M. Schoenitz and E. L. Dreizin, "Structure and properties of Al-Mg mechanical alloys," *Journal of Materials Research,* vol. 18, pp. 1827-1836, 2003.

[34] A. L. Breiter, E. I. Popov, and V. L. Velikanova, *Fizika Aerodispersnykh Sistem (Physics of Aerodisderse Systems),* vol. 23, pp. 43-48, 1983.

[35] T. A. Roberts, R. L. Burton, and H. Krier, "Ignition and combustion of aluminum/magnesium alloy particles in O_2 at high pressures," *Combustion and Flame,* vol. 92, pp. 125-143, 1993.

[36] S. Yuasa and T. Takeno, "Ignition and combustion of magnesium-aluminum alloy particle clouds in a hot gas stream," *Symposium (International) on Combustion,* vol. 19, pp. 741-748, 1982.

[37] S. Zhang, M. Schoenitz, and E. L. Dreizin, "Mechanically alloyed Al-I composite materials," *Journal of Physics and Chemistry of Solids,* vol. 71, pp. 1213-1220, 2010.

[38] M. Schoenitz, T. S. Ward, and E. L. Dreizin, "Arrested reactive milling for in-situ production of energetic nanocomposites for propulsion and energy-intensive technologies in exploration missions," *43rd AIAA Aerospace Sciences Meeting,* pp. 3001-3006, 2005.

[39] S. S. Nayak, M. Wollgarten, J. Banhart, S. K. Pabi, and B. S. Murty, "Nanocomposites and an extremely hard nanocrystalline intermetallic of Al-Fe alloys prepared by mechanical alloying," *Materials Science and Engineering A,* vol. 527, pp. 2370-2378, 2010.

[40] M. Tavoosi, M. H. Enayati, and F. Karimzadeh, "Softening behaviour of nanostructured Al-14 wt% Zn alloy during mechanical alloying," *Journal of Alloys and Compounds,* vol. 464, pp. 107-110, 2008.

[41] J. D. E. White, R. V. Reeves, S. F. Son, and A. S. Mukasyan, "Thermal explosion in Ni-Al system: Influence of mechanical activation," *Journal of Physical Chemistry A,* vol. 113, pp. 13541-13547, 2009.

[42] Y. L. Shoshin, M. A. Trunov, X. Zhu, M. Schoenitz, and E. L. Dreizin, "Ignition of aluminum-rich Al-Ti mechanical alloys in air," *Combustion and Flame,* vol. 144, pp. 688-697, 2006.

[43] T. S. Ward, M. A. Trunov, M. Schoenitz, and E. L. Dreizin, "Experimental methodology and heat transfer model for identification of ignition kinetics of powdered fuels," *International Journal of Heat and Mass Transfer,* vol. 49, pp. 4943-4954, 2006.

[44] H. Okamoto, *Desk Handbook Phase Diagrams for Binary Alloys*, Materials Park, OH: ASM International, 2000.

[45] M. Schoenitz, B. Patel, O. Agboh, and E. L. Dreizin, "Oxidation of aluminum powders at high heating rates," *Thermochimica Acta,* vol. 507-508, pp. 115-122, 2010.

[46] M. A. Trunov, M. Schoenitz, X. Zhu, and E. L. Dreizin, "Effect of polymorphic phase transformations in Al_2O_3 film on oxidation kinetics of aluminum powders," *Combustion and Flame,* vol. 140, pp. 310-318, 2005.

[47] M. A. Trunov, M. Schoenitz, and E. L. Dreizin, "Effect of polymorphic phase transformations in alumina layer on ignition of aluminium particles," *Combustion Theory and Modelling,* vol. 10, pp. 603-623, 2006.

[48] S. Mohan, M. A. Trunov, and E. L. Dreizin, "Characterization of Aluminum Powder Ignition," *The 2003 Technical Meeting of the Eastern States Section of the Combustion Institute*, University Park, PA, 2003, pp. 329-332.

[49] H. E. Kissinger, "Reaction kinetics in differential thermal analysis," *Analytical Chemistry,* vol. 29, pp. 1702-1706, 1957.

[50] L. Meda, G. Marra, L. Galfetti, F. Severini, and L. De Luca, "Nano-aluminum as energetic material for rocket propellants," *Materials Science and Engineering C,* vol. 27, pp. 1393-1396, 2007.

[51] J. K. Sambamurthi, E. W. Price, and R. K. Sigman, "Aluminum agglomeration in solid-propellant combustion," *AIAA Journal,* vol. 22, pp. 1132-1138, 1984.

[52] P. Brousseau and C. J. Anderson, "Nanometric aluminum in explosives," *Propellants, Explosives, Pyrotechnics,* vol. 27, pp. 300-306, 2002.

[53] L. T. Luca, L. Galfetti, F. Severini, L. Meda, G. Marra, A. B. Vorozhtsov*, et al.*, "Burning of Nano-Aluminized Composite Rocket Propellants," *Combustion, Explosion and Shock Waves,* vol. 41, pp. 680-692, 2005/11/01 2005.

[54] A. Pivkina, P. Ulyanova, Y. Frolov, S. Zavyalov, and J. Schoonman, "Nanomaterials for Heterogeneous Combustion," *Propellants, Explosives, Pyrotechnics,* vol. 29, pp. 39-48, 2004.

[55] A. Ingenito and C. Bruno, "Using aluminum for space propulsion," *Journal of Propulsion and Power,* vol. 20, pp. 1056-1063, 2004.

[56] E. L. Dreizin and M. Schoenitz, US Patent 7524355, 2009.

[57] S. Umbrajkar, M. A. Trunov, M. Schoenitz, E. L. Dreizin, and R. Broad, "Arrested reactive milling synthesis and characterization of sodium-nitrate based reactive composites," *Propellants, Explosives, Pyrotechnics,* vol. 32, pp. 32-41, 2007.

[58] S. M. Umbrajkar, M. Schoenitz, and E. L. Dreizin, "Fuel-rich Al-MoO_3 nanocomposite powders prepared by arrested reactive milling," *45th AIAA Aerospace Sciences Meeting*, 2007, pp. 3590-3595.

[59] S. M. Umbrajkar, S. Seshadri, M. Schoenitz, V. K. Hoffmann, and E. L. Dreizin, "Aluminum-rich Al-MoO_3 nanocomposite powders prepared by arrested reactive milling," *Journal of Propulsion and Power,* vol. 24, pp. 192-198, 2008.

[60] J. H. de Boer, "Flash Lamp," US Patent 2325667, 1943.

[61] J. H. O'Neill, "Producing heat with aluminum and magnesium or other metallic fuel," US Patent 1532930, 1925.

[62] A. I. Sidorov, I. P. Kravchenko, V. M. Antonov, M. M. Arsh, F. P. Madyakin, L. Y. Gudoshnikova, S. Ugol'kova, "Pyrotechnic composition for yellow flames," Soviet Patent SU237041, 1969.

[63] H. Habu, "Application of magnalium to solid rocket propellant," *Keikinzoku (Journal of Japan Institute of Light Metals),* vol. 58, pp. 162-166, 2008.

[64] R. H. Chen, C. Suryanarayana, and M. Chaos, "Combustion characteristics of mechanically alloyed ultrafine-grained Al-Mg powders," *Advanced Engineering Materials,* vol. 8, pp. 563-567, 2006.

[65] V. G. Poyarkov and I. Vyssh, "Combustibility of aluminum-magnesium powdered alloys," *Tsvetnye Metally,* Uchebnye Zavedeniya, vol. 10, pp. 149-153, 1967.

[66] E. I. Popov, Kashporov, L. Ya., Mal'tsev, V.M, and Breiter, A.L., "Combustion mechanism of aluminum-magnesium alloy particles," *Combustion, Explosion, and Shockwaves,* vol. 9, pp. 204-208, 1973.

[67] A. A. Zenin, G. P. Kuznetsov, and V. I. Kolesnikov, *Khimicheskaya Fizika (Russian Journal of Physical Chemistry B),* vol. 30, pp. 28-41, 2011.

[68] V. I. Glukhov and V. I. Gnatovskii, *Fizika Aerodispersnykh Sistem (Physics of Aerodisderse Systems),* vol. 5, pp. 71-76, 1971.

[69] E. I. Popov, L. Y. Kashporov, V. M. Mal'tsev, and A. L. Breiter, "Combustion mechanism of aluminum - magnesium alloy particles," *Combustion, Explosion, and Shock Waves,* vol. 9, pp. 204-208, 1975.

[70] B. Z. Eapen, V. K. Hoffmann, M. Schoenitz, and E. L. Dreizin, "Combustion of aerosolized spherical aluminum powders and flakes in air," *Combustion Science and Technology,* vol. 176, pp. 1055-1069, 2004.

[71] P. R. Santhanam, V. K. Hoffmann, M. A. Trunov, and E. L. Dreizin, "Characteristics of aluminum combustion obtained from constant-volume explosion experiments," *Combustion Science and Technology,* vol. 182, pp. 904-921, 2010.

[72] M. Schoenitz, E. L. Dreizin, and E. Shtessel, "Constant volume explosions of aerosols of metallic mechanical alloys and powder blends," *Journal of Propulsion and Power,* vol. 19, pp. 405-412, 2003.

[73] I. Glassman, *Combustion*, 3rd ed. San Diego, CA: Academic Press, 1996.

[74] C. Badiola, R. J. Gill, and E. L. Dreizin, "Combustion characteristics of micron-sized aluminum particles in oxygenated environments," *Combustion and Flame,* vol. 158, pp. 2064-2070, 2011.

[75] R. J. Gill, C. Badiola, and E. L. Dreizin, "Combustion times and emission profiles of micron-sized aluminum particles burning in different environments," *Combustion and Flame,* vol. 157, pp. 2015-2023, 2010.

[76] R. J. Gill, S. Mohan, and E. L. Dreizin, "Sizing and burn time measurements of micron-sized metal powders," *Review of Scientific Instruments,* vol. 80, 2009.

[77] E. L. Dreizin, C. Badiola, S. Zhang, and Y. Aly, "Particle combustion dynamics of metal-based reactive materials.," *International Journal of Energetic Materials and Chemical Propulsion,* 2012.

[78] S. Zhang, C. Badiola, M. Schoenitz, and E. L. Dreizin, "Oxidation, ignition, and combustion of $Al{\cdot}I_2$ composite powders," *Combustion and Flame,* vol. 159, pp. 1980-1986, 2012.

[79] D. L. Zhang, T. B. Massalski, and M. R. Paruchuri, "Formation of metastable and equilibrium phases during mechanical alloying of Al and Mg powders," *Metallurgical and Materials Transactions A: Physical Metallurgy and Materials Science,* vol. 25 A, pp. 73-79, 1994.

[80] N. Saunders, "A review and thermodynamic assessment of the Al-Mg and Mg-Li systems," *Calphad,* vol. 14, pp. 61-70, 1990.

[81] M. Schoenitz and E. L. Dreizin, "Oxidation processes and phase changes in metastable Al-Mg alloys," *Journal of Propulsion and Power,* vol. 20, pp. 1064-1068, 2004.

[82] B. J. McBride and S. Gordon, "NASA RP 1311," *Computer Program for Calculation of Complex Chemical Equilibrium Compositions and Applications II. User's Manual and Program Description,* 1996.

[83] A. L. Corcoran, V. K. Hoffmann, and E. L. Dreizin, "Aluminum particle combustion in turbulent flames," *Combustion and Flame,* vol. 160, pp. 718-724, 2013.

[84] B. R. Clark and M. L. Pantoya, "The aluminium and iodine pentoxide reaction for the destruction of spore forming bacteria," *Physical Chemistry Chemical Physics,* vol. 12, pp. 12653-12657, 2010.

[85] C. Farley and M. Pantoya, "Reaction kinetics of nanometric aluminum and iodine pentoxide," *Journal of Thermal Analysis and Calorimetry,* vol. 102, pp. 609-613, 2010.

[86] S. A. Grinshpun, A. Adhikari, M. Yermakov, T. Reponen, E. Dreizin, M. Schoenitz*, et al.*, "Inactivation of aerosolized Bacillus atrophaeus (BG) endospores and MS2 viruses by combustion of reactive materials," *Environmental Science and Technology,* vol. 46, pp. 7334-7341, 2012.

[87] S. Zhang, M. Schoenitz, and E. L. Dreizin, "Iodine release, oxidation, and ignition of mechanically alloyed Al-I composites," *Journal of Physical Chemistry C,* vol. 114, pp. 19653-19659, 2010.

[88] E. L. Dreizin, Y. L. Shoshin, R. S. Mudryy, and V. K. Hoffmann, "Constant pressure flames of aluminum and aluminum-magnesium mechanical alloy aerosols in microgravity," *Combustion and Flame,* vol. 130, pp. 381-385, 2002.

[89] C. Badiola and E. L. Dreizin, "On weak effect of particle size on its burn time for micron-sized aluminum powders," *Combustion Science and Technology,* vol. 184, pp. 1993-2007, 2012.

[90] S. Mohan, M. A. Trunov, and E. L. Dreizin, "On possibility of vapor-phase combustion for fine aluminum particles," *Combustion and Flame,* vol. 156, pp. 2213-2216, 2009.

[91] Y. Lin, W. Liu, L. Wang, and E. J. Lavernia, "Ultra-fine grained structure in Al-Mg induced by discontinuous dynamic recrystallization under moderate straining," *Materials Science and Engineering A,* vol. 573, pp. 197-204, 2013.

[92] G. Ribárik, J. Gubicza, and T. Ungár, "Correlation between strength and microstructure of ball-milled Al-Mg alloys determined by X-ray diffraction," *Materials Science and Engineering A,* vol. 387-389, pp. 343-347, 2004.

[93] S. J. Kim, S. J. Lee, J. Y. Jeong, and K. H. Kim, "Electrochemical characteristics of Al-Mg and Al-Mg-Si alloy in sea water," *Transactions of Nonferrous Metals Society of China (English Edition),* vol. 22, pp. s881-s886, 2012.

[94] S. Bouaricha, J. P. Dodelet, D. Guay, J. Huot, S. Boily, and R. Schulz, "Hydriding behavior of Mg-Al and leached Mg-Al compounds prepared by high-energy ball-milling," *Journal of Alloys and Compounds,* vol. 297, pp. 282-293, 2000.

[95] Y. Aly, M. Schoenitz, and E. L. Dreizin, "Ignition and combustion of mechanically alloyed Al-Mg powders with customized particle sizes," *Combustion and Flame,* vol. 160, pp. 835-842, 2013.

[96] S. M. Umbrajkar, M. Schoenitz, S. R. Jones, and E. L. Dreizin, "Effect of temperature on synthesis and properties of aluminum-magnesium mechanical alloys," *Journal of Alloys and Compounds,* vol. 402, pp. 70-77, 2005.

[97] C. Johnson, Parr, T., Hanson-Parr, D., Hollins, R., Fallis, S., and Higa, K., "Combustion and Oxidation of Metal Nanoparticles and Composite Particles," *Proceedings of the 37th JANNAF Combustion Subcommittee Meeting,* vol. 1, pp. 539-551, 2000.

[98] Y. Aly, V. K. Hoffman, M. Schoenitz, and E. L. Dreizin, "Reactive, mechanically alloyed Al·Mg powders with customized particle sizes and compositions," *Journal of Propulsion and Power,* vol. 30, pp. 96-104, 2014.

[99] C. Badiola and E. L. Dreizin, "Combustion of micron-sized particles of titanium and zirconium," *Proceedings of the Combustion Institute,* vol. 34, pp. 2237-2243, 2013.

[100] S. Zhang, M. Schoenitz, and E. L. Dreizin, "Nearly pure aluminum powders with modified protective surface," *Combustion Science and Technology,* vol. 185, pp. 1360-1377, 2013.

[101] Y. Zhong, M. Yang, and Z. K. Liu, "Contribution of first-principles energetics to Al-Mg thermodynamic modeling," *Calphad: Computer Coupling of Phase Diagrams and Thermochemistry,* vol. 29, pp. 303-311, 2005.

[102] M. W. Chase, "NIST-JANAF Thermochemical Tables, 4th Edition," *Journal of Physical Chemistry Reference Data, Monograph 9,* pp. 1-1951, 1998.

[103] Y. Du, Y. A. Chang, B. Huang, W. Gong, Z. Jin, H. Xu, *et al.*, "Diffusion coefficients of some solutes in fcc and liquid Al: critical evaluation and correlation," *Materials Science and Engineering: A,* vol. 363, pp. 140-151, 12/20/ 2003.

[104] Z. Moser, W. Zakulski, K. Rzyman, W. Gasior, Z. Panek, I. Katayama, *et al.*, "New thermodynamic data for liquid Aluminum-Magnesium alloys from emf, vapor pressures, and calorimetric studies," *Journal of Phase Equilibria,* vol. 19, pp. 38-47, 1998.